



**This electronic thesis or dissertation has been  
downloaded from Explore Bristol Research,  
<http://research-information.bristol.ac.uk>**

*Author:*

**Major, Will R**

*Title:*

**Marine heatwaves and oxygen extremes in the Mediterranean Sea under climate change**

**General rights**

Access to the thesis is subject to the Creative Commons Attribution - NonCommercial-No Derivatives 4.0 International Public License. A copy of this may be found at <https://creativecommons.org/licenses/by-nc-nd/4.0/legalcode> This license sets out your rights and the restrictions that apply to your access to the thesis so it is important you read this before proceeding.

**Take down policy**

Some pages of this thesis may have been removed for copyright restrictions prior to having it been deposited in Explore Bristol Research. However, if you have discovered material within the thesis that you consider to be unlawful e.g. breaches of copyright (either yours or that of a third party) or any other law, including but not limited to those relating to patent, trademark, confidentiality, data protection, obscenity, defamation, libel, then please contact [collections-metadata@bristol.ac.uk](mailto:collections-metadata@bristol.ac.uk) and include the following information in your message:

- Your contact details
- Bibliographic details for the item, including a URL
- An outline nature of the complaint

Your claim will be investigated and, where appropriate, the item in question will be removed from public view as soon as possible.



Master's by Research in

# Global Environmental Challenges

'Marine Heatwaves and Oxygen  
Extremes in the Mediterranean  
Sea under Climate Change'  
William Richard Major

 University of  
BRISTOL  
Cabot Institute  
for the Environment

Word count: 15487

## Abstract

Significant physical and biogeochemical alterations to the ocean have occurred in the recent past as a result of anthropogenic climate change, including warming and deoxygenation. A consequence of rising temperatures is the increasing frequency, intensity and duration of marine heatwaves (MHWs), which are defined as discrete and prolonged periods of anomalously warm temperatures (Hobday et al., 2016). Biogeochemical responses to MHWs remain unclear and there is a growing concern regarding extremes in marine biogeochemistry. Further, global dissolved oxygen concentrations  $[O_2]$  have declined over the last 50 years. I use a high resolution 3-D physical-biogeochemical modelled dataset for the Mediterranean Sea (MS) from 1982-2100 to explore extremes in temperature and deoxygenation. The MS is a climate change hotspot and has experienced many MHWs as well as localised periods of hypoxia.

MHW events in the Mediterranean Sea are one-in-a-hundred-day events in historical simulation and become one-in-six-day events by the end of the century under RCP4.5. By applying MHW definitions to  $[O_2]$  model output, my work defines low-end extreme  $[O_2]$  events, termed major oxygen lows (MOLs). I find evidence of MOLs in the historical simulation that develop into annual events between 80-200 metres depth with mean event duration and intensity increasing by a factor of 3 under the same moderate scenario. This is driven by a reduction in mean  $[O_2]$  whereby the historical extreme threshold becomes the new normal in large portions of the basin. Furthermore, I find that increased MHW intensity enhances subsurface deoxygenation ( $<1 \mu\text{mol l}^{-1}$ ). Mediterranean regions that experience more intense MHWs also demonstrate stronger deoxygenation signals implying that a similar relationship could be found in other climatically sensitive areas of the ocean.

## Acknowledgements

I would like to thank my supervisor, Dr Oliver Andrews, for his infectious passion and enthusiasm for ocean science and computer programming, and his patience and understanding during my learning. I would like to further thank my secondary supervisor, Dr Fanny Monteiro, for her support and feedback on my work. I acknowledge and very much appreciate the role of the Cabot Institute for Environment in creating a master's course that allowed me to be successful in my aim of working in the science sector. I would also like to highlight my gratitude for the people whom I have lived with during this two-year process; they have witnessed and endured my fluctuating emotional state, especially during the times of homeworking. The greatest level of gratitude goes to my father, Neil, for his timely words of encouragement and the financial support that allowed me to take a desired path. And finally, thanks must go to those that have kindly agreed to assess my work as it is greatly appreciated.

# Table of contents

Abstract .....	i
Acknowledgements .....	ii
Table of contents .....	iii
Comments on figure and table captions inline .....	vi
Table captions .....	vi
Figure captions .....	vii
1 Introduction .....	1
2 Literature review .....	3
2.1 Marine heatwaves .....	3
2.1.1 Definitions.....	3
2.1.2 Drivers.....	5
2.1.3 MHWs under climate change .....	7
2.2.4 Biogeochemical effects .....	8
2.2 Ocean deoxygenation.....	9
2.2.1 Fundamental controls on dissolved oxygen.....	9
2.2.2 Drivers.....	11
2.2.3 Impacts.....	13
2.3 The Mediterranean Sea .....	16
2.3.1 Physical and biogeochemical characteristics .....	16
2.3.2 Observed extremes.....	20

2.3.3	Future of the Mediterranean Sea .....	23
2.4	Aims and research questions.....	24
3	Methods .....	26
3.1	Data .....	26
3.1.1	Model data .....	26
3.1.2	POLCOMS .....	27
3.1.3	ERSEM .....	28
3.1.4	Climate and ocean forcing.....	29
3.1.5	Methods used for model-data comparison and results calculations .....	31
3.2	Model-data comparison.....	32
3.2.1	Sea Surface Temperature.....	32
3.2.2	Seasonal water column validation .....	37
3.3	Apparent oxygen utilisation.....	44
4	Results and discussion.....	45
4.1	Changes to mean and extreme states .....	47
4.1.1	Spatially averaged changes .....	47
4.1.2	Changes in spatial patterns.....	54
4.2	MHW and MOL event diagnostics.....	58
4.2.1	MHW characteristics .....	58
4.2.2	MOL event characteristics.....	62
4.2.3	Event sequencing and seasonality .....	63

4.3	MHW event intensity and category comparison .....	69
4.3.1	Intensity comparison .....	70
4.3.2	Category comparison .....	75
4.4	Implications and recommendations .....	78
5	Conclusions .....	82
6	References.....	83

# Comments on figure and table captions inline

## Table captions

TABLE 1: MEAN AND SPATIAL MAXIMUM ROOT MEAN SQUARE ERROR (RMSE) VALUES FOR POLCOMS-ERSEM [O<sub>2</sub>] AGAINST OBSERVATIONS FOR EACH BASIN OF THE MS AT THE SURFACE (0-50 METRES) AND WITHIN THE INTERIOR (80-200 METRES). .....40

TABLE 2: A SUMMARY OF SPATIAL AVERAGED POLCOMS-ERSEM ANALYSIS. MEAN AND EXTREME THRESHOLD TRENDS IN SST AND [O<sub>2</sub>]<sup>100</sup> ARE BASED ON ANNUAL MEANS AND GIVEN IN °C YEAR<sup>-1</sup> AND μMOL L<sup>-1</sup> YEAR<sup>-1</sup> ACROSS 1982-2099, WHILE MHW AND MOL EVENT CHARACTERISTICS ARE AN AVERAGE OF ALL EVENTS IN THE TWO 24-YEAR PERIODS (1982-2005; 2076-2099). MEAN AND MAXIMUM EVENT FREQUENCY IS A COUNT (DAYS/YEAR) WHILE MEAN EVENT DURATION RELATES TO CONSECUTIVE EXTREME OCCURRENCES. START AND END REFER TO MONTHS THAT THE AVERAGE EVENT WILL OCCUR WITHIN, AND FRACTIONAL COVERAGE IS THE FRACTION OF THE MS THAT WILL EXPERIENCE EXTREMES IN AN AVERAGE YEAR. ....46

TABLE 3: SUMMARY OF AVERAGE LOW INTENSITY ( $SST_{MAX} < SST_{99Q} + 1.5^{\circ}C$ ) AND HIGH INTENSITY ( $SST_{MAX} \geq SST_{99Q} + 1.5^{\circ}C$ ) MHW EVENTS CHARACTERISTICS ACROSS 2076-2099 AND THEIR CORRESPONDING MOL, AOU AND O<sub>2SAT</sub> RESPONSES. MOL AND AOU RESPONSES ARE BASED ON 100 METRES FOR THE MONTHS OF OCTOBER, NOVEMBER AND DECEMBER DURING MOL PEAK INTENSITY. MHW (MOL) ANOMALIES ARE RELATIVE TO  $SST_{99P}$  ([O<sub>2</sub>]<sub>1P</sub>) WITH MEANS REPRESENTING THE AVERAGE VALUE DURING THE EVENT, AND MAXIMUMS THE MOST EXTREME POSITIVE (NEGATIVE) DEVIATION OF SPATIALLY AVERAGED DATA. AOU VALUES REPRESENT AUTUMN AT 100 METRES DEPTH WHILE O<sub>2SAT</sub> VALUES REPRESENT SUMMER AT 0-10 METRES; BOTH ARE RELATIVE TO THE RCP4.5 END-OF-THE-CENTURY (2076-2099) MEAN AND MAXIMUM REPRESENTS THE MOST EXTREME NEGATIVE VALUE. ....70

TABLE 4: SUMMARY OF THE MEAN LOW CATEGORY ( $SST_{MAX} < CATEGORY\ 2$ ) AND HIGH CATEGORY ( $SST_{MAX} \geq CATEGORY\ 2$ ) MHWs ACROSS 2076-2099 AND THEIR CORRESPONDING MOL, AOU AND O<sub>2SAT</sub> RESPONSES. CALCULATIONS FOLLOW THE SAME METHODOLOGY AS FOR THE VALUES IN TABLE 3 EXCEPT DATA IS GROUPED BASED ON ANNUAL MAXIMUM MHW CATEGORY AS OPPOSED TO INTENSITY. ....75



## Figure captions

- FIGURE 1: DEFINITION AND DETERMINATION OF MHWS AFTER HOBDDAY ET AL. (2016, 2018; A) AND FRÖLICHER ET AL. (2018; B). THE LIGHT AND DARK RED LINES SHOW THE SAME OBSERVED SST FOR A LOCATION. THE DASHED BLACK LINES REPRESENT THE CLIMATOLOGICAL 90<sup>TH</sup> PERCENTILE THRESHOLD (FIGURE 1A) AND THE FIXED 99<sup>TH</sup> PERCENTILE THRESHOLD (FIGURE 1B). THE BLUE LINE ON THE LEFT SIDE REPRESENTS THE CLIMATOLOGICAL MEAN WHICH IS USED TO CATEGORISE EVENTS: CATEGORY I IS ONE- TO TWO-TIMES THE DIFFERENCE; CATEGORY II IS TWO- TO THREE-TIMES AND SO FORTH. ON THE LEFT, LABEL A REPRESENTS A HEAT SPIKE (<5 DAYS DURATION) WHILE LABEL B REPRESENTS A CATEGORY III MHW (≥5 DAYS). THE FIXED PERCENTILE THRESHOLD DOES NOT REGISTER THE HEAT SPIKE (A) BUT DOES CAPTURE THE MHW (B). 4
- FIGURE 2: RELEVANT PHYSICAL OCEAN PROCESSES THAT AFFECT THE MIXED-LAYER TEMPERATURE BUDGET. FIGURE REPRODUCED FROM OLIVER ET AL. (2021). 6
- FIGURE 3: MAP OF THE MEDITERRANEAN SEA AND ITS INTERNAL SEAS AND SUB-BASINS. THE THREE REGIONS USED IN THIS STUDY ARE DISPLAYED: NORTHWEST BASIN (NW; RED), ADRIATIC BASIN (AD; BLUE) AND SOUTHEAST BASIN (SE; GREEN). 16
- FIGURE 4: BATHYMETRY (M; BLUE SHADING) AND UPPER 100 METRES AVERAGE VELOCITY (UV; GREY ARROWS) OF THE MS. 19
- FIGURE 5: STUDY AREA JUSTIFICATION FOR THE PROJECT. THE SUBDOMAINS WITHIN THE POLCOMS-ERSEM OUTPUT ARE SHOWN WITH THE MEDITERRANEAN SEA (RED OUTLINE), NORTH SEA (BLUE) AND CANARY CURRENT (GREEN). 20
- FIGURE 6: THREE SUBDOMAINS INCLUDED IN THE POLCOMS-ERSEM MODEL FOR THE CERES PROJECT: THE NORTH SEA AND NORTHEAST ATLANTIC (BLUE), THE CANARY CURRENT (GREEN) AND THE MEDITERRANEAN SEA (RED). 27
- FIGURE 7: ERSEM MODEL SCHEMATIC SHOWING THE WAYS IN WHICH MODEL ELEMENTS INTERACT WITH EACH OTHER. INORGANIC CARBON FLUXES ARE REPRESENTED IN BLUE, NUTRIENT FLUXES IN RED, PREDATOR-PREY INTERACTIONS IN BLACK AND NON-LIVING ORGANIC FLUXES IN GREEN. REPRODUCED FROM BUTENSCHÖN ET AL. (2016). THE FOCUS OF THIS STUDY PREDOMINANTLY CONCERNS THE PELAGIC PART OF THE MODEL SYSTEM. 29

FIGURE 8: SST ANOMALIES AS FRACTIONAL FREQUENCY THROUGHOUT THE PERIOD OF 1982-2005 COMPARING MODEL (RED) AND OBSERVATIONS (CLEAR/BLACK OUTLINE) RELATIVE TO THEIR RESPECTIVE MEANS (VERTICAL DASHED LINE) IN EACH BASIN (NW (A), AD (B) AND SE (C)). VERTICAL LINES DENOTE 99<sup>TH</sup> PERCENTILES IN OBSERVED (BLACK) AND MODEL (RED). 33

FIGURE 9: COMPARING TWO MHW CATEGORISATION SCHEMES. SST<sub>90P</sub> DISPLAYED IN A AND C ALONGSIDE THE NEWLY PROPOSED CATEGORISATION SCHEME FOR SST<sub>99P</sub> IN PANELS B AND D. PANELS A AND B SHOW IDEALISED SCHEMATICS ; C AND D SHOW THE SCHEMES APPLIED TO SATELLITE MAXIMUM SST IN THE NORTH-WEST MEDITERRANEAN BASIN DURING THE 2003 MHW EVENT. LABEL A DENOTES A HEAT-SPIKE THAT EXCEEDS SST<sub>90P</sub> IN A BUT NOT SST<sub>99P</sub> IN B; LABEL B DENOTES A MHW WHICH VARIES IN DURATION AND INTENSITY DEPENDING ON THE METHOD OF DETECTION. PANEL E COMPARES THE TWO SCHEMES BY NORMALISING BOTH TO ZERO (SST MINUS THRESHOLD) SO THAT THE DASHED BLACK LINE REPRESENTS SST<sub>90P</sub> (LIGHT RED LINE) AND SST<sub>99Q</sub> (DARK RED LINE). THE BLUE VERTICAL LINES REPRESENT THE BEGINNING AND END OF OBSERVED BIOLOGICAL IMPACTS. 36

FIGURE 10: OBSERVED (A, E AND I) AND MODEL (B, F AND J) WATER COLUMN TEMPERATURE (°C) IN NW (A-D), AD (E-H) AND SE (I-L) ALONG WITH OBSERVATIONAL-MODEL DIFFERENCES (C, G AND K) AND ROOT MEAN SQUARE ERROR (RSME; D, H AND L). ALL DATA IS RELATIVE TO THE RESPECTIVE MEAN STATE. 39

FIGURE 11: OBSERVED (A, E AND I) AND MODEL (B, F AND J) WATER COLUMN [O<sub>2</sub>] (μMOL L<sup>-1</sup>) IN NW (A-D), AD (E-H) AND SE (I-L) ALONG WITH OBSERVATIONAL-MODEL DIFFERENCES (C, G AND K) AND ROOT MEAN SQUARE ERROR (RSME; D, H AND L). ALL DATA IS RELATIVE TO THE RESPECTIVE MEAN STATE. 41

FIGURE 12: CLIMATOLOGICAL FRACTIONAL AREA OF THE MEDITERRANEAN SEA AND SUB-BASINS IN AN EXTREME STATE OVER THE BASELINE PERIOD (1982-2005) IN SST (A AND C) AND DISSOLVED OXYGEN AT 100 M DEPTH (B AND D) FOR SST<sub>90P</sub> (A) AND [O<sub>2</sub>]<sub>10P</sub> (B), AND SST<sub>99P</sub> (C) AND [O<sub>2</sub>]<sub>1P</sub> (D) USING POLCOMS-ERSEM DATA. (ENTIRE MEDITERRANEAN BASIN – THICK RED AND BLUE LINES; NW – LIGHT GREY; ADRIATIC – MID-GREY; SE – DARK GREY). 42

FIGURE 13: DEFINITION AND DETERMINATION OF A MAJOR OXYGEN LOW (MOL). THE BLUE LINE SHOWS THE OBSERVED [O<sub>2</sub>] AT DEPTH FOR A PARTICULAR LOCATION. THE DASHED BLACK LINE REPRESENTS THE FIXED 1<sup>ST</sup> PERCENTILE THRESHOLD. AUTUMN CLIMATOLOGICAL MEAN IS REPRESENTED IN GREEN AND IS USED TO CATEGORISE EVENTS: CATEGORY I IS ONE- TO TWO-TIMES THE DIFFERENCE; CATEGORY II IS

TWO- TO THREE-TIMES; CATEGORY III IN THREE- TO FOUR-TIMES; CATEGORY IV IS FOUR-TIMES OR ABOVE. LABEL A REPRESENTS A CATEGORY III MOL. 43

FIGURE 14: ANNUAL  $SST_{MEAN}$  (A),  $[O_2]_{(100)MEAN}$  (D),  $SST_{99P}$  (B), AND  $[O_2]_{(100)1P}$  (E) ANOMALIES FOR HISTORICAL (1982–2005), RCP4.5 AND RCP8.5 (2006–2009) WITHIN THE SIMULATED MS AND SUBBASINS. PANELS C AND F DISPLAY EXTREME AGAINST MEAN ANOMALIES FOR FUTURE PROJECTIONS WITH A DASHED BLACK LINE REPRESENTING 1:1 RATIO. PANELS G AND H PRESENT ANNUAL  $[O_2]_{(100)MEAN}$  AGAINST  $SST_{MEAN}$  ANOMALIES AND ANNUAL  $[O_2]_{(100)1P}$  AGAINST  $SST_{99P}$  ANOMALIES. ANOMALIES ARE RELATIVE TO 1982–2005;  $R^2$  VALUES ARE AN AVERAGE ACROSS RCP4.5 AND RCP8.5 PROJECTIONS. 47

FIGURE 15: BASIN AVERAGED FRACTIONAL FREQUENCY OF DAILY MEAN SST (A B AND C) AND DAILY MEAN  $[O_2]_{(100)}$  (D, E AND F) FOR BASELINE PERIOD (BLACK/WHITE; 1982-2005) AND RCP4.5 AND 8.5 (GREEN AND ORANGE, RESPECTIVELY; 2076-2099) RELATIVE TO BASELINE MEAN VALUES. VERTICAL RED LINES SHOW BASELINE  $SST_{99P}$  AND BLUE LINES SHOW BASELINE  $[O_2]_{(100)1P}$ . 52

FIGURE 16: CHANGES TO EXTREMES ( $SST_{P99}$  AND  $[O_2]_{(100)P1}$ ) RELATIVE TO SST AND  $[O_2]_{(100)}$  MEANS. RELATIVE MEAN FOR EACH 24-YEAR PERIOD (HISTORICAL [1982-2005]; RCP4.5 AND RCP8.5 [2076-2099]) IS SUBTRACTED FROM THE RELATIVE P99 (P1) AND EXPRESSED AS THE DIFFERENCE BETWEEN THE TWO PERIODS. RED AREAS INDICATE EXTREMES HAVE CHANGES MORE THAN MEANS. 54

FIGURE 17: HISTORICAL (1982-2005; LEFT SIX PANELS) AND END-OF-THE-CENTURY (RCP4.5; 2076-2099; RIGHT SIX PANELS) MHW CHARACTERISTICS. ‘NORMAL YEAR’ (MEAN) MHW DAYS (A AND C), INTENSITY ABOVE THE 99<sup>TH</sup> PERCENTILE (E AND G) AND CATEGORY (I AND K) ARE DISPLAYED, ALONG WITH MAXIMUM MHW DAYS (B AND D), INTENSITY (F AND H) AND CATEGORY (J AND L) FOR EACH GRID CELL ACROSS EACH 24-YEAR PERIOD. 57

FIGURE 18: HISTORICAL (1982-2005; LEFT SIX PANELS) AND END-OF-THE-CENTURY (RCP4.5; 2076-2099; RIGHT SIX PANELS) LOW OXYGEN EVENT CHARACTERISTICS. ‘NORMAL YEAR’ (MEAN) LOW  $[O_2]$  DAYS (A AND C), MEAN INTENSITY BELOW THE 1<sup>ST</sup> PERCENTILE (E AND G) AND CATEGORY (I AND K) ARE DISPLAYED, ALONG WITH MAXIMUM LOW  $[O_2]$  DAYS (B AND D), MINIMUM INTENSITY (F AND H) AND MAXIMUM CATEGORY (J AND L) FOR EACH GRID CELL ACROSS EACH 24-YEAR PERIOD. 61

FIGURE 19: ‘NORMAL YEAR’ FRACTIONAL AREA OF EACH MS BASIN EXPERIENCING A MHW AND MOL FOR HINDCAST (BLACK; 1982-2005), RCP4.5 (GREEN; 2079-2099) AND RCP8.5 (ORANGE; 2076-2099). 63

FIGURE 20: DEPTH-TIME HOVMOLLER PLOTS (0-200 M) FOR HISTORICAL (1982-2005; A, F, K AND P), RCP4.5 (2076-2099; B, G, L AND Q) AND RCP8.5 (2076-2099; C, H, M AND R) ALONG WITH END-OF-THE-CENTURY CHANGE IN RCP4.5 (D, I, N AND S) AND RCP8.5 (E, J, O AND T) FOR THE MS IN TEMPERATURE ( $^{\circ}\text{C}$ ; A-E),  $[\text{O}_2]$  ( $\mu\text{MOL L}^{-1}$ ; F-J),  $(-1)*\text{AOU}$  ( $\mu\text{MOL L}^{-1}$ ; K-O) AND  $\text{O}_{2\text{SAT}}$  ( $\mu\text{MOL L}^{-1}$ ; P-T). FOR TEMPERATURE AND  $[\text{O}_2]$ ,  $T_{99\text{P}}$  AND  $[\text{O}_2]_{1\text{P}}$  THRESHOLDS ARE REPRESENTED BY ZERO SO THAT YELLOW THROUGH RED SHADING INDICATES EXTREMES. AOU HAS BEEN INVERTED SO THAT THE COLOUR KEY MATCHES  $[\text{O}_2]$  AND  $\text{O}_{2\text{SAT}}$ . 66

FIGURE 21: TIME-MEAN SEASONAL CYCLES (0-200 M) FOR COMPOSITE LOW INTENSITY ( $\text{SST}_{\text{MAX}} < \text{SST}_{99\text{Q}} + 1.5^{\circ}\text{C}$ ; A, C, E AND G) AND HIGH INTENSITY ( $\text{SST}_{\text{MAX}} \geq \text{SST}_{99\text{Q}} + 1.5^{\circ}\text{C}$ ; B, D, F AND H) MHW YEARS FOR RCP4.5 (2076-2099) FOR THE MS IN TEMPERATURE ( $^{\circ}\text{C}$ ; A AND B),  $[\text{O}_2]$  ( $\mu\text{MOL L}^{-1}$ ; C AND D),  $(-1)*\text{AOU}$  ( $\mu\text{MOL L}^{-1}$ ; E AND F) AND  $\text{O}_{2\text{SAT}}$  ( $\mu\text{MOL L}^{-1}$ ; G AND H). FOR TEMPERATURE AND  $[\text{O}_2]$ ,  $T_{99\text{P}}$  AND  $[\text{O}_2]_{1\text{P}}$  THRESHOLDS ARE REPRESENTED BY ZERO SO THAT YELLOW THROUGH RED SHADING INDICATES EXTREMES;  $(-1)*\text{AOU}$  AND  $\text{O}_{2\text{SAT}}$  ARE RELATIVE TO THE 2076-2099 MEAN. 72

FIGURE 22: TIME-MEAN SEASONAL CYCLES (0-200 M) FOR COMPOSITE LOW CATEGORY ( $\text{CATEGORY} < 2$ ; A, C, E AND G) AND HIGH CATEGORY ( $\text{CATEGORY} \geq 2$ ; B, D, F AND H) MHW YEARS UNDER RCP4.5 (2076-2099) FOR THE MS IN TEMPERATURE ( $^{\circ}\text{C}$ ; A AND B),  $[\text{O}_2]$  ( $\mu\text{MOL L}^{-1}$ ; C AND D),  $(-1)*\text{AOU}$  ( $\mu\text{MOL L}^{-1}$ ; E AND F) AND  $\text{O}_{2\text{SAT}}$  ( $\mu\text{MOL L}^{-1}$ ; G AND H). FOR TEMPERATURE AND  $[\text{O}_2]$ ,  $T_{99\text{P}}$  AND  $[\text{O}_2]_{1\text{P}}$  THRESHOLDS ARE REPRESENTED BY ZERO SO THAT YELLOW THROUGH RED SHADING INDICATES EXTREMES;  $(-1)*\text{AOU}$  AND  $\text{O}_{2\text{SAT}}$  ARE RELATIVE TO THE 2076-2099 MEAN. 76

# 1 Introduction

Oceans play a significant role in regulating climate sequestering more than 90% of anthropogenic heat (Cheng et al., 2019). The ocean experiences discrete periods of anomalously warm conditions, termed marine heatwaves (MHWs; Hobday et al., 2016), and since industrialisation, occurrences of the most intense events have increased 20-fold as a result of anthropogenic influences (Laufkötter et al., 2020). Negative biological effects of MHWs include fish biodiversity changes (Pearce and Feng, 2013; Wernberg et al., 2013), destruction of marine flora (Rogers-Bennett and Catton, 2019, Marbà and Duarte, 2009) and mass mortality in sessile marine organisms (Garrabou et al., 2009; Oliver et al., 2018, 2017) and sea birds (Jones et al., 2018). Significant economic losses result from long ecosystem recovery timescales, for example, scallop fisheries in Western Australia were closed for up to 5 years following a MHW in 2011 (Caputi et al., 2019).

Oceanic warming from climate change affects ocean biogeochemistry globally (Gruber, 2011) and contributes to ocean deoxygenation (Andrews et al., 2013). Dissolved oxygen is fundamental for aerobic organisms and plays a key role in the biogeochemical cycling of carbon, nitrogen and phosphorus which are essential for life (Keeling et al., 2010a). The global mean concentration of dissolved oxygen (herein  $[O_2]$ ) has declined in the oceans by 2% over the past 50 years (Schmidtko et al., 2017) with an expansion in the size of oxygen minimum zones (OMZs) by 3-8.3% (Bindoff et al., in press). Business-as-usual CMIP6 models show a continuing trend with further declines by up to 3-4% in  $O_2$  content between 100 and 600 metres depth by 2100 (Kwiatkowski et al., 2020). These  $O_2$  changes are attributed primarily to reduced solubility in the surface ocean and increased stratification and respiratory oxygen demand in the subsurface, all of which are caused by rising temperatures on decadal and centennial timescales (Oschlies et al., 2018).

The impacts of MHWs on ocean biogeochemistry remain unclear and yet, no research has attempted to quantify the response of [O<sub>2</sub>] following these events. The Mediterranean region is a climate change hotspot and is warming at a rate 20% faster than the global mean (Collins et al., n.d.; Giorgi, 2006). The basin has been severely affected by MHWs including a significant event in 2003 that had substantial ecosystem impacts (Darmaraki et al., 2019a; Garrabou et al., 2009). Physical circulation models show the MS remaining well-oxygenated (>150 μmol L<sup>-1</sup>) up to 2100 and beyond (Powley et al., 2016) but a gap remains in the literature in considering deoxygenation in relation to short term physical and biogeochemical extremes. Here I will explore how MS MHWs are likely to change by the end of the century and identify for the first time their signature in dissolved oxygen by using a high resolution (0.1°) physical-biogeochemical model.

## 2 Literature review

### 2.1 Marine heatwaves

#### 2.1.1 Definitions

In recent years MHWs have received ever-growing interest with the majority of studies focusing on the intensity, spatiotemporal extent and biological impacts of events. There are two established methodologies that are frequently used within the scientific community to define MHWs; both classify events based on the exceedance of sea surface temperature (SST) above a relative percentile-based threshold. Typically, percentiles are calculated over time for a particular location (e.g. on a grid cell basis) which accounts for regions that differ in climate sensitivity and variability (Frölicher et al., 2018).

MHWs are defined as discrete and prolonged, anomalously warm oceanic events (Hobday et al., 2016). The severity of an event is based on its intensity, duration and spatial extent. Hobday et al. (2016) suggest that thirty years of data provides an historic distribution of SST that can be used to produce the climatological 90<sup>th</sup> percentile threshold. To ensure a large enough sample size for percentiles, the method requires use of an 11-day running window and monthly smoothing. In order to qualify as a MHW, local maximum SST values must persist above the climatological 90<sup>th</sup> percentile threshold ( $SST_{90P}$ ) for  $\geq 5$  days. As a result of using a seasonally varying threshold, the method allows detection of anomalously warm water all year round. Hobday et al. (2016)'s method also categorises MHWs by dividing the difference between the maximum SST and threshold value by the difference between the threshold value and climatological mean (*Figure 1a*). For example, on the 14<sup>th</sup> of June during the 2003 North-West Mediterranean Sea MHW, regional maximum SST peaked at 4.38°C above  $SST_{90P}$  relative to a 1982-2016 baseline period.

Because the maximum SST recorded during the event was greater than or equal to two times the difference between the climatological mean and 90<sup>th</sup> percentile, the event falls into category II – strong (Hobday et al., 2018).

Frölicher et al. (2018) developed a simpler approach to determine MHW events which is based on SST exceeding a fixed 99<sup>th</sup> percentile (SST<sub>99P</sub>; a one-in-hundred-day event; *Figure 1b*). The threshold should be calculated using a baseline period of 35 years. In developing this method, Frölicher et al. (2018) note that the majority of determined MHWs are longer than 5 days and therefore do not exclude events that are shorter than this duration. A significant difference of this method over the method proposed by Hobday et al. (2016) is that only summertime events are captured and cold season events are ignored. Frölicher et al. (2018) classify the severity of events based on their duration and intensity as well as their cumulative mean intensity. Cumulative mean intensity is the average intensity of an event multiplied by the event duration and is similar to the degree heating weeks (DHW) metric.

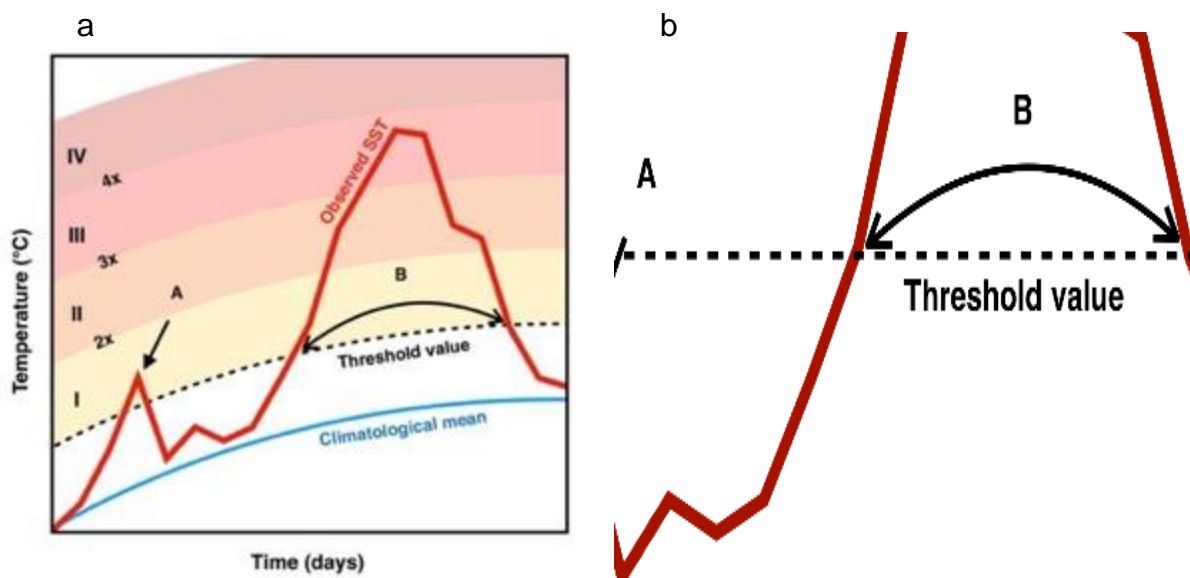


Figure 1: definition and determination of MHWs after Hobday et al. (2016, 2018; a) and Frölicher et al. (2018; b). The light and dark red lines show the same observed SST for a location. The dashed black lines represent the climatological 90<sup>th</sup> percentile threshold (Figure 1a) and the fixed 99<sup>th</sup> percentile threshold (Figure 1b). The blue line on the left side represents



*the climatological mean which is used to categorise events: category I is one- to two-times the difference; category II is two- to three-times and so forth. On the left, label A represents a heat spike (<5 days duration) while label B represents a category III MHW ( $\geq 5$  days). The fixed percentile threshold does not register the heat spike (A) but does capture the MHW (B).*

The DHW metric, developed by the U.S. National Oceanic and Atmospheric Administration Coral Reef Watch program, aims to predict severity of coral bleaching (Liu et al., 2014). It combines twelve weeks duration and temperature intensity into one measurement of thermal stress and uses an absolute threshold of 1°C above the maximum monthly mean (MMM) of SSTs. The measure is a positive only anomaly and is the cumulative exceedance in SST above the threshold across the most recent twelve weeks. For example, one week of 1°C above the MMM and two weeks of 3°C above the MMM over a total of twelve weeks would contribute a total of 7°C-weeks. It is used in tropical regions either instead of the definition in Hobday et al. (2016) (e.g Hughes et al., 2018) or alongside it (e.g Benthuisen et al., 2018). Extreme positive anomalies in SST can also be described in terms of thermal displacement for mobile marine organisms. Thermal displacement is the distance that must be covered if a consistent temperature is to be maintained and intense positive thermal anomalies are to be avoided (Jacox et al., 2020). However, I will use neither DHW metric or thermal displacement in my analysis and focus instead on the two methods of MHW detection (SST<sub>90P</sub> and SST<sub>99P</sub>).

## 2.1.2 Drivers

### 2.1.2.1 Local processes

MHWs are driven by local ocean processes in the surface mixed layer that are modulated by teleconnection processes and large-scale climate modes. *Figure 2* outlines the relevant local-scale physical ocean processes that contribute to the temperature budget of the mixed layer. Surface level heating creates stability in the surface layers of the ocean

inhibiting mixing and downward advection due to density stratification (Coma et al., 2009; Sparnocchia et al., 2006). A stratified water column increases entrainment by reducing vertical diffusion and vertical advection (Hobday et al., 2016). A MHW results from these combined processes contributing to a positive thermal anomaly strong enough to exceed a relative threshold. For example, low advection and wind speeds may reduce horizontal velocity, vertical advection and radiative heat loss at the base of the mixed layer causing it to shoal and enhancing entrainment. Should these conditions coincide with a high net air-sea heat flux then an MHW could develop (Gao et al., 2020; Oliver et al., 2021).

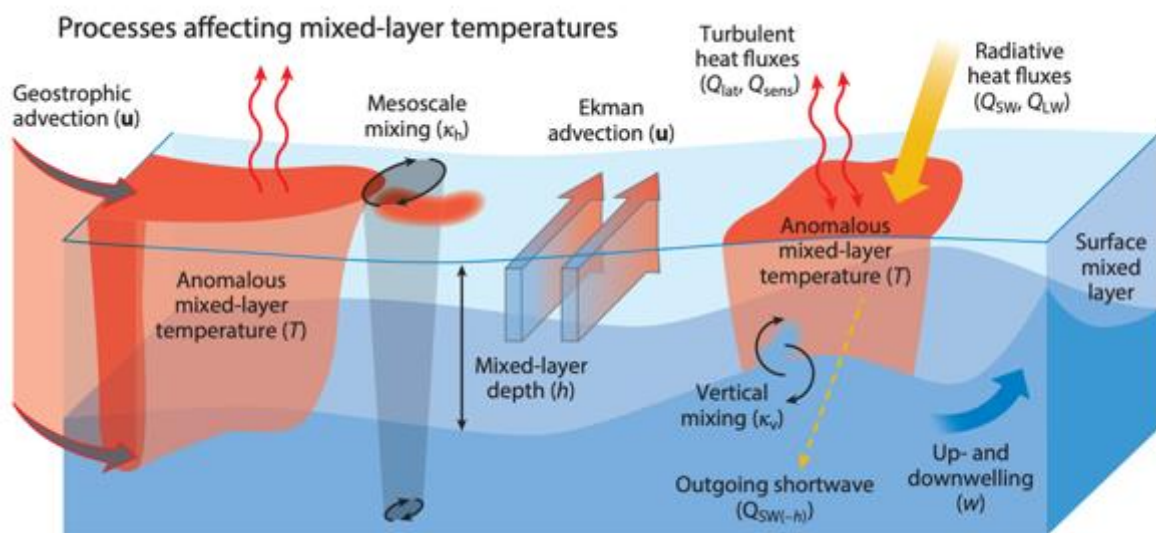


Figure 2: Relevant physical ocean processes that affect the mixed-layer temperature budget. Figure reproduced from Oliver et al. (2021).

### 2.1.2.2 Natural climate variability

Teleconnections are climatic links between regions that are separated geographically but exhibit fluctuations in atmospheric conditions. They are known to contribute to local processes that cause MHWs (Holbrook et al., 2019). For example, the Northeast Pacific MHW, known colloquially as ‘the blob’, is the longest event on record lasting from 2013-

2015 and had devastating impacts for wildlife (Di Lorenzo and Mantua, 2016). A positive phase of the North Pacific Oscillation (NPO), causing high atmospheric pressure in the Gulf of Alaska and low pressure in the central Pacific, initially led to strong positive SST and sea-level pressure (SLP) anomalies. These conditions persisted in 2015 because of the Aleutian Low (AL). High SLP inhibited the surface heat flux along with horizontal and vertical advection resulting in SSTs that were 3°C higher than normal (Bond et al., 2015). Likewise, the 2012 Gulf of Maine MHW was instigated by wintertime high pressure in the region caused by a northward shift of the Jet Stream (Chen et al., 2014). These conditions constrained latent and sensible heat fluxes from the surface of the ocean by reducing wind speeds and increasing air temperatures, propagating conditions favourable for a MHW in the early summer.

Large-scale climate modes likely affect MHWs despite evidence remaining unclear for many events (Holbrook et al., 2019). The most severe MHW in terms of intensity occurred in Western Australia in 2011, with temperatures elevated by 4.89°C above a seasonally varying threshold (Hobday et al., 2018). Here, El Niño Southern Oscillation (ENSO) is the key driver of interannual variability (Holbrook et al., 2019). MHWs in this region are known as Ningaloo Niño events and are associated with the negative phase of ENSO. The Western Australia MHW in 2011 coincided with a strong La Niña event (Holbrook et al., 2019).

### 2.1.3 MHWs under climate change

MHWs have increased in frequency and intensity by 17 and 34% respectively over the past century, with 80% attributable to human-induced warming via rising SSTs (Frölicher et al., 2018; Oliver et al., 2018). Prior to industrialisation, Earth System Models (ESMs) show MHWs lasting on average 11 days with an intensity of  $SST_{99P}+0.4^{\circ}C$

(Frölicher et al., 2018). With current warming at 1°C, these have risen to 25 days and SST<sub>99P</sub>+0.8°C, respectively. Under scenarios of 1.5°C, 2.0°C and 3.5°C of warming, the number of MHW days each year is expected to increase by a factor of 16, 21 and 41, respectively by the end of the century, with spatial extent expanding by a factor of 21 globally, and events lasting for an average 112 days (Frölicher et al., 2018).

MHWs have devastating impacts on foundational low-trophic taxa such as corals, kelps and seagrasses (Smale et al., 2019), and can result in regional biodiversity shifts (Wernberg et al., 2013). Transitions from kelp forests to echinoid barrens are reported following an MHW in Northern California (Rogers-Bennett and Catton, 2019), while high temperatures have exterminated sea urchins in the Levantine basin of the Mediterranean Sea (Yeruham et al., 2015). On top of this, tropicalisation effects can result in adventitious fish populations migrating poleward (Pearce and Feng, 2013). Ecological recovery times from events are slow and may take decades (Garrabou et al., 2001); predicted changes in MHW frequency and intensity over the remainder of the century will likely have cumulative effects for regions sensitive to MHWs and climate change.

#### 2.2.4 Biogeochemical effects

Extreme SSTs can result in changes to biogeochemistry, including effects on dissolved oxygen and primary production. Low oxygen conditions (63-80  $\mu\text{mol l}^{-1}$ ) coincided with elevated temperatures and likely contributed to mortality of 11 fish species at Cocos Islands in the Indian Ocean from 2007-2009 (Hobbs and McDonald, 2010). Several periods mortality occurred during warm and calm weather conditions and elevated SSTs (33-35°C). Warm temperatures affect metabolic rates of taxa often resulting in greater O<sub>2</sub> requirements (Kipson et al., 2012; Previati et al., 2010). Furthermore, MHWs can affect chlorophyll-a levels, for instance with low latitude regions that experience MHWs

showing suppressed levels of chlorophyll-a, while high latitude regions display elevated levels (Hayashida et al., 2020).

## 2.2 Ocean deoxygenation

### 2.2.1 Fundamental controls on dissolved oxygen

#### 2.2.1.1 Oxygen cycle

Air-sea gas exchange ( $Q_F$ ) couples the inventories of oceanic and atmospheric oxygen ( $O_2$ ) and can be expressed as follows:

$$Q_F = k_\omega \alpha (\rho O_2^{atm} - \rho O_2^{ocean}) \quad (2)$$

where  $k_\omega$  is the gas transfer velocity and  $\alpha$  is  $O_2$  solubility in seawater, while  $\rho O_2^{atm}$  and  $\rho O_2^{ocean}$  represent the partial pressures of  $O_2$  in the atmosphere and ocean, respectively. Exchange between the two inventories dominates the surface  $O_2$  signal maintaining concentrations close to saturation ( $O_{2sat}$ ) in the surface mixed layer. Seawater  $O_2$  solubility ( $\alpha$ ) is largely controlled by temperature and salinity. In the upper 1000 metres of the ocean ~50% of the observed  $O_2$  loss over the last 50 years can be attributed to rising oceanic temperatures reducing the solubility of  $O_2$  (Schmidtko et al., 2017).

$[O_2]$ -rich surface water is transported into the interior of the ocean via mixing and advection processes referred to as ‘ventilation’ (e.g. Keeling et al., 2010). The deep ocean is primarily ventilated by deep-water formation which occurs annually at high latitudes during winter when surface waters become cooler and denser. Biology affects  $O_2$  through photosynthetic production in the photic zone and respiratory consumption via the remineralisation of organic matter throughout the water column. Where light penetrates

and sufficient nutrients are available, photosynthesis may exceed respiration resulting in  $O_2$  exceeding  $O_{2sat}$  (Giomi et al., 2019). Warmer oceanic temperatures result in greater rates of consumptive remineralisation.

#### *2.2.1.2 Stratification*

Stratification describes layers within a body of water that have varying densities due to differences in temperature and salinity (Capotondi et al., 2012). Less dense water such as riverine input may lead to surface waters becoming more stratified by reducing salinity. Similarly, warming will also contribute to decreasing density. Lower surface densities relative to the interior density inhibit downward advection causing the mixed layer to shoal, hindering ventilation and the upwelling of oxygen-deficient waters. In opposition, upwelled waters are nutrient-rich and drive surface primary production, increasing the export flux of organic carbon and depleting interior  $[O_2]$ . Inhibited exchange rates between the surface and interior ocean are generally the overriding control on the subsurface  $[O_2]$  signal in model experiments (Keeling et al., 2010b). However, Frölicher et al. (2009) determined a 50% contribution from solubility effects in simulated deoxygenation from 1850 to 2100. Since the 1960s, statistically significant increases in thermal stratification of the upper 200 metres of the water column are observed in 40% of the ocean (Yamaguchi and Suga, 2019).

While high latitude regions of deep-water formation rarely stratify and the mid-latitudes experience seasonal stratification in calm summertime conditions, equatorial and tropical waters can be permanently stratified. The physical and biological controls on  $[O_2]$  result in an  $O_2$  minimum at the base of the thermocline. The most prominent  $[O_2]$  minima are found in the eastern regions of tropical oceans where ventilation is low and organic matter transport high. These areas are known as OMZs (Stramma et al., 2008) and

account for a significant proportion of hypoxic ( $[O_2] < 62 \mu\text{mol l}^{-1}$ ) conditions in the open ocean (Stramma et al., 2008).

## 2.2.2 Drivers

### 2.2.2.1 Natural climate variability

Substantial changes to the oxygenation of the oceans occur because of natural variability at interannual and interdecadal timescales as well as in response to long term external forcing. For example, fluctuating  $[O_2]$  concentrations in the surface and subsurface of the water column in the North Atlantic and North Pacific oceans correlate with the NAO and the Pacific Decadal Oscillation (PDO), respectively. The NAO accounts for 30% of  $[O_2]$  variability in the North Atlantic in surface and subsurface waters (Frolicher et al., 2009). Similarly, suboxic regions of the Pacific ocean between  $10^\circ\text{N}$ - $10^\circ\text{S}$  expanded by 7% over the course of 50 years during a positive PDO phase (Duteil et al., 2018). The PDO causes trade winds to slow, reducing surface turbulence in a region where advection is the primary ventilation process. Finally, Frolicher et al. (2009) compared model simulations with and without the external forcing of volcanism to demonstrate the cooling effect eruptions have on the atmosphere enhancing  $[O_2]$  solubility in the oceans.

### 2.2.2.2 Climate change

The major controls on  $[O_2]$  such as mixing processes, respiration rates and solubility are all affected by rising temperatures. Since 1960, the oceanic  $O_2$  reservoir has decreased by  $4.8 \pm 2.1$  petamoles (2%), with the direct thermal effect accounting for 15% of this decline (Schmidt et al., 2017). The upper ocean (100-600 metres) is largely affected by changes to solubility and remineralisation rates, while the deep ocean is affected by the weakening of large-scale ventilation processes. Multi-model analysis shows significant differences between models in the recent past and towards the end of the 21<sup>st</sup> century

(Frolicher et al., 2009). Disentangling natural variability from anthropogenic influence has proved difficult. External forcing has been detected within observed declining  $[O_2]$  levels in the Atlantic and Pacific basins (Andrews et al., 2013), with similar anthropogenically-forced trends expected to emerge in the Indian Ocean by 2030 (Long et al., 2016).

By the year 2100, model studies predict between a further 1-7% decline in the oceanic reservoir of  $[O_2]$  (Bopp et al., 2013; Kwiatkowski et al., 2020; Schmidtko et al., 2017). Climate models are conservative in terms of the  $[O_2]$  signal in response to warming when compared with observations, implying that future trends may be underestimated (Andrews et al., 2013). Furthermore, climate models have been unable to consistently reproduce the observed expansion of tropical OMZs (e.g. Stramma et al. 2012). Recent work has highlighted issues in model parameterisation of C:N ratios, where inclusion of  $\rho CO_2$ -sensitive ratios drives biogeochemical  $[O_2]$  utilisation through increased export rates (Andrews et al., 2017).

#### *2.2.2.3 Organic pollution in coastal systems*

Naturally, precipitation erodes terrestrial organic matter that is transported via rivers into the ocean providing nutrients for marine primary production. Further, agricultural fertilisers leach into rivers and wastewater is often poorly managed resulting in anthropogenic enrichment of coastal waters. Nitrate, phosphate and micronutrients are essential components for algal production and excessive transport into the ocean causes eutrophication. Enhanced primary production increases the export flux of organic matter and a greater degree of remineralisation means more  $[O_2]$  is consumed in the water column (Rabalais et al., 2010). Deoxygenation occurs and hypoxic or anoxic bottom waters in the coastal zone may ensue depending on the strength of the export flux. Over



500 coastal sites have reported hypoxia globally since 1950 while only 10% of these had previously recorded such levels (Diaz and Rosenberg, 2008). Increases in nitrate and phosphate levels by 90% and 67% from 1995-2005 in Bolinao, Philippines, a region of dense aquaculture (San Diego-McGlone et al., 2008). Here, anthropogenic eutrophication contributed to an algal bloom and mass fish kill in 2002 that incurred economic costs equivalent to \$9 million.

### 2.2.3 Impacts

#### 2.2.3.1 Biogeochemical impacts

At certain thresholds, deoxygenation can transition the ocean into an anaerobic state and affect the biogeochemical cycling of essential elements for life such as N, P and Fe (Wright et al., 2012). Once  $[O_2]$  is at low levels or depleted, bacteria more commonly utilise other electron acceptors such as nitrate in the breakdown of organic matter, a process known as denitrification (Bianchi et al., 2012). Remineralisation via denitrification forms  $N_2$  which is not accessible for the majority of organisms. Therefore, high rates of denitrification provide a sink of bioavailable N, a limiting nutrient in the oceans, and will reduce the capacity of the biological pump. Additionally, the potent greenhouse gas nitrous oxide ( $N_2O$ ) is a product of denitrification (Bange, 2006). Observational and modelling evidence of depositional environments indicates that denitrification beneath high nutrient and low  $[O_2]$  areas (e.g. OMZs) removes N 3-times faster than in sediments of highly oxygenated regions (Bohlen et al., 2012). The same study showed that OMZs cause 10% of global oceanic  $N_2O$  production despite accounting for 1% of the global ocean volume. However, OMZs are strongly stratified regions of the ocean, and hypoxia- and suboxia-induced  $N_2O$  must first reach atmosphere through air-sea gas exchange to contribute to greenhouse warming. Increased stratification under climate change may act

to inhibit this process, with models showing a 4-12% decrease in oceanic N<sub>2</sub>O emissions by 2100 (Martinez-Rey et al., 2015).

Anthropogenic inputs have also altered the biogeochemical cycling of P in coastal systems. The residence time of P in these regimes is lengthened by bacterial retention and remobilisation processes in that they are recycled from sediments and within the water column (Paytan and McLaughlin, 2007). In hypoxic conditions, P remobilisation processes are enhanced by sulphate and Fe reduction in sediments. A model study of Xiamen Bay, China, shows this process can result in a continuous release of P (Pan et al., 2019). This recycling of P from sediments acts as a positive feedback loop by driving primary production and further remineralisation, a process linked with oceanic anoxic events during the Mesozoic era (Jenkyns, 2010).

#### *2.2.3.1 Biological impacts of long-term changes*

The conventional definition of hypoxia ( $<62 \mu\text{mol l}^{-1}$ ), originally used in the context of fisheries collapse (Renaud, 1986), does not apply universally for all marine taxa. Physiological tolerances to low oxygen conditions vary significantly, with lethal and sublethal impacts observed in 10% of species (mainly crustaceans and fish) at  $143 \mu\text{mol l}^{-1}$  and  $156 \mu\text{mol l}^{-1}$ , respectively (Vaquer-Sunyer and Duarte, 2008). Impacts include impairment of the spatial ranges of species sensitive to low oxygen conditions by the vertical expansion of OMZs (Stramma et al., 2008). Habitat compression forces species such as marlin, billfishes, tuna and sharks (Gilly et al., 2013; Vedor et al., 2021) closer to the surface enhancing the likelihood of overfishing.

### *2.2.3.1 Biological impacts of low oxygen events*

Along with long-term deoxygenation, periodic low oxygen events negatively impact marine biology. Unprecedented anoxic conditions were observed in the Californian Current system off the coast of central Oregon between June and October, 2006 (Chan et al., 2008). The occurrence was driven by upwelling favourable winds, caused a mass mortality event in macroscopic benthic invertebrates and coincided with a growth of bacterial mats in shallower waters (<50 metres). Typically, there is an OMZ in this regime at a depth greater than 600 metres, but anoxia in waters less than 50 metres had not previously been recorded (Chan et al., 2008).

Low oxygen events often appear to be triggered by extreme temperatures. For example, in the Bay of Santa Catarina (Brazil) in 2020, a 9-day MHW with SSTs of 30°C cooccurred with the first regional record of hypoxia (Brauko, 2020). Observed phosphate levels since 1994 had been increasing as a result of anthropogenic enrichment while mean [O<sub>2</sub>] levels decreased from >267  $\mu\text{mol l}^{-1}$  to ~220  $\mu\text{mol l}^{-1}$ . The synergistic effects of extreme temperatures and low oxygen affected microbenthic and phytoplanktonic biodiversity (Brauko, 2020).

## 2.3 The Mediterranean Sea

### 2.3.1 Physical and biogeochemical characteristics

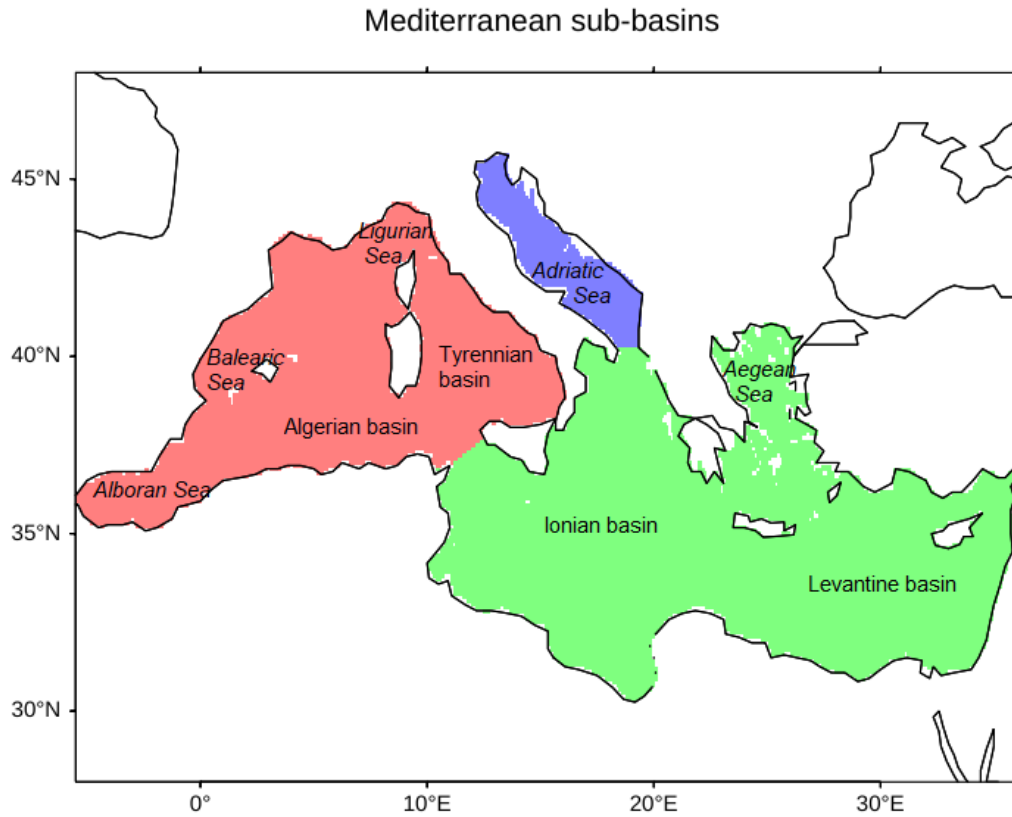


*Figure 3: Map of the Mediterranean Sea and its internal seas and sub-basins. The three regions used in this study are displayed: Northwest basin (NW; red), Adriatic basin (AD; blue) and Southeast basin (SE; green).*

The Mediterranean region is a “hotspot” for climate change due to its semi-enclosed nature and SSTs are warming at rate a 20% faster than the global mean under climate change (Giorgi, 2006; Lionello and Scarascia, 2018). The MS is socioeconomically important for fisheries and tourism (Russo et al., 2019). Therefore, it is essential to understand the biogeochemistry of the basin and how it might be affected by anthropogenic warming in order to mitigate potential impacts, especially in cases of extreme events.

There is an east-west disparity in atmospheric and sea surface temperatures with warmer SST in SE ( $\sim 20.5^{\circ}\text{C}$ ) relative to NW where SST averages  $\sim 19^{\circ}\text{C}$  (Nykjaer, 2009). The temperature difference results in an east-west salinity-controlled density gradient driven by surface heating and evaporation. This phenomenon is the main driver of convection in SE as high evaporation creates dense saline surface waters that sink. Intermediate-water formation events occur sporadically in the eastern basin having previously been observed in the Adriatic. They have been observed to raise SE intermediate-water  $[\text{O}_2]$  by  $5 \mu\text{mol L}^{-1}$  (Powley et al., 2016 and references therein). Intermediate-water formation occurred in the Aegean Sea at the end of the 1980s leading to changes in the properties of intermediate water throughout the MS. MS deep waters have become warmer and more saline at a rate of  $0.04^{\circ}\text{C}$  and  $0.015 \text{ PSU}$  per decade over the last 40 years (Borghini et al., 2014). Mediterranean surface currents flow from the Atlantic Jet (AJ) through the southern NW to SE via the Strait of Sicily, with a continuing cyclonic flow throughout SE, AD and back through NW (El-Geziry and Bryden, 2014; see *figure 4*).

Throughout the seasonal cycle, the MS typically undergoes vertical mixing during winter, spring algal blooms in regions of nutrient enrichment, and water column stratification in summer that weakens throughout autumn. Stratification means that a feature of the Northwest basin is an oxygen minimum layer between 200 – 1300 metres depth (Coppola et al., 2018). In the winters of 2005 and 2006, NW deep convection resulted in an increase of  $24 \text{ mol L}^{-1} \text{ O}_2$  in this oxygen minimum layer in the region (Coppola et al., 2018). Models show that 88% of total annual  $[\text{O}_2]$  uptake of atmospheric oxygen in NW occurs during wintertime mixing (Ulses et al., 2020). This resupplies the surface layer with nutrients

and O<sub>2</sub> resulting in a stronger algal bloom in spring as vertical mixing weakens and temperatures warm (Bernardello et al., 2012; Taylor and Ferrari, 2011).

Generally, the MS is oligotrophic and nutrient input is low. The AJ is the most significant input of water and nutrients (N and P) into the MS entering via the Gibraltar Strait at 0-200 metres depth (Powley et al., 2017). During periods of strong westerly winds, chlorophyll concentrations are 0.5 mg m<sup>-3</sup> greater than the regional mean in the Alboran Sea (Macias et al., 2007). Chlorophyll concentrations are elevated by westerly winds because of strengthened eastern boundary upwelling in the Atlantic bringing nutrient-rich waters to the surface from depth (Macias et al., 2007). Significant biogeochemical disparities between regions within the MS arise from the input of the AJ. Surface rates of primary production are 2-3 times higher in NW relative to SE, with rates declining eastwardly with increasing oligotrophy and distance from the AJ (Turley et al., 2000). Primary productivity is equally high in AD as in NW with anthropogenic enrichment from riverine input as the main driver (Turley et al., 2000).

Simulations show that a deep chlorophyll maximum (DCM) is present in 75% of the open-sea MS (Macías et al., 2014). A DCM has been observed in many regions (e.g. Estrada et al., 1993; Kimor et al., 1987). Recent work suggests this phenomenon is caused by light-dependent zooplankton consuming organic matter at a rate that decreases with depth within the photic zone (Moeller et al., 2019). The Depth of the DCM varies between NW (60-110 metres) and SE (100-150 metres), and signifies a peak in photosynthesis (Turley et al., 2000). As a result, maximal climatological [O<sub>2</sub>] levels in each basin (between 1960-2011) mirror the depth of the DCM, with a shallower, more pronounced positive deviation observed in NW compared with SE (Mavropoulou et al., 2020).

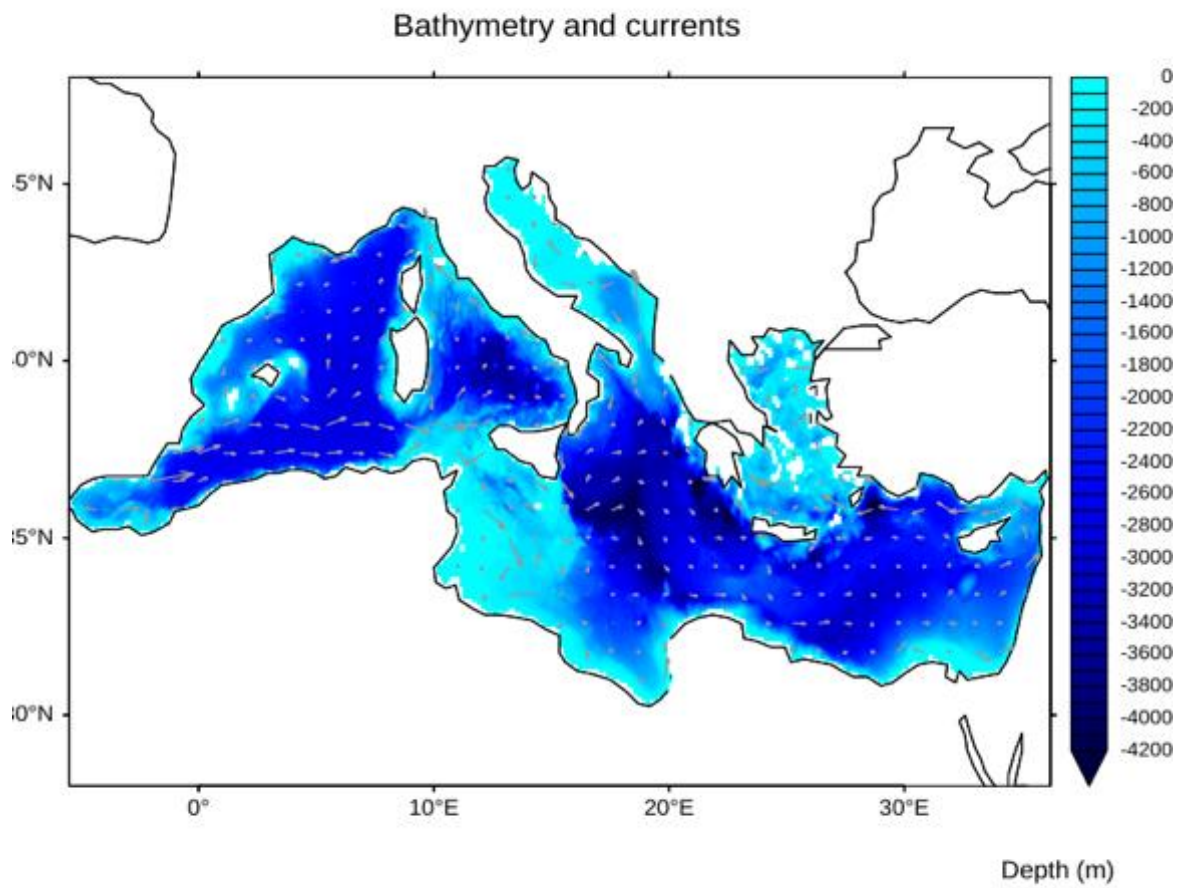


Figure 4: Bathymetry (m; blue shading) and upper 100 metres average velocity (uv; grey arrows) of the MS.

### 2.3.2 Observed extremes

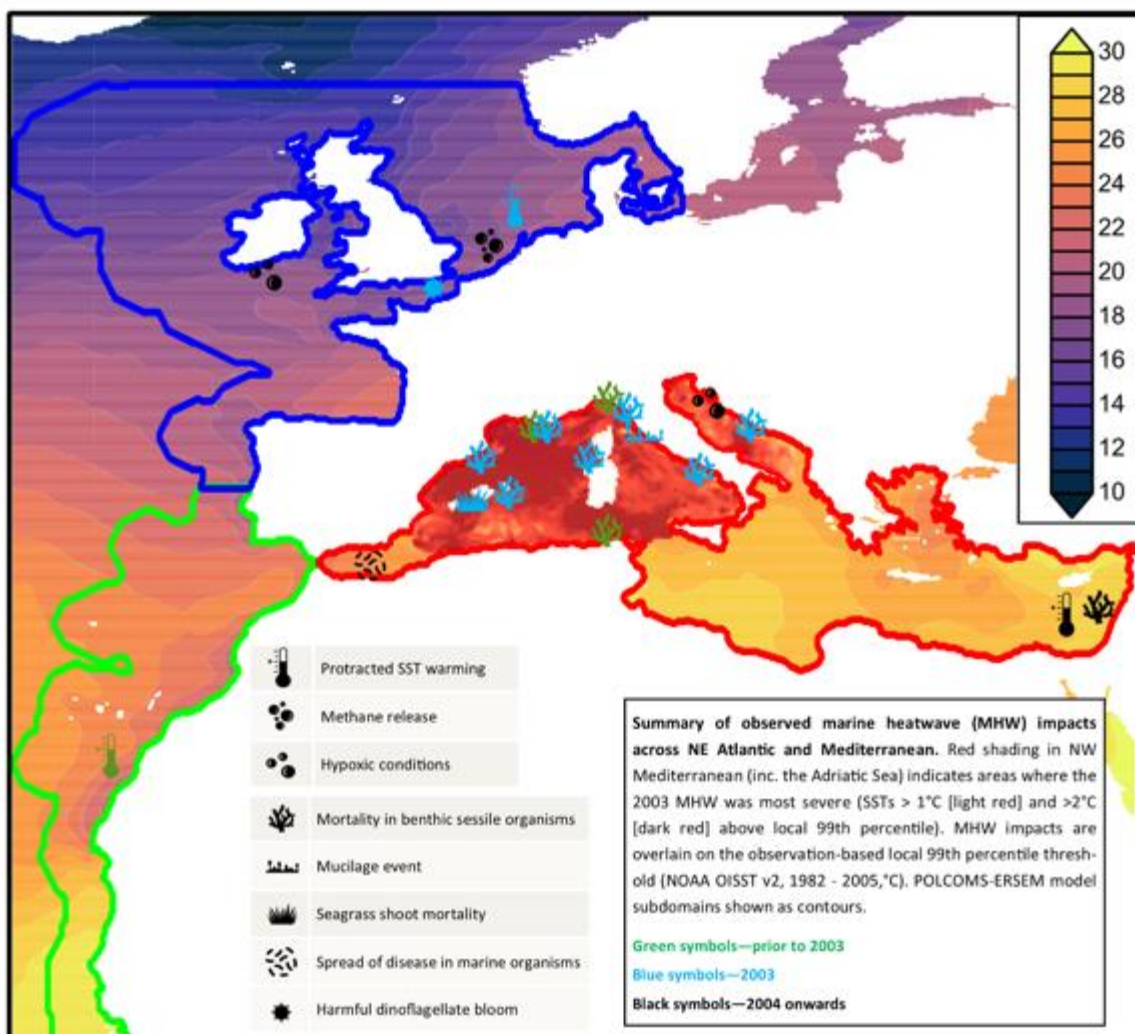


Figure 5: Study area justification for the project. The subdomains within the POLCOMS-ERSEM output are shown with the Mediterranean Sea (red outline), North Sea (blue) and Canary Current (green).

#### 2.3.2.1 MHWs

In the MS, SSTs have increased by 0.24°C per decade in the western basin and 0.42°C per decade in the eastern basin (Skiriris et al., 2012). MS MHW events increased in frequency, intensity and spatial extent between 1982-2017 (Darmaraki et al., 2019a). Between 1982-2017, events in the basin lasted on average 15 days, had a mean intensity of 0.6°C above SST<sub>99P</sub> threshold, and a maximum spatial coverage of 39% (Darmaraki et al.,



2019a). Reports of MS MHWs exist in the literature for events in 1999 (Cerrano et al., 2000), 2003 (Garrabou et al., 2009), 2006 (Marbà and Duarte, 2009), 2011 (Kružić et al., 2014; Yeruham et al., 2015), 2012 (Darmaraki et al., 2019a) and 2015 (Darmaraki et al., 2019a; Rubio-Portillo et al., 2016), with more recent events occurring in 2019 and 2020. The Northwest Mediterranean MHW of 2003 was the first well-documented, ecologically catastrophic event (Garrabou et al., 2009). The MHW is determined to be a category II event that endured for 31 days (Hobday et al., 2018).

Mediterranean MHWs can have repercussions for ocean fauna and flora with biological impacts predominantly observed in low motility organisms. MHW events have caused mortality in seagrass shoots (Marbà and Duarte, 2010) and benthic invertebrates including gorgonians (Cerrano et al., 2000; Garrabou et al., 2009), sponges (Rubio-Portillo et al., 2016), corals (Kružić et al., 2014), bryozoans (Cocito and Sgorbini, 2014) and echinoderms (Yeruham et al., 2015). Furthermore, MHWs coincide with mucilage events which instigate erect coral biomass detachment (Schiaparelli et al., 2007) and appear to promote proliferation and spread of pathogens among sessile organisms (Garrabou et al., 2001). In the 2003 event, necrosis was recorded in organisms down to 50 metres depth (Linares et al., 2005). These impacts will inevitably have unforeseen consequences for mobile fractions of ecological communities.

MHWs in the MS occur during summer and are driven by persistent high atmospheric pressure and sea-level pressure anomalies accompanied by high air temperatures, reduced wind speeds and low cloud cover (Cerrano et al., 2000; Holbrook et al., 2019; Olita et al., 2007). Low winds prevent atmospheric and surface layer turbulence which inhibits the air-sea heat flux, causing a shoaling of MLD. Heat from shortwave and longwave radiation is absorbed by the ocean in the surface layer where it accumulates.

Calm conditions and extreme surface heating strengthen summertime stratification of the MS (Coma et al., 2009; Sparnocchia et al., 2006). On top of this, elevated SSTs impact atmospheric conditions. Higher SSTs induce greater precipitation over central Europe (Messmer et al., 2017) and reinforce the strength of atmospheric heatwaves creating a positive feedback mechanism for warming over and within the Mediterranean basin (Feudale and Shukla, 2007; García-Herrera et al., 2010). The 2003 event is linked with a positive phases of the Atlantic Multi-decadal Oscillation (AMO; Holbrook et al., 2019), a climate oscillation that affects SSTs in the Atlantic by increasing air temperature and reducing wind stress.

#### *2.3.2.2 Low oxygen conditions*

In the last century, the basin has generally been in a fully oxygenated state (typically 180-240  $\mu\text{mol l}^{-1}$ ) and remains well ventilated (Mavropoulou et al., 2020). However, punctuations of low oxygen and hypoxic conditions have been documented (e.g. Kralj et al., 2019). These are predominantly associated with stratification and anthropogenic enrichment driving primary production and organic matter export. Low oxygen events tend to be confined to coastal and semi-enclosed areas (Kountoura and Zacharias, 2014; Kralj et al., 2019; Rabalais et al., 2010). For example, two periods of hypoxia were recorded in the Gulf of Trieste (northern Adriatic) in 2015 and 2016. Both occasions were preceded by heavy precipitation in spring which increased riverine discharge and nutrient input. Subsequent warmer weather resulted in strong stratification which inhibited ventilation (Kralj et al., 2019). Regular instances of hypoxia and anoxia were also recorded in Elefsis Bay, Aegean Sea between 1987-2009. However, sedimentary records denote periods of low oxygen in the underlying depositional environment

throughout the Holocene suggesting that natural variation may be the controlling factor (Pavlidou et al., 2010).

On millennial timescales, the Eastern Mediterranean has seen the formation of deep-sea sapropels (Rohling et al., 2015). Sapropels are layers of sediment that are carbon-rich, signifying an anoxic (zero [O<sub>2</sub>]) depositional environment. They correlate with solar precession cycles which intensify the Indian Ocean monsoon. Precipitation increases enhance discharge from the River Nile adding nutrients to the basin. The elevated export flux of organic matter depletes [O<sub>2</sub>] in the water column and the benthic environment. Oxygen is the most efficient electron receptor for bacterial respiration; once exhausted, organic matter is broken down at a slower rate resulting in a carbon-rich sediment layer. There is no evidence of similar events in the Western Mediterranean, likely because of the inflow and outflow via the Strait of Gibraltar injecting sufficiently dense water driving mixing (Rohling et al., 2015; Rohling and Hilgen, 2007).

### 2.3.3 Future of the Mediterranean Sea

Multi-model analysis suggests that the 2003 MHW event will become the 'new normal' by 2050 and represent a weak occurrence by 2100 under RCP8.5 (Darmaraki et al., 2019b). The same ensemble shows extreme SSTs increasing faster than mean temperatures throughout the 21<sup>st</sup> century in the MS: under RCP8.5 (RCP4.5), mean SST and SST<sub>99P</sub> will rise to 3.1±0.5°C and 3.6±0.7°C (1.6±0.8°C and 1.9±0.9°C), respectively (Darmaraki et al., 2019b). Furthermore, end-of-the-century MHW events (averaged across 2071-2099) under RCP8.5 (RCP4.5) will last for 94±10 (59±10) days, cover 52±5% (45±5%) of the basin, show mean SST<sub>99Q</sub> exceedances of 1.4±0.4°C (0.5±0.2°C), and maximum exceedances of 3.7±0.6°C (1.9±0.4°C; Darmaraki et al., 2019b). Changes in MHWs will increase thermal stratification, subsurface ventilation and surface solubility. Therefore,

it is important to investigate how MS dissolved oxygen will change in this MHW hotspot region.

#### 2.4 Aims and research questions

The three principal drivers of deoxygenation (solubility, respiration and stratification) are primarily driven by temperature, and fluctuations in  $[O_2]$  are shown to have a detrimental impact on ocean ecosystems. CMIP5 models have demonstrated the negative relationship between mean SST and subsurface dissolved oxygen (Bopp et al., 2013) but there remains a need to explore the relationship between their respective extreme states. While MHW characteristics are well defined, insofar, no attempts have been made to apply extreme statistical metrics to  $[O_2]$  in the MS or globally under future climate change. My research employs a percentile-based extremes approach on both SST and  $[O_2]$ . I use a coupled physical-biogeochemical model to investigate the change in incidence of extremes in SST and  $[O_2]$  and how they relate. I focus on the MS because there is ample evidence of extreme events occurring in the region. I aim to characterise and delineate MHWs and low dissolved oxygen events in the MS over the recent past and under future climate change. I will quantify the contributions of ventilation and solubility changes to the low dissolved oxygen events. And finally, I will attempt to determine a temporal relationship between MHWs and low oxygen events, demonstrating that MHW intensity affects the  $[O_2]$  response. These aims lead to the following questions:

1. How will extremes in SST and dissolved oxygen in the MS change by the end of the century in terms of frequency, intensity, and spatial distribution?
2. In response to MHWs, what are the relative contributions from  $O_{2sat}$  and Apparent Oxygen Utilisation (AOU) to the  $[O_2]$  signal?

3. Is there a difference in the response of dissolved oxygen to high and low intensity or high and low category MHWs at the end of the century under RCP4.5?

## 3 Methods

### 3.1 Data

#### 3.1.1 Model data

To study Mediterranean MHWs and their effect on  $[O_2]$ , I used outputs from a coupled physical-biogeochemical model covering the period 1970 to the end of the 21<sup>st</sup> century. The outputs include daily frequency potential temperature,  $[O_2]$  and AOU for 42 vertical sigma levels that have been interpolated onto a z-grid (depth axis) equating to 0.5-5500 m depth. The horizontal resolution is 11 km (or  $0.1^\circ$  longitude-latitude grid). Historical and projected data was produced using the Proudman Oceanographic Laboratory Coastal Ocean Modelling System (POLCOMS; (Holt and James, 2001) coupled to the European Regional Seas Ecosystem Model (ERSEM; Baretta et al., 1995). The model was forced under two CMIP5 Representative Concentration Pathways (RCPs; Taylor et al., 2012) 4.5 and 8.5 with climate forcing divergence occurring at the mid-point of the 21<sup>st</sup> century. POLCOMS-ERSEM has been used to explore climate change impacts of the Northwest European continental shelf seas (Artioli et al., 2012; Holt et al., 2016) and the Mediterranean Sea (Kay and Butenschön, 2018; Maynou et al., 2020).

The POLCOMS-ERSEM dataset is provided by Plymouth Marine Laboratory as a member of the Climate Change and European Aquatic Resources (CERES) project. This consortium consists of universities, research institutes and industry partners, and was created to aid long-term management plans for European seas to ensure food security. Aims of the project include providing high resolution projections of significant environmental variables relevant to the European fishing and aquaculture industries as well as assessing climate change risks to marine ecosystems (Peck et al., 2020). The data comprises of three

Global Coastal Ocean Modelling System (GCOMS) domains (see *figure 1*; Holt et al., 2009) including Canary Current, North Sea and Mediterranean Sea; for my analysis I focus on the latter.

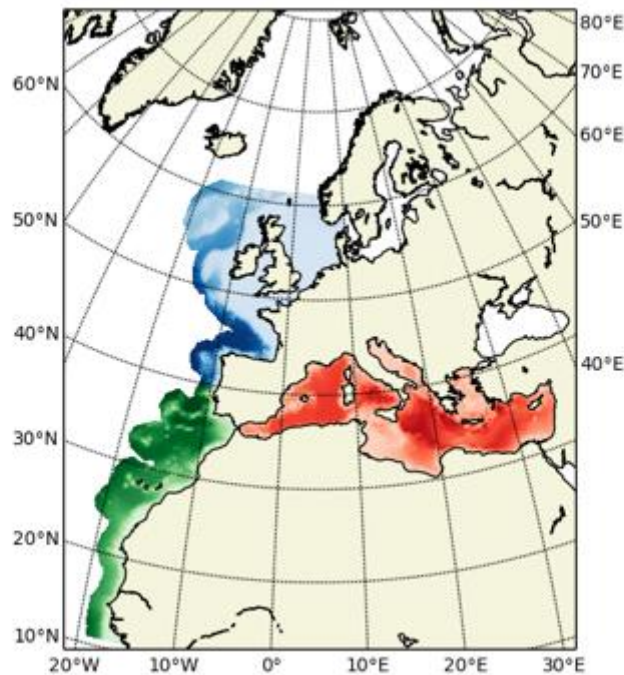


*Figure 6: three subdomains included in the POLCOMS-ERSEM model for the CERES project: the North Sea and Northeast Atlantic (blue), the Canary Current (green) and the Mediterranean Sea (red).*

### 3.1.2 POLCOMS

POLCOMS is a physical ocean model designed for shelf seas and utilises a three-dimensional baroclinic Arakawa B-grid. It provides finer scale resolution of coastal regions affording better quantification of these biogeochemically important areas. These regions yield 30% of primary production despite accounting for only 8% of the bathymetric area (Longhurst et al., 1995), yet they are poorly resolved by coarser scale Earth system models. For example, OGCMs struggle to capture baroclinic Rossby waves and often neglect to represent long gravity waves. Both processes are a dominant

influence on shelf seas (Holt et al., 2009) which POLCOMS resolves more accurately than most GCMs.

### 3.1.3 ERSEM

The ERSEM component models the marine biogeochemistry, benthic fauna and pelagic plankton with its functions based on ecosystem roles (Butenschön et al., 2016). It simplifies diverse and complex ecology into distinct groups that each have a different impact on biogeochemistry. It consists of four phytoplanktonic groups (primary producers), three zooplanktonic groups (consumers) and a bacterial group (decomposers; see *figure 7*). It also has nutrient pool inputs of carbon, nitrogen, phosphorus and silicate. The biological groups function in distinct ways, for example, each will have different rates of nutrient assimilation, excretion, predation, respiration and non-predatory mortality. Validation with in-situ data demonstrates the model's capability to capture a variety of oceanic ecosystems from oligotrophic seas such as the MS to eutrophic coastal regions (Butenschön et al., 2016). Annual mean chlorophyll-*a* data from POLCOMS-ERSEM has been demonstrated to reproduce observed data from NASA's MODIS-Aqua sensor in the Northeast Atlantic with mean error values between 0.2-0.6 mg m<sup>-3</sup> during summer and autumn in 2006 (Shutler et al., 2011). Similarly, model simulated macronutrient fields in the North Sea is consistent with measurements from ship-based CTD and water-sampling stations (Allen et al., 2007).



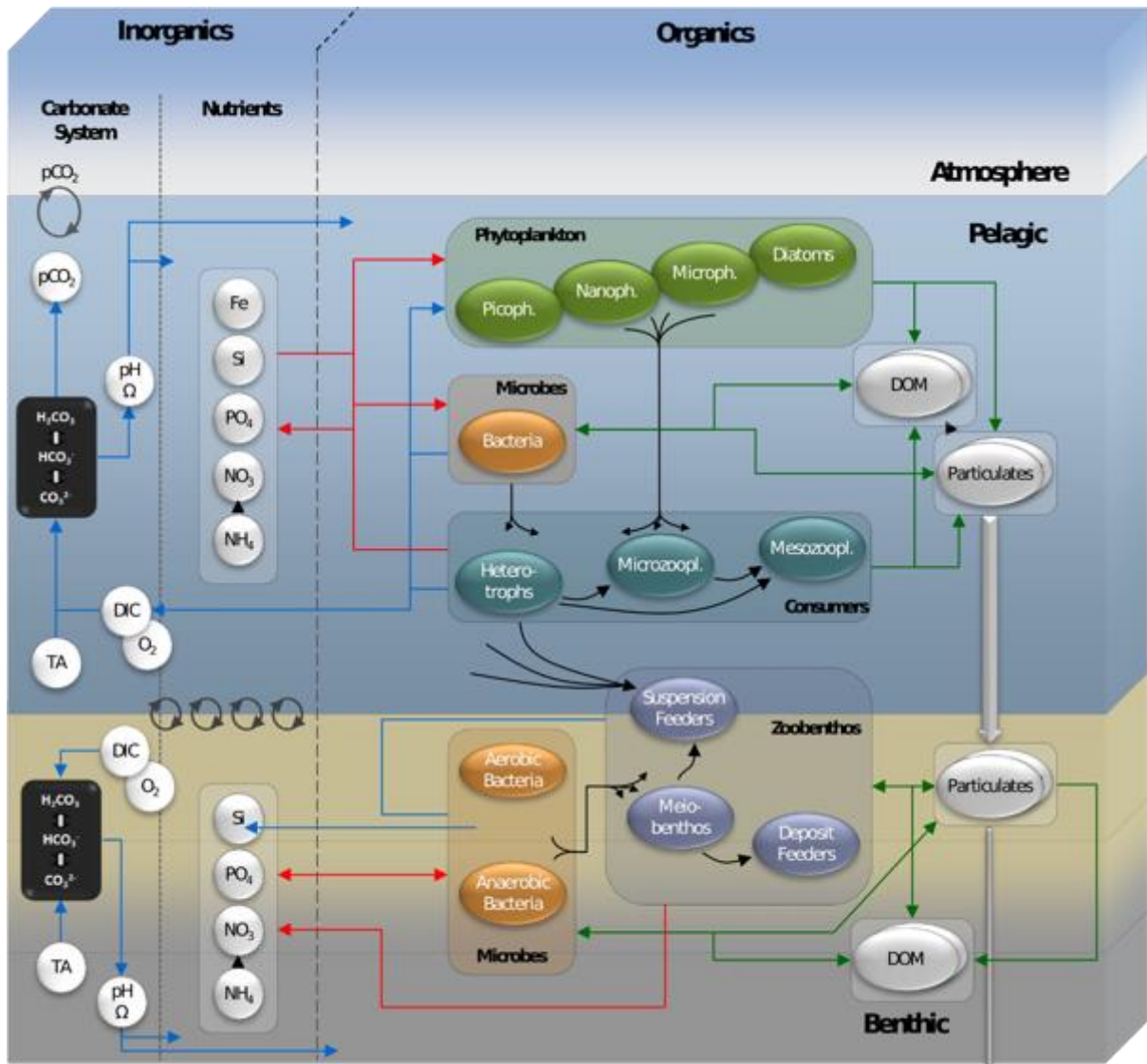


Figure 7: ERSEM model schematic showing the ways in which model elements interact with each other. Inorganic carbon fluxes are represented in blue, nutrient fluxes in red, predator-prey interactions in black and non-living organic fluxes in green. Reproduced from Butenschön et al. (2016). The focus of this study predominantly concerns the pelagic part of the model system.

### 3.1.4 Climate and ocean forcing

The POLCOMS-ERSEM experiments were forced with atmospheric output from a Coupled Model Intercomparison Project Phase 5 (CMIP5) model for the historical period and under RCP4.5 and RCP8.5. RCPs relate to the global mean increase in radiative forcing per square meter on the globe by the end of the 21<sup>st</sup> century (e.g. RCP4.5 equates to an increase of in radiative forcing of 4.5 W m<sup>2</sup>). RCP 4.5 is a moderate scenario where

greenhouse gas (GHG) levels stabilise at the mid-point of the century, while RCP8.5 is a high end scenario where atmospheric GHGs continue to increase throughout the century (Taylor et al., 2012). For the CERES project, the Max Plank Institute for Meteorology Earth System Model (MPI-ESM-LR) was selected to provide atmospheric boundary conditions because it gave the best representation of the CMIP5 ensemble despite generating lower mean surface air temperatures. Other GCMs deemed less suitable included Hadley Centre Global Environment Model version 2 (HadGEM2-ES) which had a tendency towards extreme values relative to the ensemble. A hindcast version of the model is available forced with reanalysis from 1970-2005, however, for continuity between the past and future, I use the CMIP5 forced historical experiment and subsequent projections only.

Atmospheric forcing has been downscaled to  $0.11^\circ$  across a combination of European GCOMS domains by Rossby Centre regional Atmospheric model (RCA4) as a part of the Coordinated Regional Downscaling Experiment (CORDEX) initiative (Giorgi et al., 2009). RCA4 allows for finer scale resolution in atmospheric forcing providing greater variance which will increase the model's capability of resolving small scale processes. At the open ocean boundary, POLCOMS-ERSEM utilises a one-way nesting system where boundary data from MPI-ESM-LR can affect data within the study region but not vice versa. The advantages of one-way nesting include computational efficiency and an enhanced likelihood of detection and attribution of anthropogenic signals in biogeochemical fluxes within the system across historical and RCP runs as the ocean and atmospheric forcing is consistent (Holt et al., 2009). However, interactive feedback processes between the open ocean and shelf seas cannot be inferred as MPI-ESM-LR data will not be affected by physical and biogeochemical changes within the domain.

The initial physical and biogeochemical conditions of the model were based on World Ocean Atlas (WOA) data. WOA phosphate values have been demonstrated to exceed observed levels in the MS. As a result of this, nitrate is the limiting nutrient in ERSEM for the MS (Kay et al., 2018). Despite this, rates of primary productivity are consistent with observations between 1998-2015 in the majority of the basin with only slight overestimations of mean surface chlorophyll ( $<0.8 \text{ mg m}^{-3}$ ) in the winter and spring bloom. E-HYPE is a hydrological model used by the CERES project to estimate riverine inputs into the ocean in the model run. A coding error has led to inaccurate biogeochemical inputs (pH, nutrients and dissolved inorganic carbon) limiting the reliability of regions surrounding river mouths in the context of this research, with Rhône riverine input particularly affected (Kay et al., 2018).

### 3.1.5 Methods used for model-data comparison and results calculations

In order to validate POLCOMS-ERSEM SST, I bilinearly interpolated model data from the  $0.1^\circ$  grid onto the  $0.05^\circ$  grid of SST Climate Change Initiative Advanced Very High-Resolution Radiometer and Along Track Scanning Radiometer (SST CCI AVHRR ARSR) product data for the MS from Merchant et al. (2019) for comparison. This process was carried out using a Climate Data Operator (CDO) function that remaps across the  $x$  and  $y$  planes. To validate 3D temperature and  $[\text{O}_2]$  model data I use Pyferret's trilinear interpolation on the upper 23 sigma levels (representing 0.5–250 metres). I interpolate from the  $0.1^\circ$  grid onto the  $1/8^\circ$  longitude-latitude grid with 11 depth-levels (0-225 m) from Mavropoulou et al. (2020).

All thresholding, climatology, mean and maximum calculations are performed using CDO functions while spatial averaging is conducted within Pyferret for all figures and results in *Table 2, 3 and 4*. Histograms (*Figures 8 and 15*) are a count of spatially-averaged daily

data that is then calculated into a fraction within Pyferret. Hovmoller plots (*Figures 10, 11, 20, 21 and 22*) depict climatological data that are calculated using CDO functions and then spatially averaged within Pyferret; however, data for *Figures 21 and 22* are masked based on MHW intensity and category using CDO functions. For results on the changes to mean and extreme temperature and [O<sub>2</sub>] from 1982-2099 (*Figure 14*), yearly values are calculated and then averaged spatially for the MS and each individual subbasin.

## 3.2 Model-data comparison

### 3.2.1 Sea Surface Temperature

#### 3.2.1.1 Historical SST distribution

I use SST CCI AVHRR ARSR (Merchant et al., 2019) to determine an appropriate MHW threshold (1982-2011), develop a fixed percentile MHW categorisation scheme (1982-2011), and validate SST in the POLCOMS-ERSEM historical simulation (1982-2005). Observed SST comprises daily thermal infra-red radiance measurements from satellites set to a 0.05° latitude-longitude grid and data assimilation is used to fill grid cells with no measurements (Merchant et al., 2019). Satellites measure the surface 'skin' layer of the ocean via radiance that is converted to temperature. The difference between depth SST and the skin layer typically ranges between 0.1-0.5 K, but can be as high as ~5 K under conditions of low wind and strong solar radiation (Gentemann et al., 2008). To account for this disparity, satellite measurements contained within the dataset have been validated against a depth range of in-situ SST measurements with the output intended to represent 0.2 m depth (Merchant et al., 2019). Modelled surface-level temperature data has been bilinearly interpolated onto the 0.05° grid for comparison.

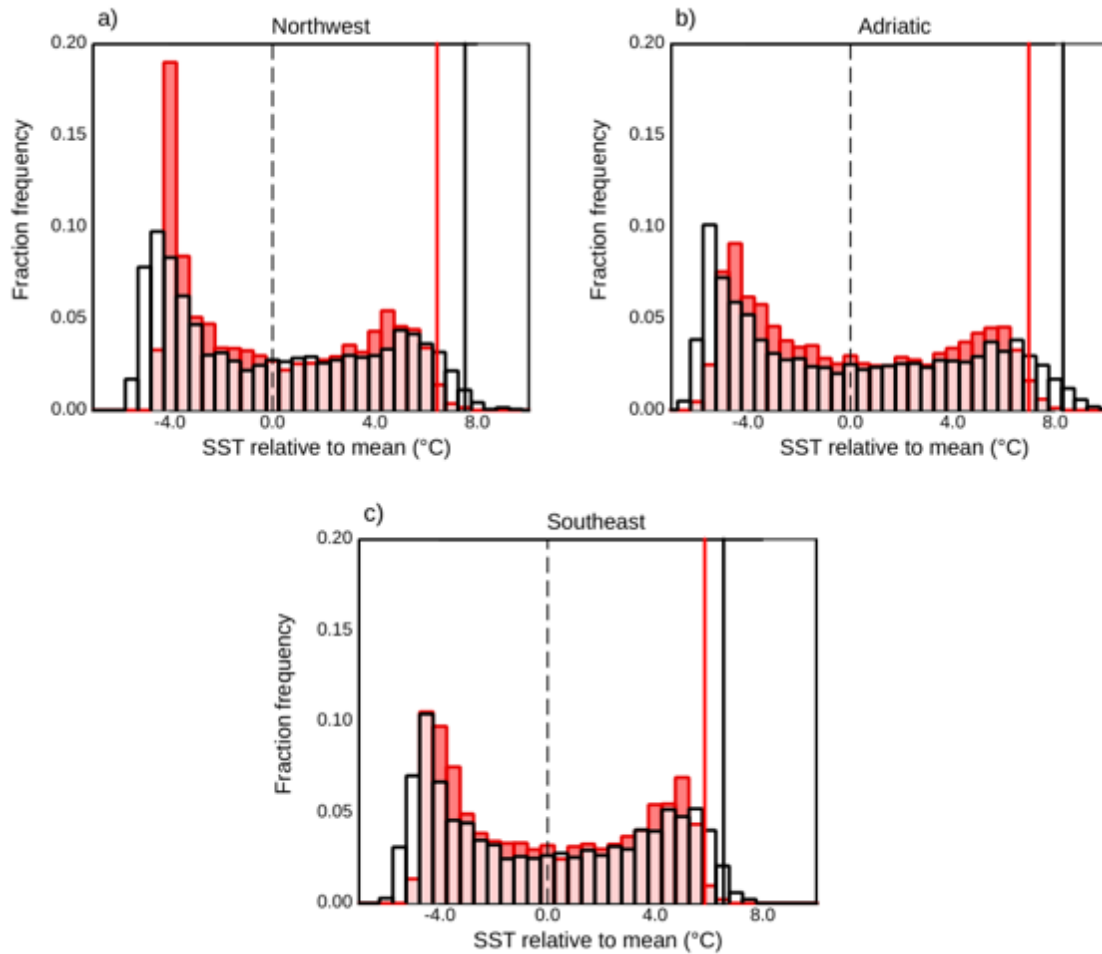


Figure 8: SST anomalies as fractional frequency throughout the period of 1982-2005 comparing model (red) and observations (clear/black outline) relative to their respective means (vertical dashed line) in each basin (NW (a), AD (b) and SE (c)). Vertical lines denote 99<sup>th</sup> percentiles in observed (black) and model (red).

Figures 8a, b and c demonstrate that the historical experiment of POLCOMS-ERSEM is able to generally reproduce the spread of satellite SST data. However, very high and very low SSTs are not as accurately reproduced. Modelled SST range is lower than the observed range in each basin by 3.24°C, 2.8°C and 1.80°C in NW, AD and SE, respectively. In turn, 99<sup>th</sup> percentiles are consistently lower by 1.09°C, 1.34°C and 0.70°C. Essentially, the model's ability to produce extreme positive deviations in SST is more muted when compared with satellite observations. Despite this, fractional frequency of the highest SSTs in observations are matched in shape by the model suggesting there is corroboration in MHW frequency, but that the model may be conservative in terms of

event intensity. The larger disparity in the SST range of NW stems from the model's apparent inability to reproduce wintertime SSTs below  $-4^{\circ}\text{C}$  relative to the mean. This is a known issue with the POLCOMS-ERSEM (Kay et al., 2018) but as my focus is extreme positive threshold exceedances this work is unaffected.

### 3.2.1.2 MHW threshold selection

Daily observational SST data (1982-2011) is compared using the two most prominent methods of MHW detection: the fixed 99<sup>th</sup> percentile ( $\text{SST}_{99\text{Q}}$ ) and the climatological 90<sup>th</sup> percentile ( $\text{SST}_{90\text{P}}$ ; see section 2.2.1) (Frölicher et al., 2018; Hobday et al., 2016). Both methods were applied during the 2003 Northwest Mediterranean MHW event. *Figure 9* displays idealised schematics of  $\text{SST}_{90\text{P}}$  (*Figure 9a and c*) and  $\text{SST}_{99\text{Q}}$  (*Figure 9b and d*) in the top row and categorisation for each method in the middle row using 2003 data with thresholds displayed in black dashed lines. In *Figure 9e*, thresholds have been normalised to zero allowing determination of the most appropriate method to distinguish biological impacts associated with the 2003 Northwest Mediterranean MHW.  $\text{SST}_{90\text{P}}$  determines the 2003 event to be longer and more intense compared with  $\text{SST}_{99\text{Q}}$  (*Figure 9e*). Event intensity also varies between the methods peaking on the 14<sup>th</sup> of June for  $\text{SST}_{90\text{P}}$  (Hobday et al., 2018) and the 12<sup>th</sup> of August for  $\text{SST}_{99\text{Q}}$ . The most devastating biological impacts of the 2003 MHW were observed in August and September (Garrabou et al., 2009) and appear unrelated to  $\text{SST}_{90\text{P}}$  peak intensity. Additionally, each method was applied to daily maximum SST data during the more localised 1999 MHW in the Northwest MS. Once again, peak event intensity of  $\text{SST}_{99\text{Q}}$  more closely matched with biological impacts than  $\text{SST}_{90\text{P}}$  (*figure not shown*).

Important MHWs in the MS occur only in summer (Darmaraki et al., 2019a).  $\text{SST}_{99\text{Q}}$  naturally focuses on summertime events as opposed to  $\text{SST}_{90\text{P}}$  which classifies events all

year round. In May 2003 for example, maximum SST exceeded the SST<sub>90P</sub> threshold but remained lower than 25°C. MS sessile species' thermotolerance is only pertinent in temperatures elevated at 25°C or above (Cau et al., 2018; Kersting et al., 2015) with biological assemblages being less susceptible to winter- and springtime warming (Galli et al., 2017; Morley et al., 2017). Therefore, SST<sub>90P</sub> is less suitable for the Northwest basin of the MS. Overall, I apply the SST<sub>99Q</sub> method to analyse MHWs in modelled data because it is the most appropriate for delineating MHWs in the MS.

A limitation of SST<sub>99Q</sub> compared with SST<sub>90P</sub> is that no intensity categorisation scheme has been developed (see section 2.1.1). In order to quantify MHW categories using SST<sub>99Q</sub>, the selection of a relative climatological baseline is required to perform the role of the climatological mean in SST<sub>90P</sub> (Hobday et al., 2018). The primary aim of the SST<sub>99Q</sub> baseline is to closely match the SST<sub>90P</sub> categories of the 2003 and 1999 MHW events. August climatological mean is therefore selected for the SST<sub>99Q</sub> categorisation scheme (*figure 9b*) because it most closely matches the SST<sub>90P</sub> categorisation of the 1999 and 2003 MHW events. SST<sub>99Q</sub> is more sensitive (category 4) compared with SST<sub>90P</sub> (category 3) when applied to 2003 maximum SST data in NW which in the context of the MS alone can be considered as a more appropriate classification.

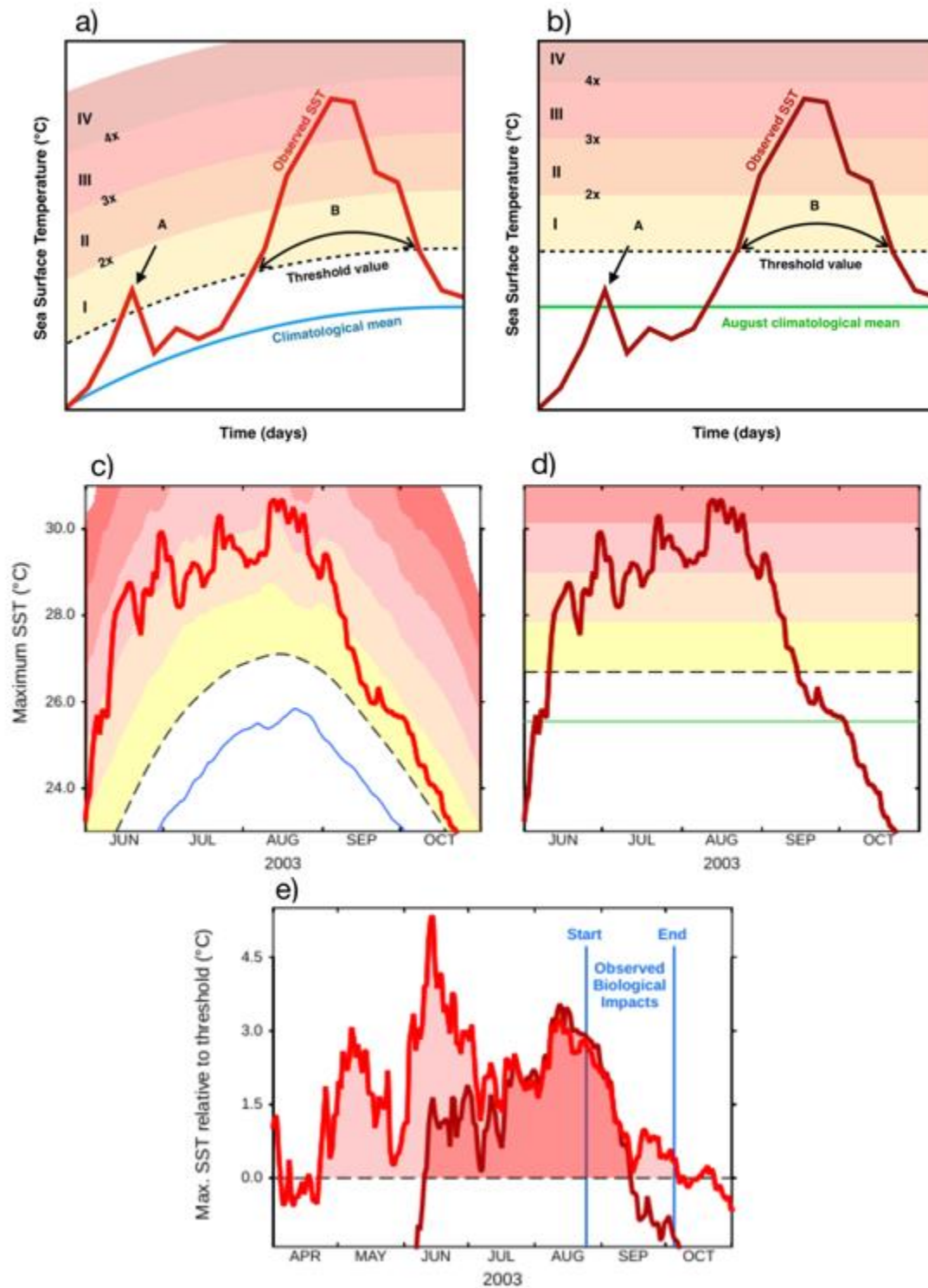


Figure 9: Comparing two MHW categorisation schemes.  $SST_{90P}$  displayed in a and c alongside the newly proposed categorisation scheme for  $SST_{99P}$  in panels b and d. Panels a and b show idealised schematics ; c and d show the schemes applied to satellite maximum SST in the North-West Mediterranean basin during the 2003 MHW event. Label A denotes a heat-spike that exceeds  $SST_{90P}$  in a but not  $SST_{99P}$  in b; label B denotes a MHW which varies in duration and intensity depending on the method of detection. Panel e compares the two schemes by normalising both to zero (SST minus threshold) so that the dashed black line represents  $SST_{90P}$  (light red line) and  $SST_{99Q}$  (dark red line). The blue vertical lines represent the beginning and end of observed biological impacts.



### 3.2.2 Seasonal water column validation

#### 3.2.2.1 Historical temperature and dissolved oxygen

I carry out a model validation by comparing historical (1982-2005) POLCOMS-ERSEM temperature and dissolved oxygen data with a monthly climatology (1960-2011) of observed potential temperature and [O<sub>2</sub>] data (Mavropoulou et al., 2020). Mavropoulou et al. (2020) made available annual mean temperature and [O<sub>2</sub>] with depth from 1960-2011 and a monthly climatology with depth spanning the same time period. Validating seasonality is important given that ecosystem relevant MHWs in the MS are associated with amplified seasonal warming. Therefore, the climatology is deemed the most appropriate despite the issue of differing timespans.

The observational climatology was produced using World Ocean Database 2013 (WOD13) data (Boyer et al., 2013) that has been regrided using Data-Interpolating Variational Analysis (DIVA; Troupin et al., 2012) by Mavropoulou et al. (2020). WOD13 observations consist of ocean station data, moored and drifting buoys, and high- and low-resolution conductivity-temperature-depth profiles. As satellites cannot measure below the sea surface and other methods are less cost-effective, there is a lack of good spatiotemporal data coverage within the MS. DIVA interpolates sparse and non-uniform data via a variational inverse method. Cost function minimisation and an appropriate correlation length relative to the constructed grid allows the best fit of the available data. The data is presented on a 1/8° longitude-latitude grid at 11 depth-levels (0-225 m). I use a depth range 0.5 to 200 metres to study the impacts on MHWs on water column [O<sub>2</sub>]. Modelled temperature and [O<sub>2</sub>] are bilinearly interpolated to match observations in *Figures 10 and 11*.

Generally, POLCOMS-ERSEM is able to reproduce the seasonal cycle of temperature for each basin well in the upper 200 metres of the water column with values within 1°C of the basin mean (*Figure 10*). The variability of the surface layer (0-50 metres) is more difficult to model which is reflected by annual mean RMSE values of 0.54, 0.51 and 0.61. The model is weakest in capturing the penetration of elevated temperatures in the surface (0-50 m) during late-summer and autumn. Here, RMSE is highest at 1.41, 0.98 and 1.16 in the 3 basins. This feature is overestimated in NW and AD but underestimated in SE and which may impact interior [O<sub>2</sub>] by affecting ventilation through stratification along with respiration rates. Significantly, RMSE is much lower in the spatiotemporal regions where deoxygenation signals develop. For example, beneath the highly variable surface layer between 80-200 metres, annual mean RMSE is 0.13, 0.19 and 0.23 in NW, AD and SE, respectively, and does not exceed 0.36, 0.69 and 0.59.

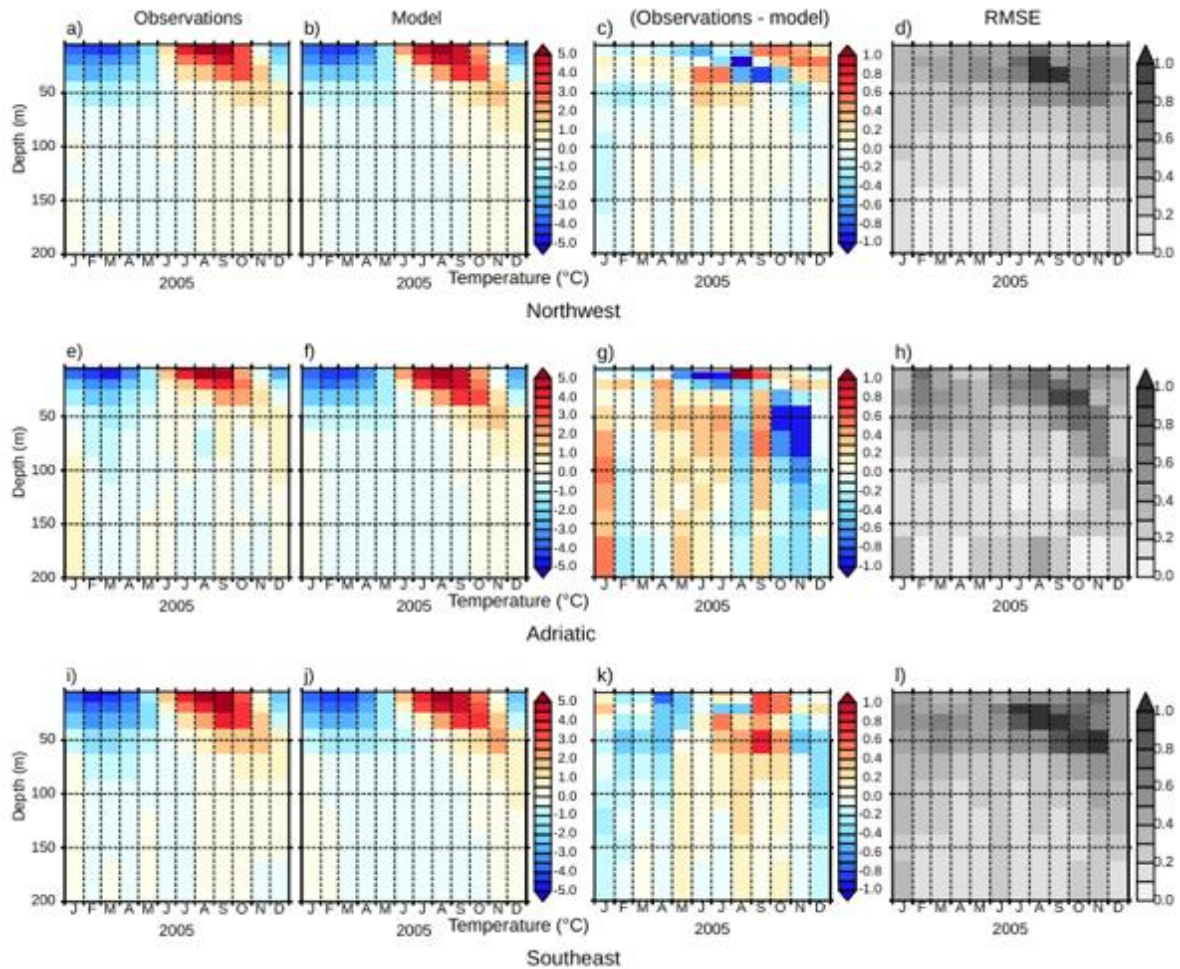


Figure 10: Observed (a, e and i) and model (b, f and j) water column temperature ( $^{\circ}\text{C}$ ) in NW (a-d), AD (e-h) and SE (i-l) along with observational-model differences (c, g and k) and root mean square error (RMSE; d, h and l). All data is relative to the respective mean state.

Modelling dissolved oxygen is complex due to interactions between physical and biological processes in the ocean; it is therefore less well constrained within models compared with temperature. Nevertheless, the observed seasonal cycle is once again well represented, capturing mixed layer deepening during winter and spring with summertime stratification beginning in June and persisting into winter (Figure 11). Table 1 summarises model-data RMSE values specified for the year-round well-mixed surface layer (0-50 metres depth) and subsurface (80-200 metres). The model shows the greatest skill in SE likely due to increasing oligotrophy eastwards within the MS. In oligotrophic

regions [O<sub>2</sub>] is more likely to be controlled by physical processes (e.g. temperature driven solubility changes) which are generally well reproduced by the model.

Table 1: mean and spatial maximum root mean square error (RMSE) values for POLCOMS-ERSEM [O<sub>2</sub>] against observations for each basin of the MS at the surface (0-50 metres) and within the interior (80-200 metres).

[O <sub>2</sub> ] RMSE		NW	AD	SE
		<i>Surface (0-50 metres)</i>		
January - June	Mean	5.37	6.65	4.23
	Max.	8.22	12.5	5.84
July - December	Mean	4.97	8.42	4.37
	Max.	8.66	16.8	6.61
		<i>Interior (80-200 metres)</i>		
January - June	Mean	5.17	2.93	3.51
	Max.	7.13	5.43	4.76
July - December	Mean	4.2	3.15	3.13
	Max.	6.46	5.65	5.06

The model appears to underestimate interior [O<sub>2</sub>] in NW and SE with values ~6-12  $\mu\text{mol l}^{-1}$  lower than observations throughout autumn. However, interior mean (maximum) RMSE values are relatively low from July through December at 4.2 (6.46), 3.15 (5.65) and 3.13 (5.06), respectively in NW, AD and SE. The observed seasonal cycle is less pronounced in AD which is overestimated by the model, contributing to greater bias in this region relative to NW and SE. Possible reasons for this disparity include: oscillations of thermohaline circulation in the upper regions of the Ionian gyre affecting cyclonic circulation in AD (Gačić et al., 2011); the model may be unable to accurately reproduce periodic occurrences of the EMT in AD (see section 2.3.1); the known issue of unreliable riverine nutrient influx within the model is most concentrated in AD, with the most significant input from the River Po. To avoid the influence of incorrect riverine inputs on biogeochemistry, analysis of modelled SST and [O<sub>2</sub>] will be limited to regions that are  $\geq 100$  metres depth. This leaves 55% of the area of AD to be analysed.

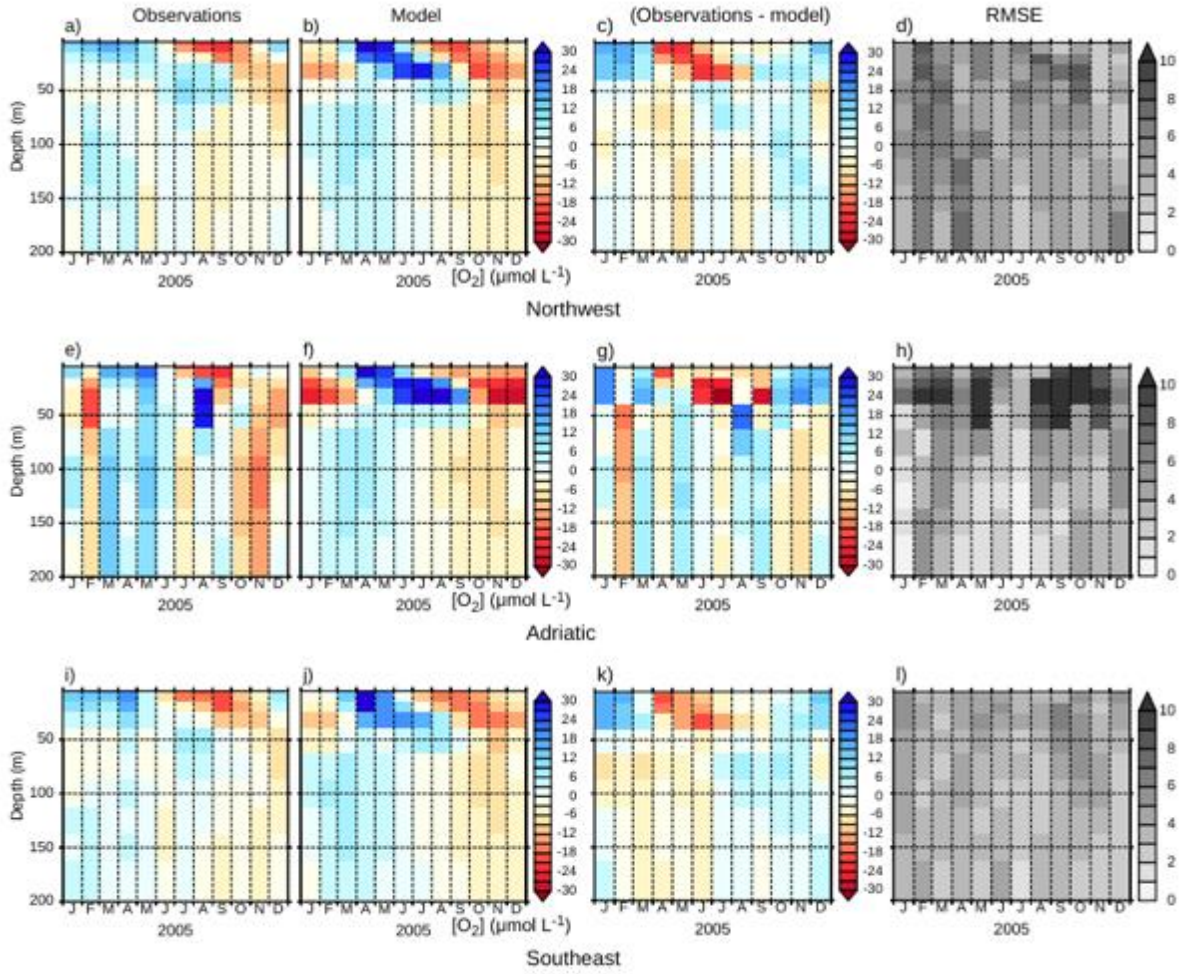


Figure 11: Observed (a, e and i) and model (b, f and j) water column  $[O_2]$  ( $\mu\text{mol l}^{-1}$ ) in NW (a-d), AD (e-h) and SE (i-l) along with observational-model differences (c, g and k) and root mean square error (RSME; d, h and l). All data is relative to the respective mean state.

### 3.2.2.2 Dissolved oxygen extreme threshold selection

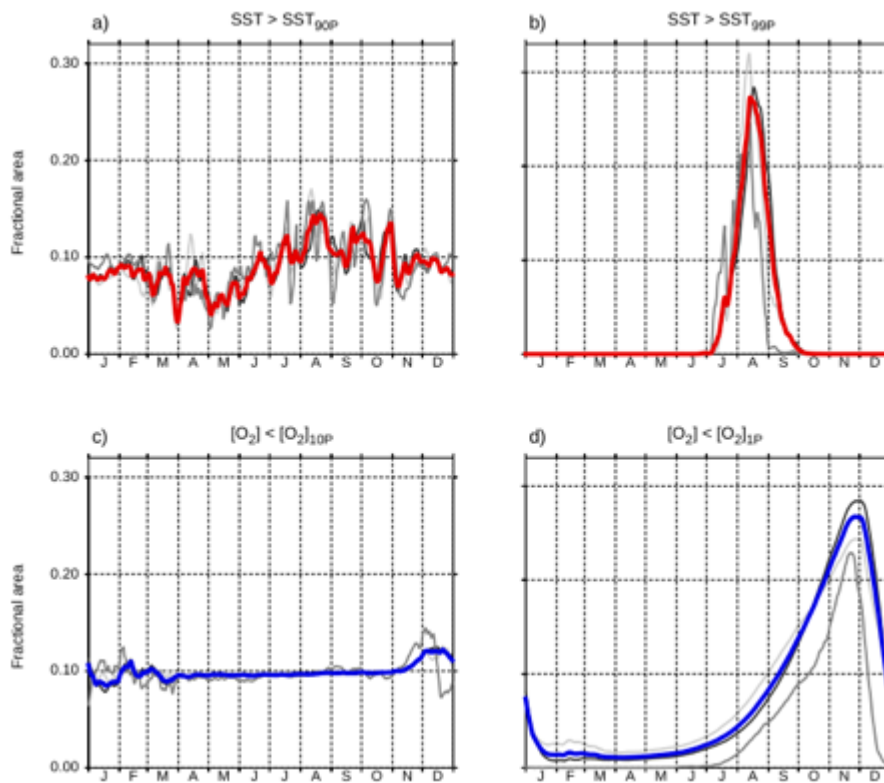


Figure 12: Climatological fractional area of the Mediterranean Sea and sub-basins in an extreme state over the baseline period (1982-2005) in SST (a and c) and dissolved oxygen at 100 m depth (b and d) for  $SST_{90P}$  (a) and  $[O_2]_{10P}$  (b), and  $SST_{99P}$  (c) and  $[O_2]_{1P}$  (d) using POLCOMS-ERSEM data. (Entire Mediterranean basin – thick red and blue lines; NW – light grey; Adriatic – mid-grey; SE – dark grey).

The two thresholds discussed in section 3.2.1 ( $SST_{99P}$  and  $SST_{90P}$ ) are applied contemporaneously to low  $[O_2]$  at 100 metres depth (herein  $[O_2]_{(100)}$ ). This gives corresponding and opposing 1<sup>st</sup> and climatological 10<sup>th</sup> percentile thresholds  $[O_2]_{(100)1P}$  and  $[O_2]_{(100)10P}$ . ‘Extreme’ defines values exceeding these thresholds as for MHWs. Within POLCOMS-ERSEM,  $[O_2]$  at 100 metres depth (herein  $[O_2]_{(100)}$ ) is where low oxygen events are simulated to occur most frequently across the MS (*figure not shown*).

Figure 12 shows the temporal mean of fractional area coverage of extremes in SST and  $[O_2]_{(100)}$  between 1982-2005 in POLCOMS-ERSEM data for the entire MS and subbasins. It highlights further the utility of  $SST_{99P}$  to represent biologically relevant summer MHWs

and demonstrates the capability of  $[O_2]_{(100)1P}$  to identify the lowest subsurface  $[O_2]$  (figure 12d). Low  $[O_2]$  extremes follow MHWs in the seasonal cycle which matches the current understanding of MS dynamics. Whereas  $[O_2]_{(100)10P}$  does not pick out  $[O_2]$  depletion events as clearly and is consistent at  $\sim 0.1$  area coverage for most of the seasonal cycle.

As of yet, there exists no relative classification of  $[O_2]$  extremes. My work is the first to determine and categorise oxygen events (figure 13). In order to better compare well-researched MHWs and newly classified oxygen events, the events will be categorised in a similar manner following the categorisation scheme devised in section 3.2.1.2 (Figure 9). As the Mediterranean experiences extreme low  $[O_2]$  values during the autumn, a climatological mean calculated from October, November and December data will be used as a baseline relative to the threshold with which events will be categorised (in the same fashion as august climatological mean for SST<sub>99P</sub>).

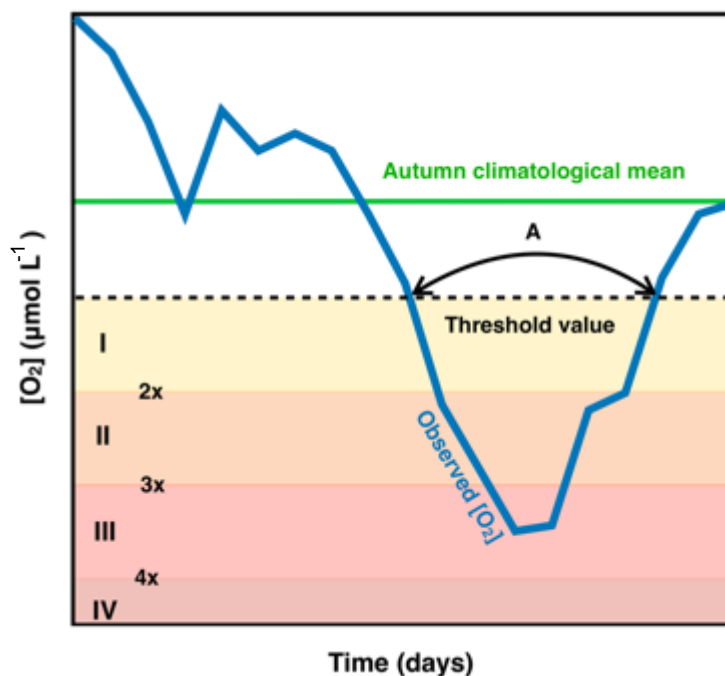


Figure 13: Definition and determination of a major oxygen low (MOL). The blue line shows the observed  $[O_2]$  at depth for a particular location. The dashed black line represents the fixed 1<sup>st</sup> percentile threshold. Autumn climatological mean is

represented in green and is used to categorise events: category I is one- to two-times the difference; category II is two- to three-times; category III in three- to four-times; category IV is four-times or above. Label A represents a category III MOL.

### 3.3 Apparent oxygen utilisation

AOU is a measure of both ventilation and biological activity and is described as:

$$AOU = O_{2sat} - [O_2] \quad (4)$$

where  $[O_2]$  is observed and  $O_{2sat}$  is the expected value of  $[O_2]$  if a body of water at given temperature and salinity is in equilibrium with the atmosphere. AOU measures the age of a water parcel since ventilation given the rate of bacterial oxidation of organic matter known as oxygen utilisation rate ( $OUR = \frac{dAOU}{dt}$ ). Without known respiration rates, it can be associated with an increase in ocean stratification (inhibited ventilation) or an increase in the export flux of organic matter. I will use POLCOMS-ERSEM reported AOU and derived  $O_{2sat}$  to look at deoxygenation related to solubility versus ventilation and stratification.

$$[O_2]_{sat} = [O_2] + AOU \quad (5)$$



## 4 Results and discussion

I look first at end-of-the-century changes to MHW and MOL events relative to historical data within POLCOMS-ERSEM. I present changes to means and extremes of SST and  $[O_2]_{(100)}$ . These results elucidate future exacerbation and sequencing of simulated MHW and MOL events and demonstrate that the intensity of MHWs relates to the intensity of MOLs. *Table 2* shows a summary of applied metrics for the entire Mediterranean basin and each of its 3 subbasins, quantifying changes in mean SST and  $[O_2]_{(100)}$  along with MHW and MOL event characteristics from the past to the end of the century. Temperature and dissolved oxygen data in *Table 2* represent the average year for each parameter, aside from maximum values which represent the maximum across the specified 24-year period.

Table 2: A summary of spatial averaged POLCOMS-ERSEM analysis. Mean and extreme threshold trends in SST and  $[O_2]^{100}$  are based on annual means and given in  $^{\circ}C\ year^{-1}$  and  $\mu mol\ l^{-1}\ year^{-1}$  across 1982-2099, while MHW and MOL event characteristics are an average of all events in the two 24-year periods (1982-2005; 2076-2099). Mean and maximum event frequency is a count (days/year) while mean event duration relates to consecutive extreme occurrences. Start and End refer to months that the average event will occur within, and fractional coverage is the fraction of the MS that will experience extremes in an average year.

	Historical (1982-2005)				RCP4.5				RCP8.5			
	Whole	NW	AD	SE	Whole	NW	AD	SE	Whole	NW	AD	SE
<b>SST evaluation</b>												
					(2006-99)							
Mean SST trend	0.023	0.023	0.020	0.024	0.015	0.015	0.015	0.015	0.032	0.030	0.033	0.033
$R^2$	0.89	0.81	0.64	0.92	0.91	0.96	0.93	0.84	0.98	0.98	0.97	0.98
SST <sub>99Q</sub> trend	0.018	0.011	0.029	0.021	0.020	0.022	0.023	0.018	0.038	0.041	0.044	0.036
$R^2$	0.56	0.17	0.73	0.73	0.90	0.94	0.88	0.85	0.99	0.99	0.97	0.99
<b><math>[O_2]^{100}</math> evaluation</b>												
Mean $[O_2]$ trend	-0.07	-0.06	-0.04	-0.07	-0.13	-0.15	-0.11	-0.11	-0.21	-0.26	-0.17	-0.18
$R^2$	0.63	0.50	0.11	0.52	0.94	0.93	0.96	0.91	0.97	0.96	0.94	0.96
$[O_2]_{10}$ trend	-0.05	-0.07	0.00	-0.04	-0.15	-0.18	-0.14	-0.14	-0.26	-0.33	-0.19	-0.22
$R^2$	0.24	0.46	0.00	0.08	0.92	0.86	0.93	0.92	0.98	0.98	0.95	0.97
<b>MHW characteristics</b>												
					(2076-99)							
Mean frequency (days/year)	4	4	4	4	57.3	57.3	54.4	57.5	99.6	90.5	88.9	106
Max. frequency (days/year)	29	24	25	31	92.2	90.8	89	93.2	129	117	117	137
Start	0	Jul	Jul	Jul	Jun	Jun	Jun	Jun	May	Jun	Jun	May
End	Sept	Sept	Sept	Sept	Oct	Oct	Oct	Oct	Nov	Oct	Oct	Nov
Mean SST>SST <sub>99Q</sub>	0.58	0.67	0.59	0.52	1.79	2.1	2.16	1.59	3.46	3.74	4.02	3.26
Max. SST>SST <sub>99Q</sub>	1.46	1.67	1.55	1.33	3.4	4.28	4.17	2.86	4.84	5.28	5.7	4.52
Mean category	1	1	1	1	4	4	3	4	7	6	6	7
Mean event duration (days)	15	14	9	16	52	52	48	53	94	84	83	100
Fractional coverage	0.28	0.32	0.25	0.29	0.89	0.93	0.93	0.88	0.99	0.99	1.00	0.99
<b>MOL characteristics</b>												
Mean frequency (days/year)	4	4	4	4	173	205	170	154	269	287	250	260
Max. frequency (days/year)	51	54	38	50	275	304	262	259	338	352	293	332
Start	Jun	All year	Jul	Jun	All year	All year	All year	All year	All year	All year	All year	All year
End	Jan	-	Dec	Jan	-	-	-	-	-	-	-	-
Mean $[O_2]<[O_2]_{10}$	-4.19	-4.59	-3.13	-4.01	-12.8	-15.7	-11.4	-11.1	-22.9	-28.9	-18.7	-19.6
Max. $[O_2]<[O_2]_{10}$	-10.8	-12.5	-8.23	-9.99	-24.7	-28.5	-22.3	-22.6	-35.7	-43.2	-29.3	-31.6
Mean category	1	1	1	1	3	4	3	3	6	7	5	6
Mean event duration (days)	49	50	22	50	148	172	131	135	268	297	252	253
Fractional coverage	0.27	0.25	0.23	0.29	0.87	0.89	0.84	0.86	0.98	0.99	0.97	0.98

## 4.1 Changes to mean and extreme states

### 4.1.1 Spatially averaged changes

#### 4.1.1.1 Annual changes from 1982–2009

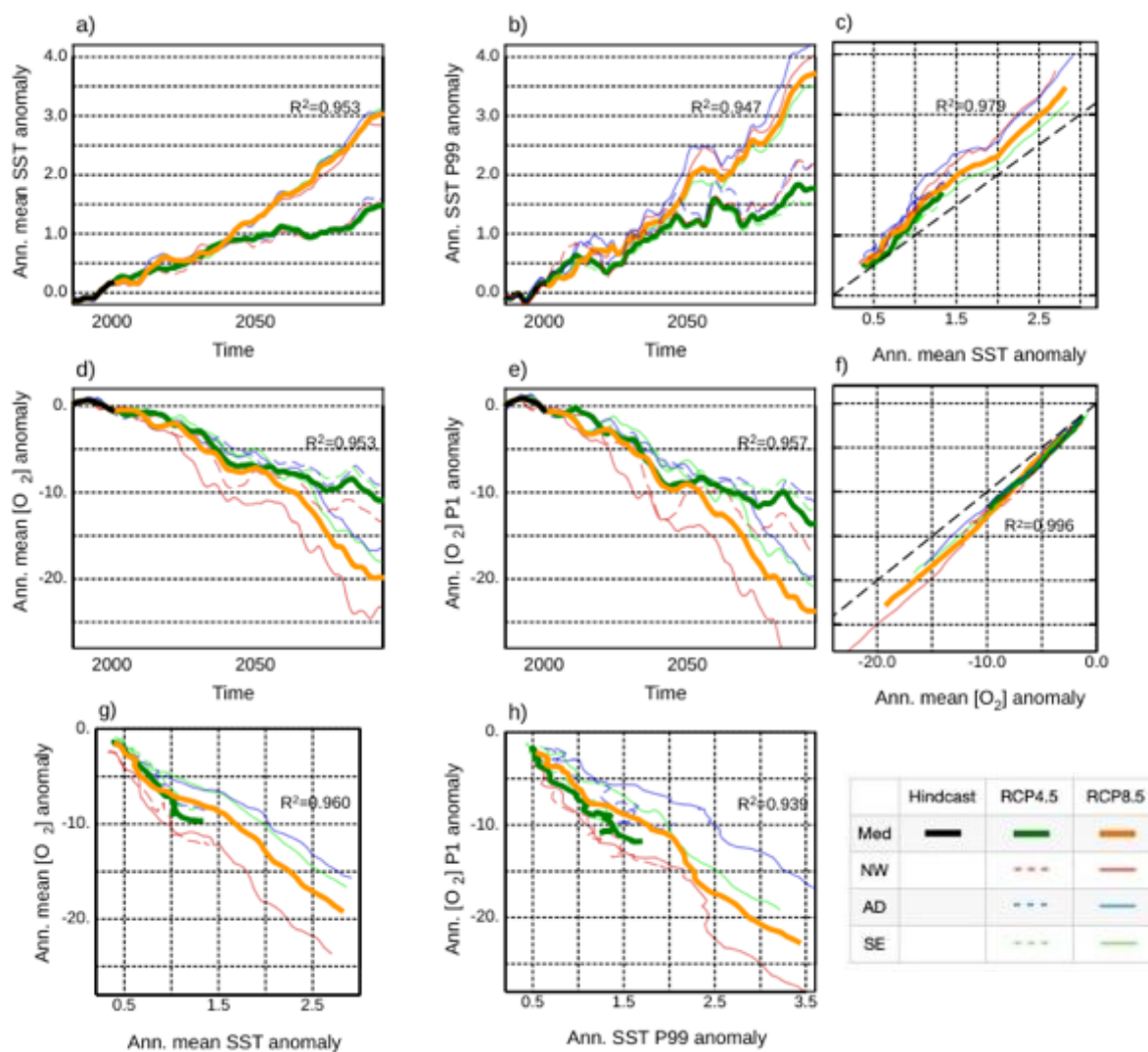


Figure 14: Annual  $SST_{mean}$  (a),  $[O_2]_{(100)mean}$  (d),  $SST_{99P}$  (b), and  $[O_2]_{(100)P}$  (e) anomalies for historical (1982–2005), RCP4.5 and RCP8.5 (2006–2009) within the simulated MS and subbasins. Panels c and f display extreme against mean anomalies for future projections with a dashed black line representing 1:1 ratio. Panels g and h present annual  $[O_2]_{(100)mean}$  against  $SST_{mean}$  anomalies and annual  $[O_2]_{(100)P}$  against  $SST_{99P}$  anomalies. Anomalies are relative to 1982–2005;  $R^2$  values are an average across RCP4.5 and RCP8.5 projections.

Figures 14a shows simulated trends for annual  $SST_{mean}$  as an anomaly relative to historical (1982-2005) POLCOMS-ERSEM outputs for the MS and its subbasins.  $SST_{mean}$

demonstrates a positive trend with time that is weaker in historical relative to RCP projections (*Table 2*). POLCOMS-ERSEM projects a consistent rate of change in SST<sub>mean</sub> from 1982–2045 under both scenarios ( $\sim 0.02^{\circ}\text{C year}^{-1}$ ). Thereafter, simulated warming accelerates under RCP8.5 to  $\sim 0.04^{\circ}\text{C year}^{-1}$  and slows under RCP4.5 to  $\sim 0.01^{\circ}\text{C year}^{-1}$  (*Figure 14a*). These findings are consistent with observed changes to SST<sub>mean</sub> across the historical period (e.g. Pastor et al., 2018; Skliris et al., 2012). A faster rate of change ( $\sim 0.03^{\circ}\text{C year}^{-1}$ ) is reported in satellite data (Merchant et al., 2019) from 1982–2005 with a stronger trend ( $R^2=0.98$ ). Furthermore, Skliris et al. (2012) found a SST<sub>mean</sub> warming rate of  $0.04^{\circ}\text{C year}^{-1}$  and  $0.03^{\circ}\text{C year}^{-1}$  in the eastern Mediterranean (SE and AD) and NW, respectively between 1985–2008 using satellite-derived data. Despite a different reporting period, this suggests that POLCOMS-ERSEM slightly underestimates the trend in annual SST<sub>mean</sub> in the MS over the historic period and is likely conservative in its future projections. This is consistent with the choice of conservative model forcing (MPI-ESM-LR) for the POLCOMS-ERSEM simulation and my validation outlined in *Section 3.2*.

*Figure 14b* displays simulated SST<sub>99P</sub> anomaly across 1982–2099. Once again, the positive trend is weaker across the historical period relative to simulated projections due to the historical signal in NW ( $\sim 0.01^{\circ}\text{C year}^{-1}$ ; *Table 2*). Simulated warming rates for SST<sub>99P</sub> are consistent from historical prior to 2050 at  $\sim 0.02^{\circ}\text{C year}^{-1}$ . Prior to 2050, the SST<sub>99P</sub> warming rate accelerates under RCP8.5 to  $\sim 0.05^{\circ}\text{C year}^{-1}$  to the end of the century but is maintained at  $\sim 0.02^{\circ}\text{C year}^{-1}$  under RCP4.5 (*Figure 14b*). Satellite-derived SST<sub>99P</sub> data shows an increasing trend of  $\sim 0.03^{\circ}\text{C year}^{-1}$  ( $R^2=0.91$ ; *data not shown*; Merchant et al., 2019) with SE showing the fastest regional rate of change ( $\sim 0.04^{\circ}\text{C year}^{-1}$ ). A stronger increase in satellite SST<sub>99P</sub> provides further support that POLCOMS-ERSEM historical SST<sub>99P</sub> is muted relative to observations (*see section 3.2.1.1*).

*Figure 14c* displays  $SST_{99P}$  increasing  $0.006^{\circ}\text{C}$  ( $0.005^{\circ}\text{C}$ )  $\text{year}^{-1}$  faster than relative  $SST_{\text{mean}}$  under RCP8.5 (RCP4.5; *Table 2*).  $SST_{99P}$  in NW and AD shows the fastest rate of change relative to  $SST_{\text{mean}}$  increase with a difference of  $0.011^{\circ}\text{C}$  ( $0.007^{\circ}\text{C}$ )  $\text{year}^{-1}$  under RCP8.5 (RCP4.5). By the end of the century (2076-2099) relative to the historical period, POLCOMS-ERSEM simulated  $SST_{\text{mean}}$  and  $SST_{99P}$  increases by  $2.7^{\circ}\text{C}$  ( $1.3^{\circ}\text{C}$ ) and  $3.3^{\circ}\text{C}$  ( $1.6^{\circ}\text{C}$ ) under RCP8.5 (RCP4.5), respectively. Darmaraki et al. (2019b) find that  $SST_{\text{mean}}$  and  $SST_{99P}$  rise by  $3.1\pm 0.5^{\circ}\text{C}$  ( $1.6\pm 0.8^{\circ}\text{C}$ ) and  $3.6\pm 0.7^{\circ}\text{C}$  ( $1.9\pm 0.9^{\circ}\text{C}$ ) under RCP8.5 (RCP4.5), respectively, clarifying that the conservative nature of SST in POLCOMS-ERSEM is consistent in annual  $SST_{\text{mean}}$  and  $SST_{99P}$ . The multi-model approach of Darmaraki et al. (2019b) includes one MPI-ESM-LR-driven run as well as two additional GCM simulations that comparatively show greater SST warming for the region (McSweeney et al., 2015).

*Figure 14d* shows annual  $[\text{O}_2]_{(100)\text{mean}}$  anomaly from 1982–2099 relative to the historical period within POLCOMS-ERSEM. Simulated rates of decrease for NW, AD and SE are 0.07, 0.04 and  $0.07 \mu\text{mol L}^{-1} \text{year}^{-2}$  (*Table 2*), while observations exhibit changes of  $-0.13$ ,  $+0.02$  and  $-0.13 \mu\text{mol L}^{-1} \text{year}^{-2}$ , respectively. Mavropoulou et al., (2020) report that no long-term trend can be identified in observed  $[\text{O}_2]_{\text{mean}}$  within MS at 0-150 metres depth across 1960–2011. However, annual  $[\text{O}_2]_{(100)\text{mean}}$  from 1982–2005 within their dataset decrease by  $\sim 0.13 \mu\text{mol L}^{-1} \text{year}^{-2}$  across the MS. There is an inconclusive trend and rate of change in observed and simulated AD while the model underestimates  $[\text{O}_2]_{(100)}$  decreases in NW and SE. Similar to mean SST therefore, simulated historical  $[\text{O}_2]_{(100)\text{mean}}$  is generally consistent with observations and captures the differences in rates of change between individual basins.

*Figure 14d* shows strong decreases in RCP projections for  $[\text{O}_2]_{(100)\text{mean}}$  (*Table 2*). Mirroring projected changes in  $SST_{\text{mean}}$ , the rate of decrease in simulated annual  $[\text{O}_2]_{(100)\text{mean}}$  is

$\sim 0.15 \mu\text{mol L}^{-1} \text{ year}^{-2}$  under both scenarios up to  $\sim 2055$ . Subsequently, the rate increases to  $\sim 0.28$  (slows to  $\sim 0.08$ )  $\mu\text{mol L}^{-1} \text{ year}^{-2}$  under RCP8.5 (RCP4.5; *Figure 14d*). By the end of the century,  $[\text{O}_2]_{(100)\text{mean}}$  decreases by 18.7 (9.8)  $\mu\text{mol L}^{-1}$  and under RCP8.5 (RCP4.5), respectively relative to historical. This equates to a loss of 5.9 (4.9) % in  $[\text{O}_2]_{(100)\text{mean}}$  across the MS by the end of the century under RCP8.5 (RCP4.5). In a multi-model study, Bopp et al. (2013) find smaller relative reductions of  $3.45 \pm 0.44$  ( $2.57 \pm 0.30$ ) % in  $[\text{O}_2]$  between 100-600 metres depth under RCP8.5 (RCP4.5) when comparing 2090-2099 to 1990-1999. Three possible factors that could contribute to this disparity are: my focus on 100 metres depth where deoxygenation rates tend to be intensified (Schmidtke et al., 2017); the MS is a semi-enclosed shelf sea compared to the global average across the ocean; the Mediterranean region is a climate change hotspot relative to the global mean. Additionally, divergence between RCPs in  $[\text{O}_2]_{(100)\text{mean}}$  occurs after 2050 while mean SST occurs before (*Figures 14a and 14d*). This suggests a lag in the relationship between surface ocean warming and interior deoxygenation that has been found previously in CMIP5 models (e.g. Bopp et al., 2013).

*Figure 14e* shows simulated annual  $[\text{O}_2]_{(100)1P}$  relative to historical data. While the trend in historical  $[\text{O}_2]_{(100)1P}$  ( $-0.07 \mu\text{mol L}^{-1} \text{ year}^{-2}$ ; *Table 2 and Figure 14e*) matches that for  $[\text{O}_2]_{(100)\text{mean}}$  in NW, no discernible trend exists within simulated historical  $[\text{O}_2]_{(100)1P}$  in AD and SE. *Figure 14e* shows projected  $[\text{O}_2]_{(100)1P}$  to track  $[\text{O}_2]_{(100)\text{mean}}$  under RCP8.5 and RCP4.5. Rates of decrease in  $[\text{O}_2]_{(100)1P}$  exceed those in  $[\text{O}_2]_{(100)\text{mean}}$  by 0.05 (0.02)  $\mu\text{mol L}^{-2} \text{ year}^{-1}$  under RCP8.5 (RCP4.5; *Table 2 and displayed in Figure 14f*) across the MS, suggesting that  $[\text{O}_2]_{(100)1P}$  will decrease 26 (16) % faster than  $[\text{O}_2]_{(100)\text{mean}}$ . NW exhibits the fastest rate of relative change in  $[\text{O}_2]_{(100)1P}$  under RCP8.5.

*Figures 14g and 14h* show the relationships between projected SST<sub>mean</sub> with [O<sub>2</sub>]<sub>(100)mean</sub> and SST<sub>99P</sub> with [O<sub>2</sub>]<sub>(100)1P</sub>. They give the clearest indication of the difference between individual basins, with NW demonstrating the greatest sensitivity to climate change in terms of SST and [O<sub>2</sub>]<sub>(100)</sub> relative to the entire MS. The last decade of the century sees sharper warming and deoxygenation under RCP4.5. A possible cause could be strong positive Atlantic Multidecadal Oscillation (AMO) signal in the model's atmospheric forcing contributing to persistent warming. The AMO affects summertime conditions in Europe and was a contributing factor in the 2003 European heatwave (Sutton, 2005), but CMIP5 models have been shown to overestimate short-term (10-20 years) AMO variability (Ruiz-Barradas et al., 2013). A limitation of this study is that atmospheric forcing has not been considered. Within this study, I use >20-year averages of simulated data to reduce the influence of interannual and decadal variability on MHW and MOL events.

In summary, *Figure 14* shows that mean and extreme SST ([O<sub>2</sub>]<sub>(100)</sub>) increase (decrease) with time towards the end of the century under RCPs. Divergence between RCP4.5 and RCP8.5 occurs around the midpoint of the 21<sup>st</sup> century. SST<sub>99P</sub> ([O<sub>2</sub>]<sub>(100)1P</sub>) anomalies increase (decrease) at a faster rate than their respective mean anomalies, with NW and AD showing a stronger intensification of the extremes compared with SE.

#### 4.1.1.2 End-of-the-century changes

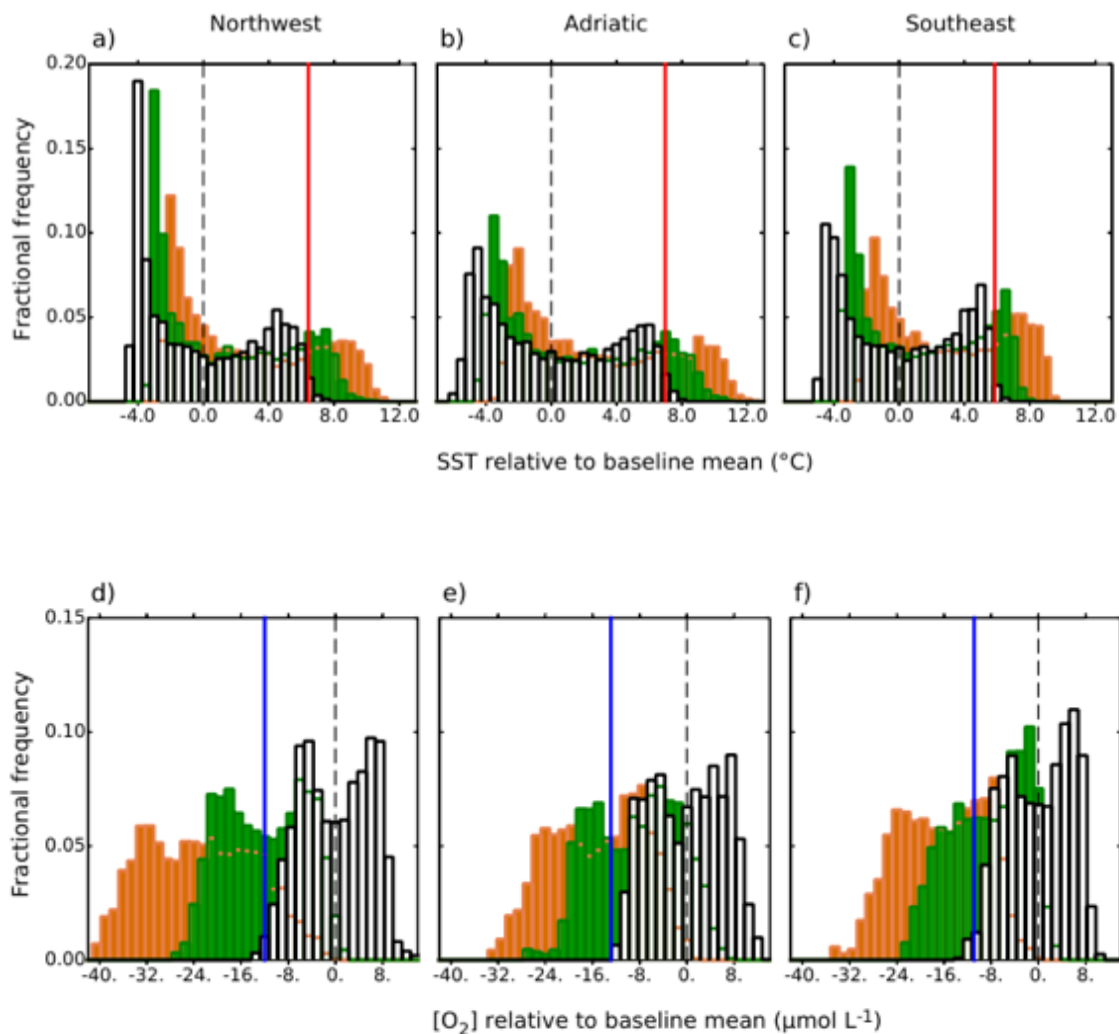


Figure 15: Basin averaged fractional frequency of daily mean SST (a b and c) and daily mean [O<sub>2</sub>]<sub>(100)</sub> (d, e and f) for baseline period (black/white; 1982-2005) and RCP4.5 and 8.5 (green and orange, respectively; 2076-2099) relative to baseline mean values. Vertical red lines show baseline SST<sub>99P</sub> and blue lines show baseline [O<sub>2</sub>]<sub>(100)1P</sub>.

Figure 15 shows simulated fractional frequency distributions of basin averaged daily SST and [O<sub>2</sub>]<sub>(100)</sub> for the historical and end-of-the-century model output. Figures 15a, b and c depict SST warming shifts from historical to the end of the century under RCP8.5 (RCP4.5) in: SST<sub>mean</sub> by 2.7°C (1.3°C); SST<sub>99P</sub> by 3.3°C (1.6°C). The range of simulated SSTs in NW, AD and SE change by +1.69°C (+1.11°C), +1.07°C (-0.43°C) and -0.08°C (-0.21°C). NW and AD exhibit the largest expansions in range under RCP8.5 as well as the fastest



rate of increase in SST<sub>99P</sub> (*Figure 14c*). Historical extremes (red lines) become the new summertime norm indicating a lengthening of summertime conditions within the MS under climate change.

The decrease in  $[O_2]_{(100)\text{mean}}$  of 18.7 (9.8)  $\mu\text{mol L}^{-1}$  by the end of the century (*Figure 14d*) is demonstrated by the significant shift to the left in fractional frequency in each basin in *Figures 15d, e and f*. Historical  $[O_2]_{(100)1P}$  (blue lines) becomes the “new norm” under RCP4.5, while historical  $[O_2]_{(100)\text{mean}}$  (dashed line) represents an extreme positive deviation in NW and SE under RCP8.5. Ranges of  $[O_2]_{(100)}$  expand by 7.02 (4.43), 5.3 (3.42) and 10.3 (2.93)  $\mu\text{mol L}^{-1}$  in NW, AD and SE, respectively under RCP8.5 (RCP4.5). The faster rate of decrease in  $[O_2]_{(100)1P}$  relative to  $[O_2]_{(100)\text{mean}}$  (*Figure 14f*) and the expansion in the range of  $[O_2]_{(100)}$  by the end of the century means there is a higher frequency of extreme low oxygen values in the lower tail of the distribution.

#### 4.1.2 Changes in spatial patterns

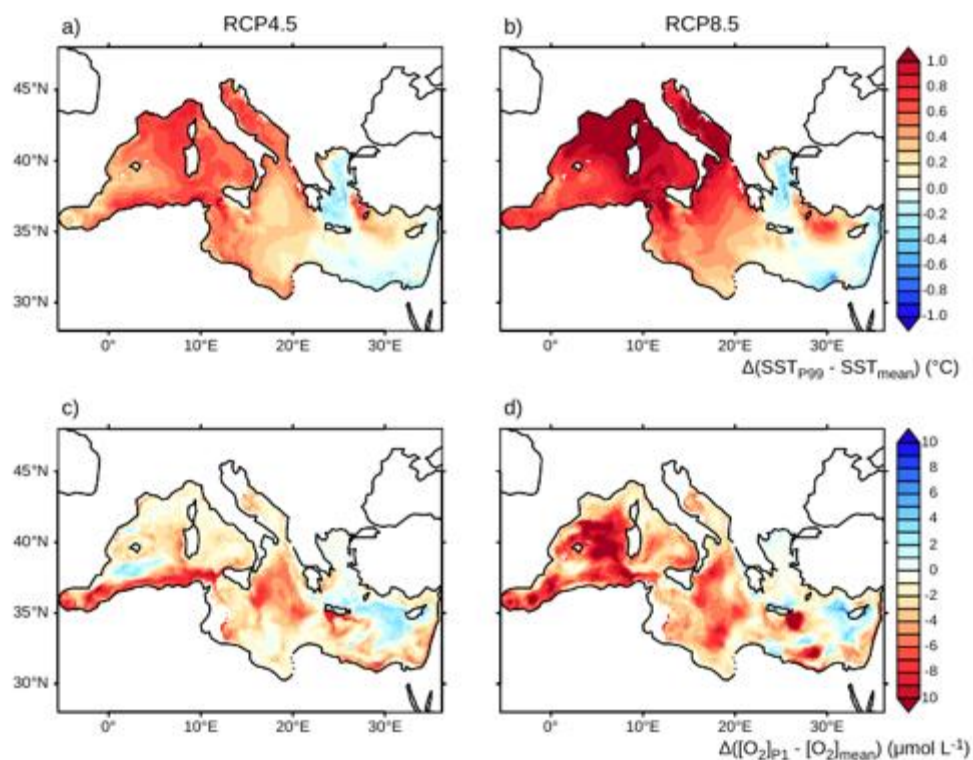


Figure 16: Changes to extremes ( $SST_{P99}$  and  $[O_2]_{(100)P1}$ ) relative to  $SST$  and  $[O_2]_{(100)}$  means. Relative mean for each 24-year period (historical [1982-2005]; RCP4.5 and RCP8.5 [2076-2099]) is subtracted from the relative P99 (P1) and expressed as the difference between the two periods. Red areas indicate extremes have changes more than means.

Figure 16b (a) shows the difference between historical and end-of-the-century  $SST_{P99}$  minus  $SST_{mean}$  across the simulated MS under RCP8.5 (RCP4.5). The majority of the MS shows projected changes in  $SST_{P99}$  to exceed  $SST_{mean}$ , supporting results presented in Figure 14c and other ocean model projections (e.g. Darmaraki et al., 2019b). Figures 16a and b highlight the amplification of similar spatial patterns between RCP4.5 and RCP8.5. A clear east-west divide suggests NW and AD extremes are more sensitive to climate change than SE; here, the intensification of  $SST_{P99}$  compared to  $SST_{mean}$  demonstrates consistency with the subbasin differences displayed in Figure 14c. The regions showing the greatest simulated change in  $SST_{P99}$  minus  $SST_{mean}$  in my study agree with projections

made by Darmaraki et al. (2019b) and correspond spatially with the areas most affected during the 2003 MHW (Garrabou et al., 2009; Olita et al., 2007; Sparnocchia et al., 2006).

*Figure 16d (c)* shows the change in  $[O_2]_{(100)1P}$  minus  $[O_2]_{(100)mean}$  under RCP8.5 (RCP4.5). Once again, the rate of change in  $[O_2]_{(100)1P}$  exceeds that of  $[O_2]_{(100)mean}$  for most of the basin but with larger inconsistencies in spatial patterns between RCPs when compared with *Figures 16c and d*. Most notably, portions of NW that exhibit little difference ( $<4 \mu\text{mol L}^{-1}$ ) under RCP4.5 show large differences ( $>10 \mu\text{mol L}^{-1}$ ) under RCP8.5. Therefore, an east-west divide is difficult to discern in  $[O_2]_{(100)1P}$  minus  $[O_2]_{(100)mean}$  under RCP4.5 but is more recognisable under RCP8.5. A notable consistency between RCPs is the AJ where changes in  $[O_2]_{(100)1P}$  greatly exceed those in  $[O_2]_{(100)mean}$ . The influence of relatively nutrient-rich inflow that drives primary production in this region means greater export and remineralisation may be contributing to MOL events at 100 metres depth. The uniformity between RCPs suggests this process is the dominant control rather than temperature-controlled affects such as reduced solubility and ventilation. It is important to consider the impact of overstated riverine input from the Rhône (*see section 3.1.4*) potentially rendered some areas of NW unreliable in terms of biogeochemistry. However, *Figures 16c and d* demonstrate that extremes in  $[O_2]_{(100)}$  around the Rhône are comparable to the rest of the basin; SST is unaffected by biogeochemical boundary conditions.

The main focus of subsequent work within my thesis is the relationship between MHW and MOL events under RCP4.5 at the end of the century (*section 2.4; question 3*). The ranges of MHW category ( $Cat_{max}$  minus  $Cat_{min}$ ) and intensity ( $Int_{max}$  minus  $Int_{min}$ ) across 2076-2099 are marginally greater under RCP4.5 ( $Cat_{range}=5.51$ ;  $Int_{range}=2.97^\circ\text{C}$ ) compared to RCP8.5 ( $Cat_{range}=5.32$ ;  $Int_{range}=2.96^\circ\text{C}$ ). The difference between RCP4.5 and

RCP8.5 is amplified in NW (RCP4.5  $\text{Cat}_{\text{range}}=6.33$ ,  $\text{In}_{\text{range}}=3.76^{\circ}\text{C}$ ; RCP8.5  $\text{Cat}_{\text{range}}=5.08$ ,  $\text{In}_{\text{range}}=3.27^{\circ}\text{C}$ ) and AD (RCP4.5  $\text{Cat}_{\text{range}}=4.7$ ,  $\text{In}_{\text{range}}=3.65^{\circ}\text{C}$ ; RCP8.5  $\text{Cat}_{\text{range}}=4.23$ ,  $\text{In}_{\text{range}}=3.34^{\circ}\text{C}$ ) where climate change appears to have the largest impact (*as in Figures 14c, 16a and 16b*). Given my analysis is concerned with determining differences between high and low category and intensity MHWs, it follows that RCP4.5 is a justifiable focus for my study. Furthermore, RCP4.5 is a more realistic projection which can better inform policy as opposed to RCP8.5 which is a low likelihood, high-end scenario (Hausfather and Peters, 2020).

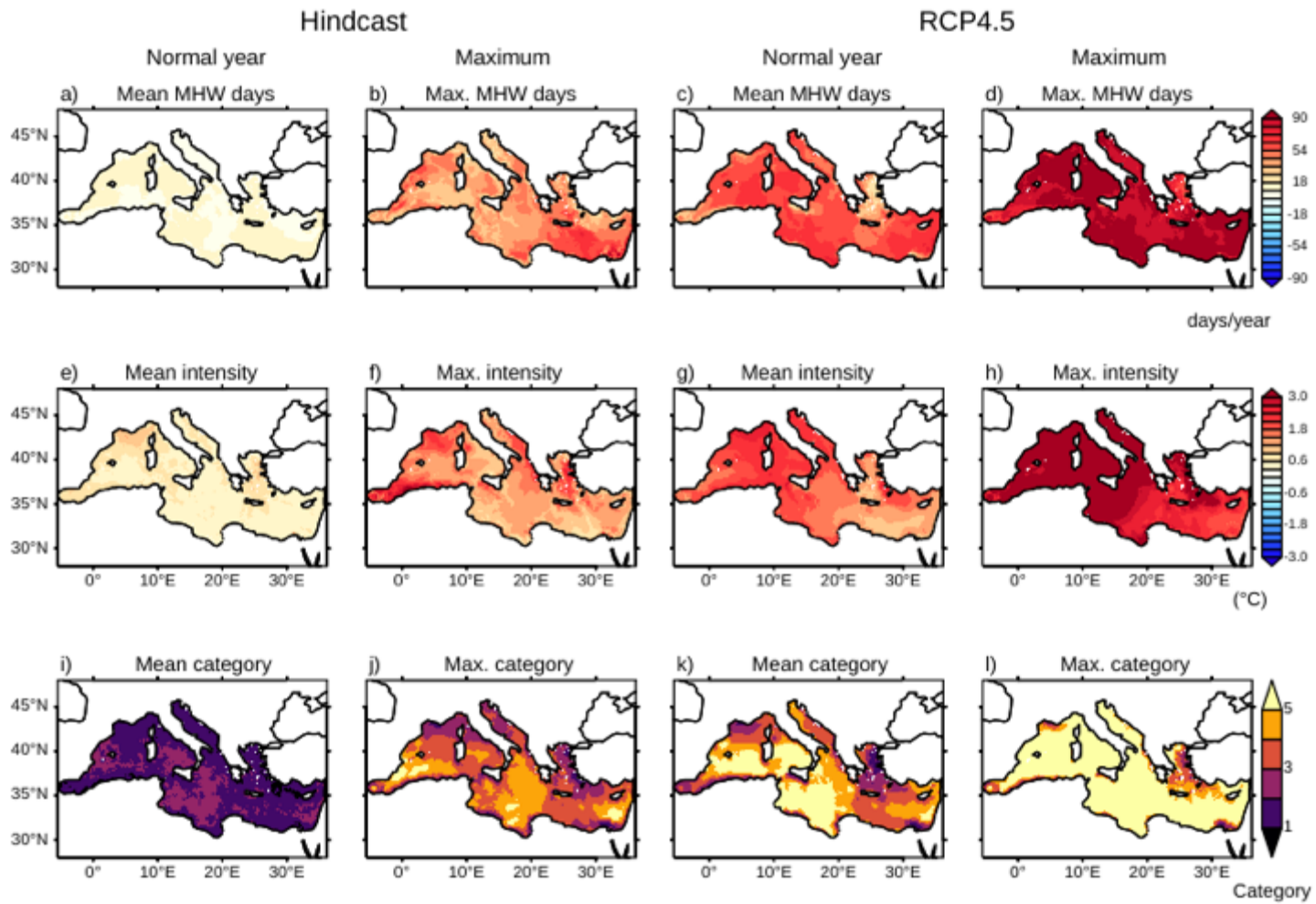


Figure 17: Historical (1982-2005; left six panels) and end-of-the-century (RCP4.5; 2076-2099; right six panels) MHW characteristics. 'Normal year' (mean) MHW days (a and c), intensity above the 99<sup>th</sup> percentile (e and g) and category (i and k) are displayed, along with maximum MHW days (b and d), intensity (f and h) and category (j and l) for each grid cell across each 24-year period.

## 4.2 MHW and MOL event diagnostics

### 4.2.1 MHW characteristics

*Figure 17* maps historical and end-of-the-century RCP4.5 'normal year' and maximum MHW characteristics for frequency, intensity and category (see *Table 2* for overall regional MHW characteristics). 'Normal year' refers to the average annual maximum for each characteristic, while 'Maximum' is the highest value across the 24-year period. In general terms, historical maximum MHW characteristics (frequency - *Figure 17a*; duration - *Table 2*; intensity - *Figure 17e*; category - *Figure 17i*) are exceeded by 'normal year' end-of-the-century RCP4.5 events (*Figures 17c, g and k*) and constitute a low intensity event under RCP8.5 (*Table 2* & Darmaraki et al., 2019b). Across the year, an historic one-in-hundred-day MHW will become a one-in-six-day event under RCP4.5 and a one-in-four-day event under RCP8.5. These considerable increases in MHW frequency are in accordance with global projections using the same percentile-based methodology (Frölicher et al., 2018). Frölicher et al. (2018) find that a pre-industrial one-in-hundred-day event will become a one-in-three-day event under RCP8.5; the disparity between this study and my own results is most likely caused by the differing baseline periods.

*Figure 17c* displays most of the MS experiencing a maximum of >90 non-consecutive MHW days (normal year=57.3; *Table 2*) in a year by the end of the century under RCP4.5 equating to an entire summer which will become the norm under RCP8.5 (*Table 2*). The average duration of an individual event will be 94 (52) days under RCP8.5 (RCP4.5; *Table 2*). This is in good agreement with a multi-model study that finds end-of-the-century RCP8.5 (RCP4.5) MHW duration to be  $94.1 \pm 9.9$  ( $59.0 \pm 10.0$ ) days using the same detection method (Darmaraki et al., 2019b – *Table 5*).

A distinct east-west divide is also visible in end-of-the-century MHW intensity (*figure 17g and 17h*). Under RCP4.5, NW and AD experience mean MHW intensities of 2.10°C and 2.16°C, respectively, while the same measure for SE is 1.59°C (*Table 2*). Therefore, SE experiences a greater number of MHW days at a lower intensity relative to NW and AD, where shorter yet more intense events occur. Maximum event intensity as expected shows a similar yet more pronounced division, with most intense MHW events in NW and AD (4.28°C and 4.17°C above SST<sub>99P</sub> compared to 2.86°C in SE; *Table 2* and displayed in *Figure 17h*). Regional hotspots of MHW intensity across the MS mirror the disproportionate amplification of SST<sub>99P</sub> minus SST<sub>mean</sub> (*Figure 16a and b*). SST<sub>99P</sub> in NW and AD rise 1.35 (1.5) times faster than SST<sub>mean</sub> compared with SE where the rate is 1.1 (1.2) times under RCP8.5 (RCP4.5). NW and AD have experienced the most damaging ecosystem impacts from MHWs over the recent past (see section 2.3.2) with these results suggesting heightened sensitivity at the end of the century. However, while simulations suggest events in NW and AD are more intense at the surface (*Figure 17e–h*), SE events penetrate deeper into and affect a greater portion of the water column (Darmaraki et al., 2019a), likely due to their more prolonged nature. SE shows the greatest ‘normal year’ event duration by the end of the century lasting 100 (53) days (*Table 2*).

Normal year event category in the historical simulation is  $\leq 1$  (*Figure 17i*) with only small portions of the MS experiencing category 5 events (*Figure 17j*). By the end of the century however, nearly the entirety of the MS will have experienced a category 5 MHW under RCP4.5 (*Figure 17l*), while category 7 becomes the norm under RCP8.5 (*Table 2*). It is important to note that maximum historical MHW category (*Figure 17j*) tends to be low in regions where mean and maximum intensity are elevated (*Figure 17e and f*). MHW categories encompass a greater range of SSTs above SST<sub>99P</sub> in regions where exceedances

are more frequent and larger; that is, categorisation is proportional to the most intense regional events. Essentially, this means that projected MHW categories are less sensitive (a lower category is more likely at the end of the century) in areas that experience historical events of greater intensity, and regions that have only experienced low intensity historical events are more likely to yield higher category events at the end of the century.



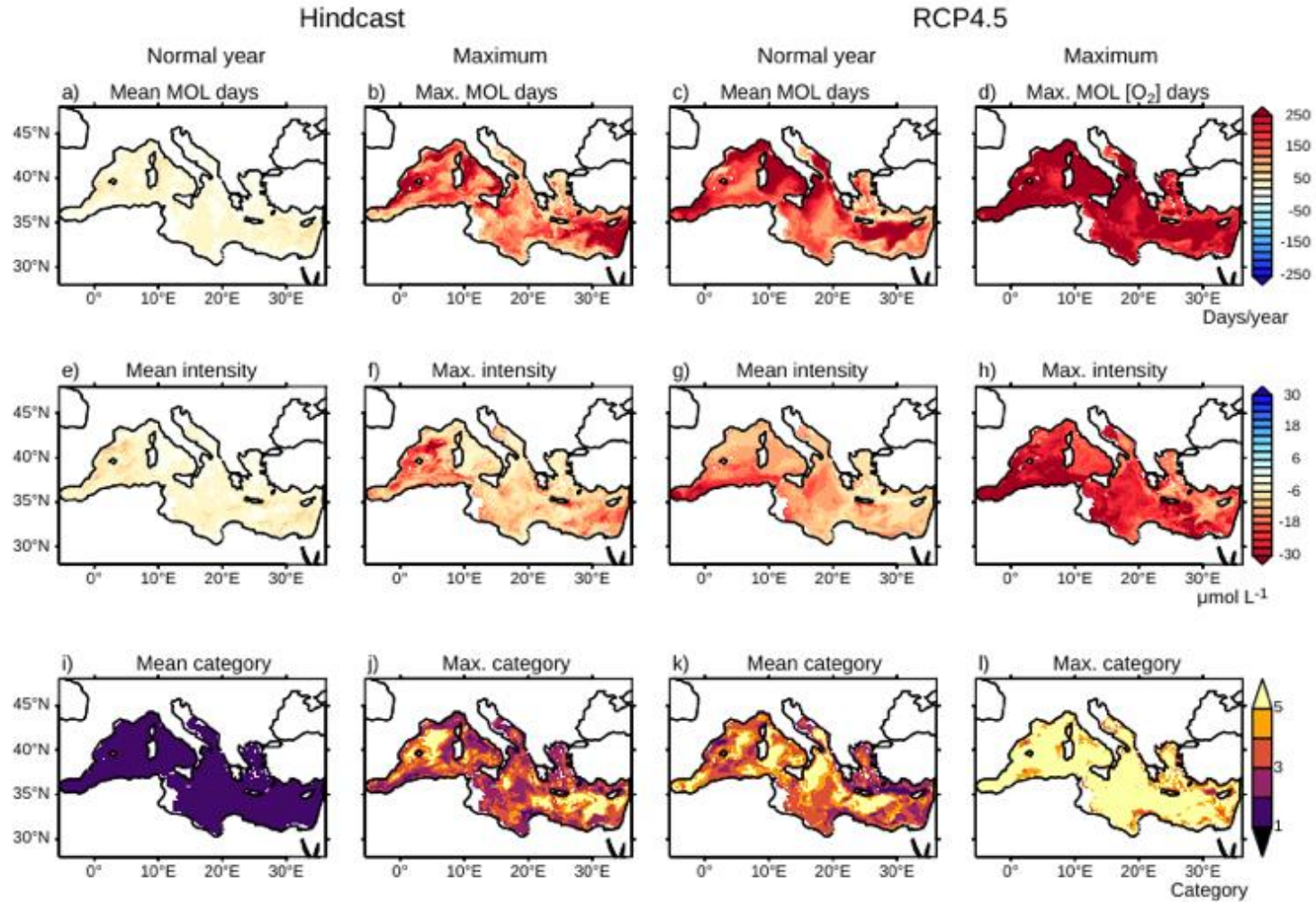


Figure 18: Historical (1982-2005; left six panels) and end-of-the-century (RCP4.5; 2076-2099; right six panels) low oxygen event characteristics. 'Normal year' (mean) low [O<sub>2</sub>] days (a and c), mean intensity below the 1<sup>st</sup> percentile (e and g) and category (i and k) are displayed, along with maximum low [O<sub>2</sub>] days (b and d), minimum intensity (f and h) and maximum category (j and l) for each grid cell across each 24-year period.

#### 4.2.2 MOL event characteristics

*Figure 18* displays analysis of POLCOMS-ERSEM MOL event characteristics for ‘normal year’ and maximum frequency. Once again, ‘normal year’ refers to average annual maximum for each characteristic while ‘Maximum’ refers to the highest value across the 24-year period. It is important to note I use ‘Maximum’ to refer to intensity of deoxygenation below  $[O_2]_{(100)1P}$ . The MS will experience unprecedented MOL events by the end of the century under RCP4.5 (*Figure 18*) which intensify under RCP8.5 (*Table 2*). There is a complicated spatial relationship in changing MOL events from historical to projected simulations (*Figure 18*). An end-of-the-century normal year MOL event generally matches the spatial distribution of maximum historical event characteristics in frequency (*Figure 18b and c*), intensity (*Figure 18f and g*) and category (*Figure 18j and k*). However, characteristics are less regionally coherent when compared with the changes between historical and end of the century MHWs (*figure 17*). For example, portions of the Levantine basin experience similar event maximum frequency of  $\sim 250$  days/year (*Figures 18b and d*) along with stronger low oxygen event intensities in historical ( $\sim 15 \mu\text{mol L}^{-1}$ ) than in RCP4.5 ( $\sim 10 \mu\text{mol L}^{-1}$ ; *Figures 18f and h*). Despite these spatial inconsistencies between historical and RCP4.5 for large portions of the basin, *Figures 18b-d and f-h* highlight that the AJ exhibits particular sensitivity to MOL events. Under RCP4.5, mean event intensity is elevated relative to the rest of the MS (*Figure 18g*). Relative to the NW average, AJ MOL event mean (maximum) intensity is  $\sim 1.4-7.4$  ( $\sim 0-5.5$ )  $\mu\text{mol L}^{-1}$  below  $[O_2]_{(100)1P}$  in historical and  $\sim 2.3-14.3$  ( $\sim 1.5-41.0$ )  $\mu\text{mol L}^{-1}$  below  $[O_2]_{(100)1P}$  in RCP4.5.

Relative to the historical simulation, MS  $[O_2]_{(100)\text{mean}}$  decreases to such an extent by the end of the century that  $[O_2]_{(100)}$  values are lower than  $[O_2]_{(100)1P}$  for 269 (173) days per

year. The maximum number of MOL days per year reaches 338 (275) under RCP8.5 (RCP4.5; *Table 2*). This means that a one-in-a-hundred-day MOL will become a three-in-four-day (one-in-two-day) MOL under RCP8.5 (RCP4.5). The rate of change for both MHWs and MOL events relative to respective  $SST_{99P}$  and  $[O_2]_{(100)1P}$  are consistent. Mean MHW intensities are 6.0 (3.1) times more severe under RCP8.5 (RCP4.5) while MOL event intensities are 5.5 (3.1) times more severe. Similarly, MHW and MOL maximum intensities both strengthen by 3.3 (2.3) times under RCP8.5 (RCP4.5).

#### 4.2.3 Event sequencing and seasonality

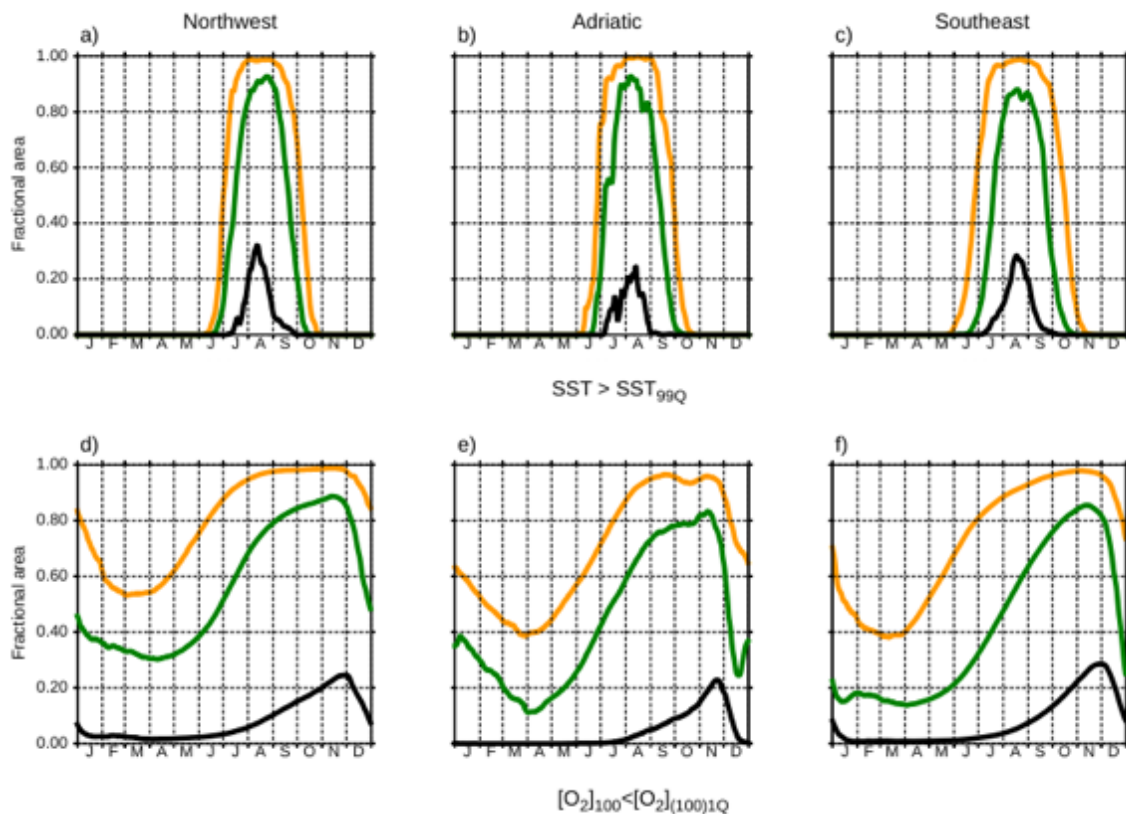


Figure 19: ‘Normal year’ fractional area of each MS basin experiencing a MHW and MOL for hindcast (black; 1982-2005), RCP4.5 (green; 2079-2099) and RCP8.5 (orange; 2076-2099).

My analysis suggests that ~0.99 (~0.89) of the fractional area of simulated MS will experience MHW conditions in a ‘normal year’ by the end of the century under RCP8.5

(RCP4.5; *Table 2*). There is also good consistency between basins (*Figures 19a, b and c*). Contrary to my results, multi-model analysis suggests that maximum MHW surface coverage is 0.55 (0.45) by the end of the century (Darmaraki et al., 2019b). Darmaraki et al. (2019b) focus on long-lasting MHWs and remove any occurrences that are less than 5 days in duration (after Hobday et al., 2016). Instead, I include every threshold exceedance in my calculation of fractional area coverage. The disparity would likely be reduced if I were to remove MHW occurrences that were <5 days.

Simulated historical MHWs occur from July to September. The end of the century sees a drastic expansion in their temporal range: RCP8.5 (RCP4.5) MHWs occur from May–November (June–October; *Figures 19a, b and c*). Given that MS MHW events are driven primarily by atmospheric heating, this expansion of the temporal range points to a lengthening of summertime conditions. Coma et al. (2009) used water column temperature differences as a proxy for stratification, a feature typical of the MS in summer. Between 1974–2006, summertime conditions expanded by 40% (Coma et al., 2009). MS MHWs occur during calm conditions and contribute to water column stratification (Cerrano et al., 2000; Sparnocchia et al., 2006). Therefore, stronger and more prolonged water column stratification should be expected by the end of the century as a result of the broadening window of MHW occurrence in the MS.

*Figure 19d, e and f* show that the fractional coverage of MOL events will expand from 0.27 in historical to 0.98 (0.87) in a ‘normal year’ at the end of the century under RCP8.5 (RCP4.5). MOLs will occur throughout the average seasonal cycle by the end of the century having been limited from ~June to January for the entire MS in the historical simulation. Furthermore, maximum fractional area coverage will shift from late November (early November) to late October under RCP8.5 (RCP4.5) with the most

significant difference seen in the Adriatic (*Figure 19e*). Given the oligotrophic nature of the MS, the spatial expansion of MOLs is most likely the result of changes to ventilation. In each basin, peak fractional area coverage of MOL events temporally follows the corresponding peak in MHW coverage, suggesting that increased stratification may be contributing to simulated MOL events.

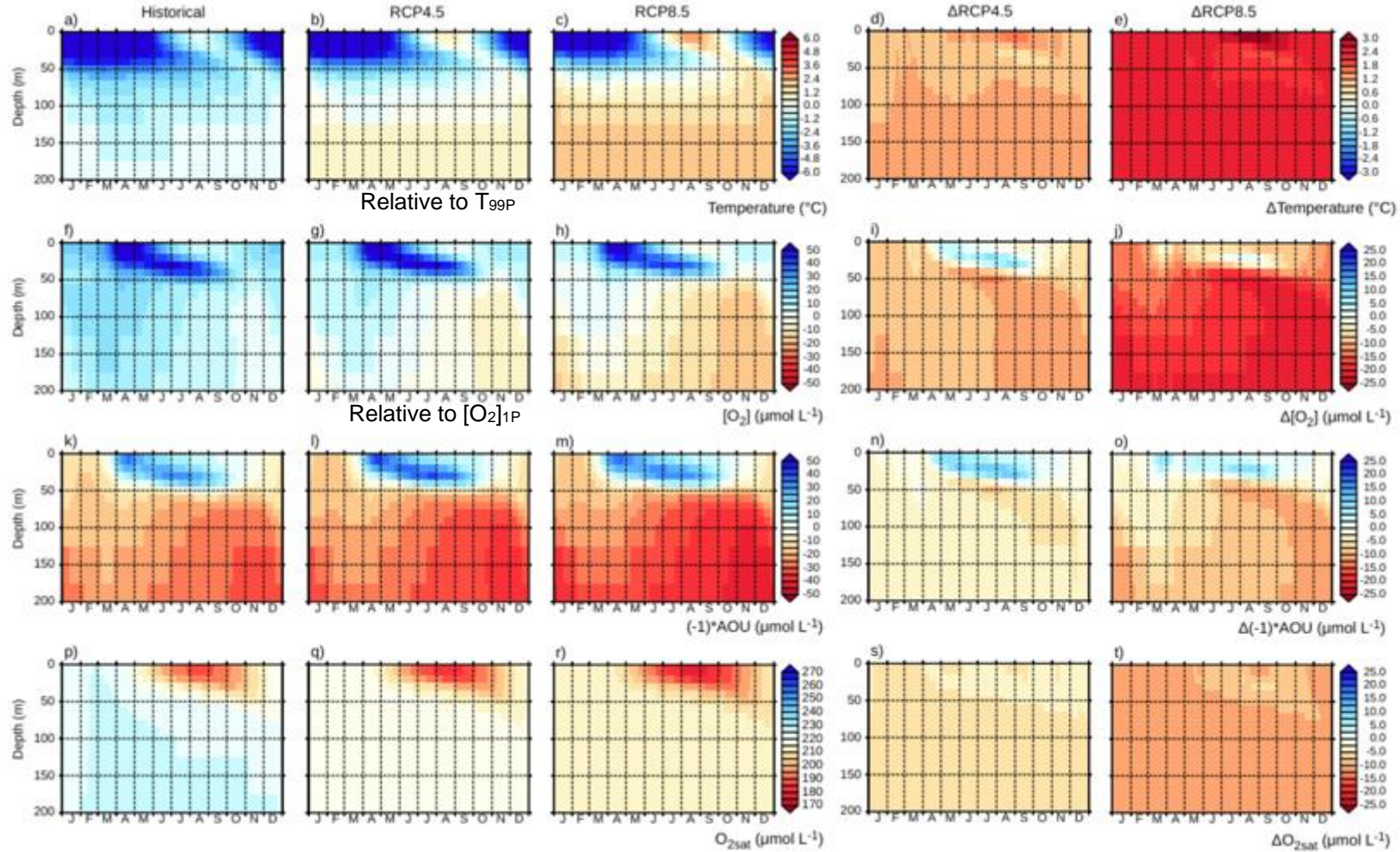


Figure 20: Depth-time Hovmöller plots (0-200 m) for historical (1982-2005; a, f, k and p), RCP4.5 (2076-2099; b, g, l and q) and RCP8.5 (2076-2099; c, h, m and r) along with end-of-the-century change in RCP4.5 (d, i, n and s) and RCP8.5 (e, j, o and t) for the MS in temperature ( $^{\circ}\text{C}$ ; a-e),  $[O_2]$  ( $\mu\text{mol l}^{-1}$ ; f-j),  $(-1)*\text{AOU}$  ( $\mu\text{mol l}^{-1}$ ; k-o) and  $O_{2\text{sat}}$  ( $\mu\text{mol l}^{-1}$ ; p-t). For temperature and  $[O_2]$ ,  $T_{99P}$  and  $[O_2]_{1P}$  thresholds are represented by zero so that yellow through red shading indicates extremes. AOU has been inverted so that the colour key matches  $[O_2]$  and  $O_{2\text{sat}}$ .

*Figure 20* displays 'normal year' (climatological mean) temperature,  $[O_2]$ , AOU and  $O_{2sat}$  for upper 200 metres of the water column. By design, a MHW is not the norm in the simulated historical surface layer (upper 50 metres; *Figure 20a*). However,  $T > T_{99Q}$  by 2.4-3.0°C (1.2-1.8°C) at the end of the century under RCP8.5 (RCP4.5; *Figures 20b and c*). The MHW develops in the upper 20 metres of the water column and propagates downwards from late summer through autumn. This downward transport of heat contributes to an intensification of a positive subsurface (>50 metres depth) temperature signature under RCPs in autumn.

End-of-the-century mean temperature change for the upper 200 metres of the water column is largely uniform throughout the year at 2.4-2.7°C (1.2-1.5°C) under RCP8.5 (RCP4.5; *Figures 20d and e*). However, mean summertime temperatures in upper 30 metres of the water column increase by >3.0°C (1.5-1.8°C). Slower increases are evident in the region of the water column directly beneath the summer MHW (0.6-0.9 and 1.8-2.1°C), indicating a shoaling of the mixed layer and entrainment of heat in the upper 20 meters. Thermal stratification is typically observed in regions of NW (e.g. Marty et al., 2002; Mena et al., 2019), AD (e.g. Santinelli et al., 2013) and SE (e.g. Ramfos et al., 2006) during summer. Coma et al. (2009) found a doubling in frequency of days the difference in seawater temperature between 20 and 80 metres depth was >18°C in NW indicating an expansion to thermal stratification. My results suggest that historical increases in MS thermal stratification are likely to continue under future RCPs, as has been reported by other studies using CMIP projections for the open ocean (e.g. Capotondi et al., 2012).

*Figure 20f* shows that historical mean  $[O_2] > [O_2]_{1P}$  throughout the seasonal cycle in the upper 200 metres of the water column as is expected by the experimental design. By the end of the century relative to historical, the rate of deoxygenation is greatest in the spatiotemporal region where MOLs occur (August to December at 50–200 metres depth). A MOL event becomes the norm (*Figures 20g and h*) enduring for 268 days (148 days) under RCP8.5 (RCP4.5) at 100 metres depth (*Table 2*). Under RCPs, MOL duration increases with depth from 50 metres where extreme values become the norm under RCP8.5 at 200 metres (*Figure 20h*). Mean event intensity peaks around the beginning of October until mid-December with  $[O_2]_{(100)} < [O_2]_{(100)1P}$  by 22.9 (12.8)  $\mu\text{mol L}^{-1}$  (*Table 2*). Extreme  $[O_2]$  values below  $[O_2]_{1P}$  reduce by 20–22.5 (10–12.5)  $\mu\text{mol L}^{-1}$  relative to the historical simulation (*Figures 20i and j*) exceeding the rate of change in annual mean deoxygenation (*see section 4.1, Figures 14d-f*).

*Figures 20k-m and p-r* show that changes in  $[O_2]$  are driven by a combination of AOU and  $O_{2\text{sat}}$  signals. There is a positive relationship between end-of-the-century changes to  $[O_2]$  and AOU (*Figures 20 i, j, n and o*). The greatest decreases in  $(-1) \cdot \text{AOU}$  of 12.5–15 (7.5–10.0)  $\mu\text{mol L}^{-1}$  begin in July at 50 metres depth and propagate downwards to 200 (125) metres depth by October (September) under RCP8.5 (RCP4.5). These excursions in the AOU signal match the timing of the seasonal MOL event. The positive relationship between the timing of the MOL and the AOU signal suggests that subsurface MOLs are driven by stratification or increased organic matter export.

Net primary production (NPP) is projected to remain unchanged for the majority of the MS in POLCOMS-ERSEM with small increases ( $< 1 \text{ g C m}^{-2} \text{ day}^{-1}$ ) simulated by the end of the century in NW under RCP8.5 and RCP4.5 (Kay et al., 2018). Other model studies suggest that the MS will become more oligotrophic after 2050 (e.g. Pagès et al., 2020).



Given simulated changes to temperature in the surface and the oligotrophic nature of the MS, stratification is likely the most significant contributor to MOL events within the AOU signal. As MHW intensity enhances thermal stratification and MOL events appear controlled by the AOU signal, it follows that MHW peak intensity may exert influence on the AOU and MOL signals.

In the upper 200 metres of the water column across the annual cycle,  $O_{2sat}$  exhibits a greater influence on mean deoxygenation than AOU by the end of the century relative to the historical simulation (*Figures 20n, o, s and t*). An inverse relationship is evident within the model between surface temperature and  $O_{2sat}$ . The lowest  $O_{2sat}$  response of 7.5-12.5 (7.50-10)  $\mu\text{mol L}^{-1}$  occurs under RCP8.5 (RCP4.5) within the lengthened summer period between 20-50 metres depth underlying the summer MHW (*Figures 20s and t*). However, changes in  $O_{2sat}$  during the MHW (0-20 metres depth) do not exceed the mean rate of change for the upper 200 metres, most likely because the surface remains well-mixed and ventilated during events. Findings from *Figure 20* suggest that  $O_{2sat}$  controls mean changes to deoxygenation in the upper 200 metres of the water column, while the influence of AOU is greater during MOL events between 80-200 metres depth. Annually between 50-200 metres depth, AOU contributes 44 (42) % of  $[O_2]$  change by the end-of-the-century under RCP8.5 (RCP4.5); during October – December when MOL events are most intense, this contribution rises to 48 (45) % (*Figure 20*). This means that  $O_{2sat}$  accounts for 52-58% of  $[O_2]$  changes which is in accordance with findings from Frolicher et al. (2009) where solubility accounts for 50% of the change in  $[O_2]$ .

#### 4.3 MHW event intensity and category comparison

My analysis has supported previous findings that severe and prolonged MHWs become more frequent under RCPs in the MS (e.g. Darmaraki et al., 2019b). I have also shown that

thermal stratification is simulated to intensify in the basin as a result of warming and MHW events. Furthermore, I have demonstrated for the first time that simulated MOL events follow the same pattern of increasing frequency, intensity and duration as MHWs towards the end of the century and are likely driven by thermal stratification. The question remains as to whether the severity of MHW events affects the intensity of a MOL event. To explore the relationship between MHWs and MOLs, I use POLCOMS-ERSEM simulated end-of-the-century (2076-2099) RCP4.5 temperature,  $[O_2]$  and AOU data. For each of the 24 years, I separated surface and subsurface (0-200 metres) output into two groups based on annual maximum SST. The two groups are High Intensity ( $SST_{max} \geq SST_{99Q} + 1.5^\circ C$ ) and Low Intensity ( $SST_{max} < SST_{99Q} + 1.5^\circ C$ ). For example, if a region experienced a High Intensity MHW in a year, then the surface layer and all underlying model output would be separate into that group. A climatological mean was then calculated from each group to give the mean High Intensity and Low Intensity MHW events and their effects on water column temperature,  $[O_2]$  and AOU (*see Table 3*). This process was repeated for High Category ( $SST_{max} \geq$  MHW category 2) and Low Category ( $SST_{max} <$  MHW category 2; *see Table 4 for results and Figure 9b for categorisation methodology*). As previously outlined, RCP4.5 output is used once more as opposed to the low likelihood RCP8.5 scenario (Hausfather and Peters, 2020).

#### 4.3.1 Intensity comparison

*Table 3: Summary of average Low Intensity ( $SST_{max} < SST_{99Q} + 1.5^\circ C$ ) and High Intensity ( $SST_{max} \geq SST_{99Q} + 1.5^\circ C$ ) MHW events characteristics across 2076-2099 and their corresponding MOL, AOU and  $O_{2sat}$  responses. MOL and AOU responses are based on 100 metres for the months of October, November and December during MOL peak intensity. MHW (MOL) anomalies are relative to  $SST_{99P}$  ( $[O_2]_{1P}$ ) with means representing the average value during the event, and maximums the most extreme positive (negative) deviation of spatially averaged data. AOU values represent autumn at 100 metres depth*

while  $O_{2sat}$  values represent summer at 0-10 metres; both are relative to the RCP4.5 end-of-the-century (2076-2099) mean and maximum represents the most extreme negative value.

	RCP4.5 (2076-2099)							
	Whole	NW	AD	SE	Whole	NW	AD	SE
<b>MHW characteristics</b>	Low ( $SST_{max} < SST_{99Q} + 1.5^{\circ}C$ )				High ( $SST_{max} \geq SST_{99Q} + 1.5^{\circ}C$ )			
Mean MHW SST	0.4	0.4	0.1	0.4	1.0	1.1	1.0	0.9
Max. MHW SST	0.5	0.5	0.2	0.6	1.5	1.7	1.8	1.5
MHW days/year	43	35	19	48	69	67	65	70
<b>MOL response</b>								
OND mean [ $O_2$ ] <sub>(100)</sub>	-7.1	-8.0	-6.7	-6.5	-7.5	-8.9	-5.9	-6.6
OND max. [ $O_2$ ] <sub>(100)</sub>	-8.1	-9.2	-9.1	-7.6	-8.5	-9.9	-7.8	-7.8
Duration days/year	188	218	271	168	185	224	236	169
<b>(-1)*AOU<sub>(100)</sub> response</b>								
OND mean	-5.9	-5.9	-2.8	-6.1	-6.2	-6.8	-1.8	-6.0
OND max.	-9.9	-9.7	-7.4	-9.7	-9.5	-10.1	-5.2	-9.3
<b><math>O_{2sat}</math> response</b>								
JAS mean	-16.0	-17.0	-16.8	-15.4	-18.7	-20.4	-20.1	-17.7
JAS max.	-18.6	-20.3	-19.4	-17.7	-21.9	-24.0	-24.1	-20.6

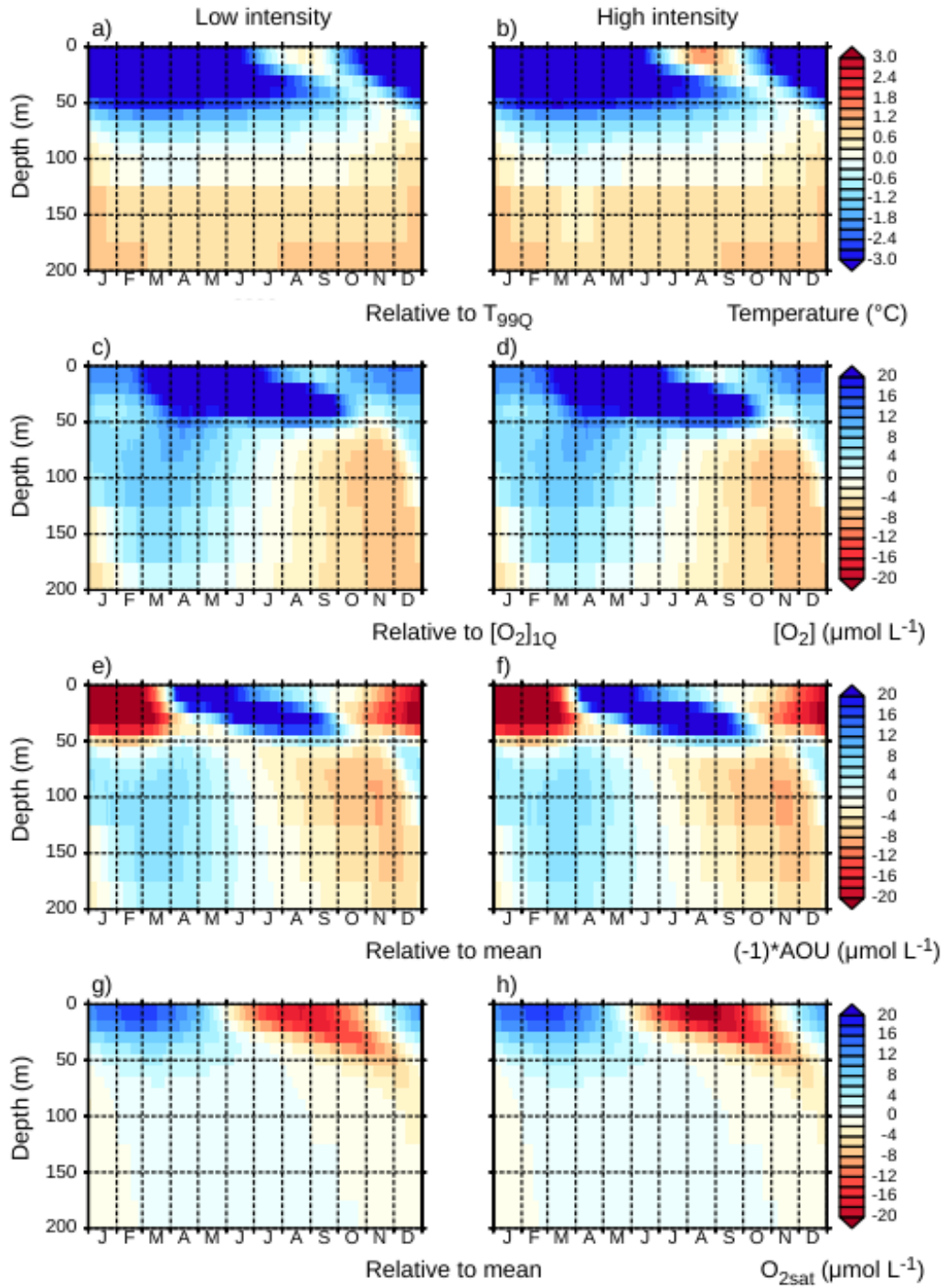


Figure 21: time-mean seasonal cycles (0-200 m) for composite Low Intensity ( $SST_{max} < SST_{99Q} + 1.5^{\circ}C$ ; a, c, e and g) and High Intensity ( $SST_{max} \geq SST_{99Q} + 1.5^{\circ}C$ ; b, d, f and h) MHW years for RCP4.5 (2076-2099) for the MS in temperature ( $^{\circ}C$ ; a and b),  $[O_2]$  ( $\mu mol\ l^{-1}$ ; c and d),  $(-1)*AOU$  ( $\mu mol\ l^{-1}$ ; e and f) and  $O_{2sat}$  ( $\mu mol\ l^{-1}$ ; g and h). For temperature and  $[O_2]$ ,  $T_{99P}$  and  $[O_2]_{1P}$  thresholds are represented by zero so that yellow through red shading indicates extremes;  $(-1)*AOU$  and  $O_{2sat}$  are relative to the 2076-2099 mean.

*Figures 21a and b* display climatological temperature for composite Low Intensity (*a*) and High Intensity (*b*) MHW years at the end of the century under RCP4.5. The most notable difference occurs in the surface from July – September during the MHW event. High Intensity event temperatures are elevated in the upper 20 metres and show greater downwards propagation in September relative to Low Intensity events. High Intensity (Low Intensity) events have mean and maximum intensities of 1.0°C (0.4°C) and 1.5°C (0.5°C), and last on average 72 (27) days (*Table 3*). High Intensity MHW characteristics exceed in severity those of Low Intensity MHWs in every subbasin (*Table 3*). There is only a small difference in subsurface (50-200 metres) temperature following High and Low Intensity MHW events (*Figures 21a and b*).

*Figures 21c and d* show MOL characteristics in response to High and Low Intensity MHWs, with peak intensities ( $[O_2] < [O_2]_{1P}$  by 6-8  $\mu\text{mol L}^{-1}$ ) between October to December evident in the water column (50-200 metres depth). There is little to distinguish between MOLs in *Figures 21c and d* but statistics in *Table 3* show quantitative differences. Subsequent to composite High Intensity (Low Intensity) MHWs, autumn MOL mean and maximum intensity responses reach 7.6 (7.2) and 8.6 (8.3)  $\mu\text{mol L}^{-1}$  below  $[O_2]_{(100)1P}$  for the MS. High Intensity MHWs are generally associated with more seasonal oxygen depletion at 100 metres depth when compared with Low Intensity events. NW experiences the lowest mean (maximum) intensity MOL response to High Intensity MHWs with  $[O_2]_{(100)}$  reaching 8.9 (9.9)  $\mu\text{mol L}^{-1}$  below  $[O_2]_{(100)1P}$ . MOLs last on average 6 days longer at 100 metres depth following High Intensity MHWs relative to Low Intensity MHWs in NW (*Table 3*). Because the strongest deoxygenation signal is found in NW following High Intensity MHWs, statistics from *Table 3* support findings from *Figures 16, 17 and 18* that this region

has a greater sensitivity to climate change relative to the rest of the MS (*see section 4.1 and 4.2.1*).

*Figures 21e and f* demonstrate a similar response in both AOU and  $O_{2\text{sat}}$  responses following High and Low Intensity MHWs. In both instances, the autumn maximum for AOU is 8-10  $\mu\text{mol L}^{-1}$  below the end-of-the-century mean and is strongest between 80-125 metres depth; however, this persists for longer ( $\sim 25$  days; *Figure 21f*) following High Intensity MHWs relative to Low Intensity ( $< 10$  days; *Figure 21e*). The response of  $(-1) \cdot \text{AOU}_{(100)}$  tracks that of  $[\text{O}_2]_{(100)}$  across the entire MS and within individual subbasins. For example, both mean and maximum  $[\text{O}_2]_{(100)}$  and  $(-1) \cdot \text{AOU}_{(100)}$  are lowest in NW under High Intensity MHW events (*Table 3*). *Figures 21g and h* show that the prominent difference between  $O_{2\text{sat}}$  responses occurs at the surface supporting findings from *Figure 20* (*section 4.2.3*) that the AOU signal drives MOL events. The notable difference in  $O_{2\text{sat}}$  response to High and Low Intensity MHWs occurs at the surface (0-20 metres) in July–September: warmer temperatures during High Intensity MHWs means  $[\text{O}_2]$  is less soluble driving a stronger negative  $O_{2\text{sat}}$  response.

### 4.3.2 Category comparison

Table 4: Summary of the mean Low Category ( $SST_{max} < \text{category } 2$ ) and High Category ( $SST_{max} \geq \text{category } 2$ ) MHWs across 2076-2099 and their corresponding MOL, AOU and  $O_{2sat}$  responses. Calculations follow the same methodology as for the values in Table 3 except data is grouped based on annual maximum MHW Category as opposed to Intensity.

		RCP4.5 (2076-2099)							
		Whole	NW	AD	SE	Whole	NW	AD	SE
<b>MHW characteristics</b>		Low category ( $SST_{max} < \text{category } 2$ )				High category ( $SST_{max} \geq \text{category } 2$ )			
	Mean MHW SST	0.2	0.2	0.1	0.2	1.2	1.3	1.1	1.2
	Max. MHW SST	0.3	0.4	0.1	0.3	2.1	2.1	2.0	2.0
	Event duration (days/year)	27	19	4	31	72	72	68	73
<b>MOL response</b>									
	OND mean $[O_2]_{(100)}$	-7.2	-8.3	-7.2	-6.5	-7.6	-8.8	-5.9	-6.8
	OND max. $[O_2]_{(100)}$	-8.3	-9.4	-9.9	-7.6	-8.6	-9.9	-7.8	-7.9
	Duration (days/year)	188	215	278	170	183	224	237	158
<b>(-1)*AOU<sub>100</sub> response</b>									
	OND mean	-6.1	-6.2	-3.3	-6.1	-6.2	-6.8	-1.8	-6.0
	OND max.	-8.1	-8.0	-7.0	-8.3	-8.2	-8.6	-4.7	-8.1
<b><math>O_{2sat}</math> response</b>									
	JAS mean	-15.9	-16.8	-16.1	-15.4	-18.6	-20.3	-19.9	-17.6
	JAS max.	-18.7	-20.3	-18.7	-17.7	-21.8	-23.7	-23.8	-20.6

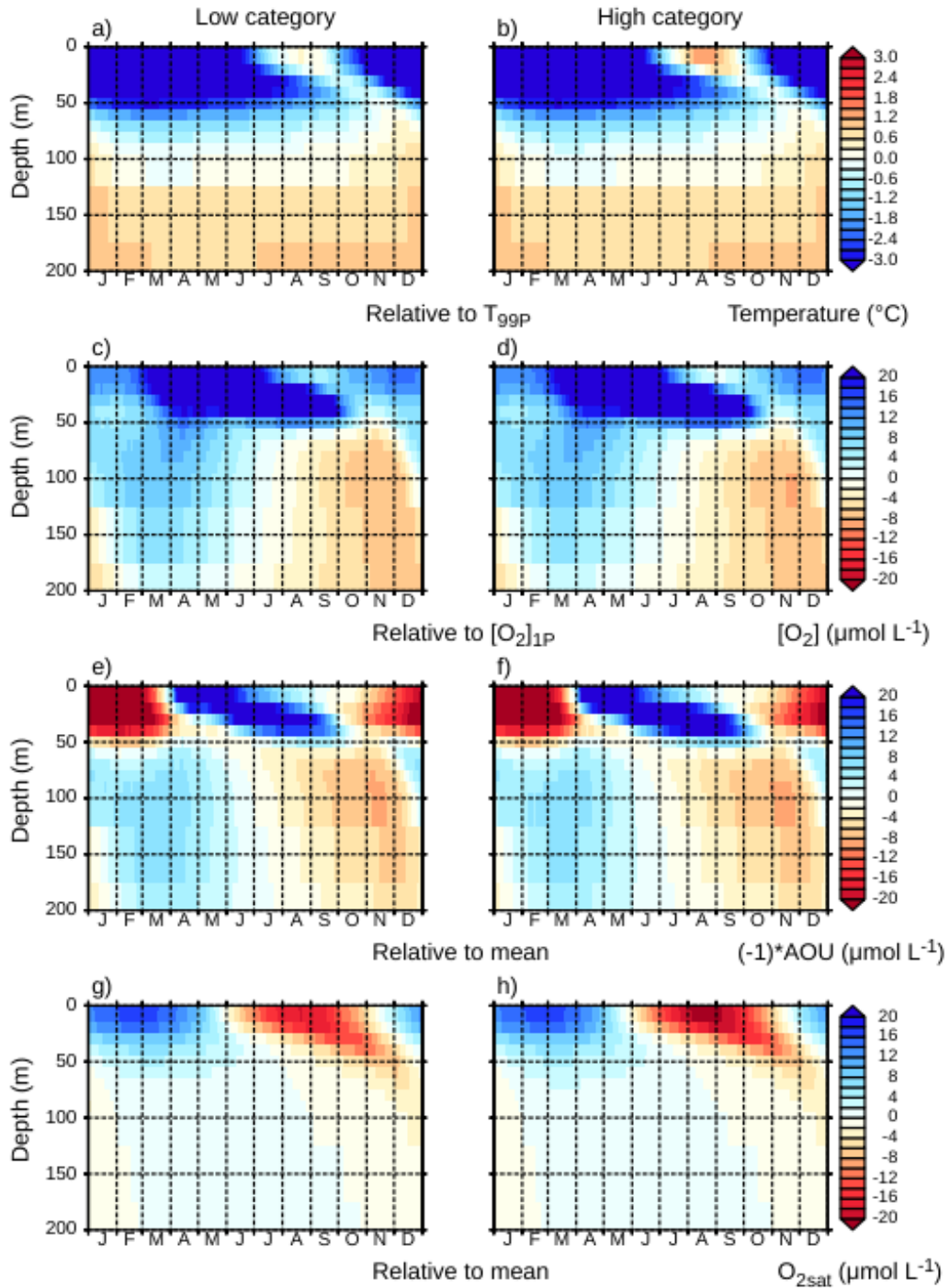


Figure 22: time-mean seasonal cycles (0-200 m) for composite Low Category (Category < 2; a, c, e and g) and High Category (Category ≥ 2; b, d, f and h) MHW years under RCP4.5 (2076-2099) for the MS in temperature (°C; a and b), [O<sub>2</sub>] (μmol l<sup>-1</sup>; c and d), (-1)\*AOU (μmol l<sup>-1</sup>; e and f) and O<sub>2sat</sub> (μmol l<sup>-1</sup>; g and h). For temperature and [O<sub>2</sub>], T<sub>99P</sub> and [O<sub>2</sub>]<sub>1P</sub> thresholds are represented by zero so that yellow through red shading indicates extremes; (-1)\*AOU and O<sub>2sat</sub> are relative to the 2076-2099 mean.



*Figures 22a and b* show climatological temperature across 0-200 metres depth for composite Low Category (*a*) and High Category (*b*) MHW years at the end of the century under RCP4.5. Similar to High and Low Intensity MHWs (*Figures 21a and b*), composite High Category (Low Category) events occur from July – September (August – September; *Figures 22a and b*) lasting for 72 (27; *Table 4*) days with greater propagation of extremes to 30 metres depth relative to Low Category MHWs (*Figures 22a and b*). MHW categorisation appears to have only a negligible effect on subsurface (50-200 meters) warming. Mean and maximum SST exceeds  $SST_{99P}$  by 1.2°C (0.2°C) and 2.1°C (0.3°C; *Table 4*).

Because an annual MOL event is the norm in the MS by the end of the century (*see figure 20g*), both composite Low and High Category MHWs are followed by subsurface MOL events. MOL responses occur from July – January affecting 50-200 metres depth, peaking in intensity below  $[O_2]_{1P}$  from October – December by  $\sim 8 \mu\text{mol L}^{-1}$  (*Figures 22c and d*). Composite autumn mean and maximum intensity MOL responses to High Category (Low Category) MHWs are 8.3 (7.2)  $\mu\text{mol L}^{-1}$  and 8.6 (7.6)  $\mu\text{mol L}^{-1}$  lower than  $[O_2]_{(100)1P}$  (*Table 4*). High Category MHWs appear more connected to seasonal oxygen depletion at 100 metres depth relative to Low Intensity MHW events. In *Figures 22a and c*, Low Category MHWs begin in August yet the MOL events develop in July. This suggests that the water column stratifies prior to the onset of the MHW, supported by the (-1)\*AOU signal in *Figure 22e*. Because of this disparity in timings under Low Category MHWs, it may be useful to repeat this test using seasonally varying thresholds such as  $SST_{90P}$  (Hobday et al., 2016). Further, considering absolute differences between depth levels in density to accurately calculate stratification may better elucidate the relationship between SST and deoxygenation.

*Figures 22e and f* display the  $(-1)*\text{AOU}$  signal corresponding with the MOL response to Low and High Category MHWs. The differences in AOU responses are supported by statistics in *Table 3* where  $(-1)*\text{AOU}_{(100)}$  tracks  $[\text{O}_2]_{(100)}$  for the entire MS and individual subbasins. NW shows the largest composite High Category MHW response in terms of MOL  $[\text{O}_2]$  and AOU impacts relative to Low Category MHWs. *Figures 22g and h* display  $\text{O}_{2\text{sat}}$  response and demonstrate correspondence with SST between High and Low Category MHWs: warmer temperatures reduce  $\text{O}_{2\text{sat}}$ .

#### 4.4 Implications and recommendations

My work implies there will be physical and biogeochemical changes to the MS towards the end of the century in terms of increasing temperature and deoxygenation. My analysis suggests that the MS will experience larger, longer lasting and more intense MHWs by the end of the century under RCPs, providing support for other model evidence that MS MHWs will get progressively more severe towards 2100 (e.g. Darmaraki et al., 2019b). My work also highlights a gap in knowledge of ocean biogeochemistry in that discrete and prolonged periods of anomalously low  $[\text{O}_2]$  may occur during autumn in the MS in the subsurface (80-200 metres depth). MOL events are newly defined here and POLCOMS-ERSEM simulates that they may already impact the MS and that events will become longer, more expansive and greater in intensity by the end of the century. My analysis shows that MHWs of greater intensity or category have a greater impact on deoxygenation within the MS at the end of the century under RCP4.5. The MS is viewed as a laboratory basin for physical and biogeochemical parameters in the global ocean as findings made within this region can be applied the global ocean (e.g. Bergamasco and Malanotte-Rizzoli, 2010; Robinson and Golnaraghi, 1994). Therefore, it seems likely that MOL events will be found elsewhere. Further work could look to determine whether MOL

events occur in other shelf seas and the open ocean and provide support for my finding that they are exacerbated by greater MHW intensity.

The MS is a climate change hotspot and SSTs are increasing a rate 20% faster than the global mean (Giorgi, 2006; Lionello and Scarascia, 2018). At regional scales, my work demonstrates that within this hotspot exists a region that displays greater sensitivity to climate change: POLCOMS-ERSEM model projections suggest that greater increases (decreases) in NW mean temperature ( $[O_2]$ ) occur with time relative to the rest of the MS. Furthermore, this trend is mirrored in changes to extremes. My work shows  $SST_{99p}$  ( $[O_2]_{(100)1P}$ ) increasing (decreasing)  $0.005^{\circ}C\ year^{-1}$  ( $0.02\ \mu mol\ L^{-2}\ year^{-1}$ ) faster than the change in mean (*Figure 14c and f*) in NW under RCP4.5, resulting in a simulated east-west divide in terms of climate change impacts. The greater sensitivity to climate change in NW could be explained by future projections of mixed layer shoaling which is projected to be enhanced in this region relative to SE (Adloff et al., 2015). A strong positive air-sea heat flux can drive stratification and could be impacting MOL severity in my analysis. Other climate change hotspots such as the Tasman Sea have demonstrated a susceptibility to mixed layer shoaling during MHW events (Perkins-Kirkpatrick et al., 2019). My work suggests that biogeochemically important regions such as the Tasman Sea could also demonstrate a similar sensitivity to deoxygenation.

It could be argued that to assume that biogeochemical parameters directly underlying MHWs as I do in *Section 4.3* is simplistic, especially considering the complicated spatial relationship between MHW and MOL characteristics displayed in *Figures 17 and 18*. The validity of my methodology relies on the widespread nature of MHW events at the end of the century in order to determine different  $[O_2]$  responses to High and Low Intensity (Category) MHWs. A possible remedy could be to implement extreme event wave (EEW)

methodology which allows extreme events to be connected in space and time by linking together peaks above a threshold (Di Biagio et al., 2020). While Di Biagio et al. (2020) look at extremes at the surface, the method could be applied to link MHW and MOLs by averaging latitudinally or longitudinally allowing inclusion of the z-axis.

The AJ is the most nutrient-rich region of the MS and typically exhibits lower [O<sub>2</sub>] values due to source waters originating from the eastern boundary upwelling region of the North Atlantic. It provides the MS with 79% (56%) of reactive P (N) which drives primary production in the region (Powley et al., 2017). Mean net primary productivity in the AJ is simulated to increase by  $\sim 0.5 \text{ g C m}^{-2} \text{ day}^{-1}$  by 2050 in POLCOMS-ERSEM which then stabilises towards the end of the century under RCPs (Kay et al., 2018). The oligotrophic nature of the majority of the MS means that the AOU signal associated with MOLs is better explained by stratification of the water column as opposed to greater carbon export and remineralisation. However, the AJ may be an example within the MS where carbon export and remineralisation affects [O<sub>2</sub>] extremes. *Figures 18e-h* highlight that the AJ eutrophic region could have a greater sensitivity to deoxygenation compared with the rest of the basin. Physical-biogeochemical simulations of the global ocean show that MHWs cause stronger phytoplankton blooms in nutrient-rich waters due to warmer conditions and a greater availability of light; weaker blooms occur in oligotrophic waters resulting from mixed layer shoaling and higher nutrient stress (Hayashida et al., 2020). The relationship between MHW, nutrient levels and phytoplankton blooms has been explored in satellite-derived SST and surface chlorophyll concentration data throughout most of the Pacific, Atlantic and Indian oceans (Le Grix et al., 2021). A stronger phytoplankton bloom could increase carbon export and remineralisation in the subsurface MS where MOLs occur.

Future research could focus on whether eutrophic regions exhibit a strong relationship between MHWs, productivity and deoxygenation.

## 5 Conclusions

By using a high-resolution physical-biogeochemical model for 3-D temperature, [O<sub>2</sub>] and AOU, I have demonstrated the significant changes in marine extremes that the MS will undergo over the course of the 21<sup>st</sup> century. My work is the first to describe extreme events in [O<sub>2</sub>] by the application of MHW methodology and depth-dependent thresholds. My research provides further evidence that MHWs will become more severe under climate change and shows they impact biogeochemistry. While mean [O<sub>2</sub>] at the surface in the MS is controlled primarily by solubility effects, extremes in the subsurface are driven by the AOU signal. By the end of the century, MOLs occur annually and throughout the year peaking in intensity between October and December under RCP4.5 and RCP8.5. MOLs are likely driven predominantly by stratification and associated reductions in ventilation, but changes to springtime organic matter export in nutrient-rich regions may influence subsurface [O<sub>2</sub>] and contribute to extremes. The extent of mean deoxygenation by the end of the century results in historical extremes becoming the new norm by 2076-2099. By demonstrating that the northwest region of the MS is more sensitive to climate change compared to the rest of the basin in terms of temperature and dissolved oxygen, this work has implications for climate change hotspots in this region and globally. I recommend that further study could explore whether MOL events can be found in the global ocean or in other model simulations, and that considerations could be made by researchers for the potential ecosystem impacts of MOLs.

## 6 References

- Adloff, F., Somot, S., Sevault, F., Jordà, G., Aznar, R., Déqué, M., Herrmann, M., Marcos, M., Dubois, C., Padorno, E., Alvarez-Fanjul, E., Gomis, D., 2015. Mediterranean Sea response to climate change in an ensemble of twenty first century scenarios. *Clim Dyn* 45, 2775–2802. <https://doi.org/10.1007/s00382-015-2507-3>
- Allen, J.I., Somerfield, P.J., Gilbert, F.J., 2007. Quantifying uncertainty in high-resolution coupled hydrodynamic-ecosystem models. *Journal of Marine Systems* 12.
- Andrews, O., Buitenhuis, E., Le Quéré, C., Suntharalingam, P., 2017. Biogeochemical modelling of dissolved oxygen in a changing ocean. *Phil. Trans. R. Soc. A* 375, 20160328. <https://doi.org/10.1098/rsta.2016.0328>
- Andrews, O.D., Bindoff, N.L., Halloran, P.R., Ilyina, T., Le Quéré, C., 2013. Detecting an external influence on recent changes in oceanic oxygen using an optimal fingerprinting method. *Biogeosciences* 10, 1799–1813. <https://doi.org/10.5194/bg-10-1799-2013>
- Artioli, Y., Blackford, J.C., Butenschön, M., Holt, J.T., Wakelin, S.L., Thomas, H., Borges, A.V., Allen, J.I., 2012. The carbonate system in the North Sea: Sensitivity and model validation. *Journal of Marine Systems* 102–104, 1–13. <https://doi.org/10.1016/j.jmarsys.2012.04.006>
- Bange, H.W., 2006. Nitrous oxide and methane in European coastal waters 14.
- Baretta, J.W., Ebenhöf, W., Ruardij, P., 1995. The European regional seas ecosystem model, a complex marine ecosystem model. *Netherlands Journal of Sea Research* 33, 233–246. [https://doi.org/10.1016/0077-7579\(95\)90047-0](https://doi.org/10.1016/0077-7579(95)90047-0)
- Benthuyssen, J.A., Oliver, E.C.J., Feng, M., Marshall, A.G., 2018. Extreme Marine Warming Across Tropical Australia During Austral Summer 2015-2016. *J. Geophys. Res. Oceans* 123, 1301–1326. <https://doi.org/10.1002/2017JC013326>
- Bergamasco, A., Malanotte-Rizzoli, P., 2010. The circulation of the Mediterranean Sea: a historical review of experimental investigations. *Advances in Oceanography and Limnology* 1, 11–28. <https://doi.org/10.1080/19475721.2010.491656>
- Bernardello, R., Cardoso, J.G., Bahamon, N., Donis, D., Marinov, I., Cruzado, A., 2012. Factors controlling interannual variability of vertical organic matter export and phytoplankton bloom dynamics – a numerical case-study for the NW Mediterranean Sea 13.
- Bianchi, D., Dunne, J.P., Sarmiento, J.L., Galbraith, E.D., 2012. Data-based estimates of suboxia, denitrification, and N<sub>2</sub>O production in the ocean and their sensitivities to dissolved O<sub>2</sub>: DATA-BASED SUBOXIA AND DENITRIFICATION. *Global Biogeochem. Cycles* 26, n/a-n/a. <https://doi.org/10.1029/2011GB004209>
- Bindoff, N.L., Cheung, W.W.L., Kairo, J.G., Arístegui, J., Guinder, V.A., Hallberg, R., Hilmi, N., Jiao, N., O’Donoghue, S., Suga, T., Acar, S., Alava, J.J., Allison, E., Arbic, B., Bambridge, T., Boyd, P.W., Bruggeman, J., Butenschön, M., Chávez, F.P., Cheng, L., Cinar, M., Costa, D., Defeo, O., Djoundourian, S., Domingues, C., Eddy, T., Endres, S., Fox, A., Free, C., Frölicher, T., Gattuso, J.-P., Gerber, G., Hallegraef, G., Harrison, M., Hennige, S., Hindell, M., Hogg, A., Ito, T., Kenny, T.-A., Kroeker, K., Kwiatkowski, L., Lam, V.W.Y., Laüfkotter, C., LeBillon, P., Bris, N.L., Lotze, H., MacKinnon, J., de Marffy-Mantuano, A., Martel, P., Molinos, J.G., Moseman-Valtierra, S., Motau, A., Mulsow, S., Mutombo, K., Oyinlola, M., Poloczanska, E.S., Pascal, N., Philip, M., Purkey, S., Rathore, S., Rebelo, X., Reygondeau, G., Rice, J., Richardson, A., Riebesell, U., Roach, C., Rocklöv, J., Roberts, M., Sloyan, B., Smith, M., Shurety, A., Wabnitz, C., Whalen, C.,

- in press. Changing Ocean, Marine Ecosystems, and Dependent Communities. *Marine Ecosystems* 142.
- Bohlen, L., Dale, A.W., Wallmann, K., 2012. Simple transfer functions for calculating benthic fixed nitrogen losses and C:N:P regeneration ratios in global biogeochemical models. *Global Biogeochem. Cycles* 26, 2011GB004198. <https://doi.org/10.1029/2011GB004198>
- Bond, N.A., Cronin, M.F., Freeland, H., Mantua, N., 2015. Causes and impacts of the 2014 warm anomaly in the NE Pacific: 2014 WARM ANOMALY IN THE NE PACIFIC. *Geophys. Res. Lett.* 42, 3414–3420. <https://doi.org/10.1002/2015GL063306>
- Bopp, L., Resplandy, L., Orr, J.C., Doney, S.C., Dunne, J.P., Gehlen, M., Halloran, P., Heinze, C., Ilyina, T., Séférian, R., Tjiputra, J., Vichi, M., 2013. Multiple stressors of ocean ecosystems in the 21st century: projections with CMIP5 models. *Biogeosciences* 10, 6225–6245. <https://doi.org/10.5194/bg-10-6225-2013>
- Borghini, M., Bryden, H., Schroeder, K., Sparnocchia, S., Vetrano, A., 2014. The Mediterranean is becoming saltier. *Ocean Sci.* 10, 693–700. <https://doi.org/10.5194/os-10-693-2014>
- Boyer, T.P., Antonov, J.I., Baranova, O.K., Coleman, C., Garcia, H.E., Grodsky, A., Johnson, D.R., Locarnini, R.A., Mishonov, A.V., O'Brien, T.D., Paver, C.R., Reagan, J.R., Seidov, D., Smolyar, I.V., Zweng, M.M., 2013. NOAA Atlas NESDIS 72: World Ocean Database 2013 208.
- Brauко, K.M., 2020. Marine Heatwaves, Sewage and Eutrophication Combine to Trigger Deoxygenation and Biodiversity Loss: A SW Atlantic Case Study. *Frontiers in Marine Science* 7, 12.
- Butenschön, M., Clark, J., Aldridge, J.N., Allen, J.I., Artioli, Y., Blackford, J., Bruggeman, J., Cazenave, P., Ciavatta, S., Kay, S., Lessin, G., van Leeuwen, S., van der Molen, J., de Mora, L., Polimene, L., Saille, S., Stephens, N., Torres, R., 2016. ERSEM 15.06: a generic model for marine biogeochemistry and the ecosystem dynamics of the lower trophic levels. *Geosci. Model Dev.* 9, 1293–1339. <https://doi.org/10.5194/gmd-9-1293-2016>
- Capotondi, A., Alexander, M.A., Bond, N.A., Curchitser, E.N., Scott, J.D., 2012. Enhanced upper ocean stratification with climate change in the CMIP3 models: CLIMATE CHANGE OF OCEAN STRATIFICATION. *J. Geophys. Res.* 117, n/a-n/a. <https://doi.org/10.1029/2011JC007409>
- Caputi, N., Kangas, M., Chandrapavan, A., Hart, A., Feng, M., Marin, M., Lestang, S. de, 2019. Factors Affecting the Recovery of Invertebrate Stocks From the 2011 Western Australian Extreme Marine Heatwave. *Front. Mar. Sci.* 6, 484. <https://doi.org/10.3389/fmars.2019.00484>
- Cerrano, C., Bavestrello, G., Bianchi, C.N., Cattaneo-vietti, R., Bava, S., Morganti, C., Morri, C., Picco, P., Sara, G., Schiaparelli, S., Siccardi, A., Sponga, F., 2000. A catastrophic mass-mortality episode of gorgonians and other organisms in the Ligurian Sea (North-western Mediterranean), summer 1999. *Ecol Letters* 3, 284–293. <https://doi.org/10.1046/j.1461-0248.2000.00152.x>
- Chan, F., Barth, J.A., Lubchenco, J., Kirincich, A., Weeks, H., Peterson, W.T., Menge, B.A., 2008. Emergence of Anoxia in the California Current Large Marine Ecosystem. *Science* 319, 920–920. <https://doi.org/10.1126/science.1149016>
- Chen, K., Gawarkiewicz, G.G., Lentz, S.J., Bane, J.M., 2014. Diagnosing the warming of the Northeastern U.S. Coastal Ocean in 2012: A linkage between the atmospheric jet stream variability and ocean response: DIAGNOSING THE COASTAL WARMING IN



2012. *J. Geophys. Res. Oceans* 119, 218–227. <https://doi.org/10.1002/2013JC009393>
- Cheng, L., Abraham, J., Hausfather, Z., Trenberth, K.E., 2019. How fast are the oceans warming? *Science* 363, 128–129. <https://doi.org/10.1126/science.aav7619>
- Cocito, S., Sgorbini, S., 2014. Long-term trend in substratum occupation by a clonal, carbonate bryozoan in a temperate rocky reef in times of thermal anomalies. *Mar Biol* 161, 17–27. <https://doi.org/10.1007/s00227-013-2310-9>
- Collins, M., Sutherland, M., Bouwer, L., Cheong, S.-M., Combes, H.J.D., Roxy, M.K., Losada, I., McInnes, K., Ratter, B., Rivera-Arriaga, E., Susanto, R.D., Swingedouw, D., Tibig, L., Bakker, P., Eakin, C.M., Emanuel, K., Grose, M., Hemer, M., Jackson, L., Kääh, A., Kajtar, J., Knutson, T., Laufkötter, C., Noy, I., Payne, M., Ranasinghe, R., Sgubin, G., Timmermans, M.-L., Abdulla, A., González, M.H., Turley, C., n.d. SPM6 Extremes, Abrupt Changes and Managing Risks 68. <https://doi.org/In press>.
- Coma, R., Ribes, M., Serrano, E., Jiménez, E., Salat, J., Pascual, J., 2009. Global warming-enhanced stratification and mass mortality events in the Mediterranean. *PNAS* 106, 6176–6181. <https://doi.org/10.1073/pnas.0805801106>
- Coppola, L., Legendre, L., Lefevre, D., Prieur, L., Taillandier, V., Diamond Riquier, E., 2018. Seasonal and inter-annual variations of dissolved oxygen in the northwestern Mediterranean Sea (DYFAMED site). *Progress in Oceanography* 162, 187–201. <https://doi.org/10.1016/j.pocean.2018.03.001>
- Darmaraki, S., Somot, S., Sevault, F., Nabat, P., 2019a. Past Variability of Mediterranean Sea Marine Heatwaves. *Geophys. Res. Lett.* 46, 9813–9823. <https://doi.org/10.1029/2019GL082933>
- Darmaraki, S., Somot, S., Sevault, F., Nabat, P., Cabos Narvaez, W.D., Cavicchia, L., Djurdjevic, V., Li, L., Sannino, G., Sein, D.V., 2019b. Future evolution of Marine Heatwaves in the Mediterranean Sea. *Clim Dyn* 53, 1371–1392. <https://doi.org/10.1007/s00382-019-04661-z>
- Di Biagio, V., Cossarini, G., Salon, S., Solidoro, C., 2020. Characterisation of extreme events waves in marine ecosystems: the case of Mediterranean Sea (preprint). *Biogeochemistry: Modelling, Aquatic*. <https://doi.org/10.5194/bg-2020-34>
- Di Lorenzo, E., Mantua, N., 2016. Multi-year persistence of the 2014/15 North Pacific marine heatwave. *Nature Clim Change* 6, 1042–1047. <https://doi.org/10.1038/nclimate3082>
- Diaz, R.J., Rosenberg, R., 2008. Spreading Dead Zones and Consequences for Marine Ecosystems. *Science* 321, 926–929. <https://doi.org/10.1126/science.1156401>
- Duteil, O., Oschlies, A., Böning, C.W., 2018. Pacific Decadal Oscillation and recent oxygen decline in the eastern tropical Pacific Ocean. *Biogeosciences* 15, 7111–7126. <https://doi.org/10.5194/bg-15-7111-2018>
- El-Gezir, T.M., Bryden, I.G., 2014. The circulation pattern in the Mediterranean Sea: issues for modeller consideration. *Journal of Operational Oceanography* 3, 9. <https://doi.org/10.1080/1755876X.2010.11020116>
- Estrada, M., Marrasé, C., Latasa, M., Berdalet, E., Delgado, M., Riera, T., 1993. Variability of deep chlorophyll maximum characteristics in the Northwestern Mediterranean. *Mar. Ecol. Prog. Ser.* 92, 289–300. <https://doi.org/10.3354/meps092289>
- Feudale, L., Shukla, J., 2007. Role of Mediterranean SST in enhancing the European heat wave of summer 2003. *Geophys. Res. Lett.* 34, L03811. <https://doi.org/10.1029/2006GL027991>
- Frölicher, T.L., Fischer, E.M., Gruber, N., 2018. Marine heatwaves under global warming. *Nature* 560, 360–364. <https://doi.org/10.1038/s41586-018-0383-9>

- Frolicher, T.L., Joos, F., Plattner, G.-K., Steinacher, M., Doney, S.C., 2009. Natural variability and anthropogenic trends in oceanic oxygen in a coupled carbon cycle–climate model ensemble 15.
- Gačić, M., Civitarese, G., Eusebi Borzelli, G.L., Kovačević, V., Poulain, P.-M., Theocharis, A., Menna, M., Catucci, A., Zarokanellos, N., 2011. On the relationship between the decadal oscillations of the northern Ionian Sea and the salinity distributions in the eastern Mediterranean. *J. Geophys. Res.* 116, C12002. <https://doi.org/10.1029/2011JC007280>
- Galli, G., Solidoro, C., Lovato, T., 2017. Marine Heat Waves Hazard 3D Maps and the Risk for Low Motility Organisms in a Warming Mediterranean Sea. *Front. Mar. Sci.* 4, 136. <https://doi.org/10.3389/fmars.2017.00136>
- Gao, G., Marin, M., Feng, M., Yin, B., Yang, D., Feng, X., Ding, Y., Song, D., 2020. Drivers of Marine Heatwaves in the East China Sea and the South Yellow Sea in Three Consecutive Summers During 2016–2018. *J. Geophys. Res. Oceans* 125. <https://doi.org/10.1029/2020JC016518>
- García-Herrera, R., Díaz, J., Trigo, R.M., Luterbacher, J., Fischer, E.M., 2010. A Review of the European Summer Heat Wave of 2003. *Critical Reviews in Environmental Science and Technology* 40, 267–306. <https://doi.org/10.1080/10643380802238137>
- Garrabou, J., Coma, R., Bensoussan, N., Bally, M., Chevaldonné, P., Cigliano, M., Diaz, D., Harmelin, J.G., Gambi, M.C., Kersting, D.K., Ledoux, J.B., Lejeusne, C., Linares, C., Marschal, C., Pérez, T., Ribes, M., Romano, J.C., Serrano, E., Teixido, N., Torrents, O., Zabala, M., Zuberer, F., Cerrano, C., 2009. Mass mortality in Northwestern Mediterranean rocky benthic communities: effects of the 2003 heat wave. *Global Change Biology* 15, 1090–1103. <https://doi.org/10.1111/j.1365-2486.2008.01823.x>
- Garrabou, J., Perez, T., Sartoretto, S., Harmelin, J., 2001. Mass mortality event in red coral *Corallium rubrum* populations in the Provence region (France, NW Mediterranean). *Mar. Ecol. Prog. Ser.* 217, 263–272. <https://doi.org/10.3354/meps217263>
- Gentemann, C.L., Minnett, P.J., Le Borgne, P., Merchant, C.J., 2008. Multi-satellite measurements of large diurnal warming events. *Geophys. Res. Lett.* 35, L22602. <https://doi.org/10.1029/2008GL035730>
- Gilly, W.F., Beman, J.M., Litvin, S.Y., Robison, B.H., 2013. Oceanographic and Biological Effects of Shoaling of the Oxygen Minimum Zone. *Annu. Rev. Mar. Sci.* 5, 393–420. <https://doi.org/10.1146/annurev-marine-120710-100849>
- Giomi, F., Barausse, A., Duarte, C.M., Booth, J., Agusti, S., Saderne, V., Anton, A., Daffonchio, D., Fusi, M., 2019. Oxygen supersaturation protects coastal marine fauna from ocean warming. *SCIENCE ADVANCES* 8.
- Giorgi, F., 2006. Climate change hot-spots. *Geophys. Res. Lett.* 33, L08707. <https://doi.org/10.1029/2006GL025734>
- Giorgi, F., Jones, C., Asrar, G.R., 2009. Addressing climate information needs at the regional level: the CORDEX framework 9.
- Gruber, N., 2011. Warming up, turning sour, losing breath: ocean biogeochemistry under global change. *Proc. R. Soc. A* 369, 1980–1996. <https://doi.org/10.1098/rsta.2011.0003>
- Hausfather, Z., Peters, G.P., 2020. Emissions – the ‘business as usual’ story is misleading. *Nature* 577, 618–620. <https://doi.org/10.1038/d41586-020-00177-3>

- Hayashida, H., Matear, R.J., Strutton, P.G., 2020. Background nutrient concentration determines phytoplankton bloom response to marine heatwaves. *Glob Change Biol* 26, 4800–4811. <https://doi.org/10.1111/gcb.15255>
- Hobbs, J.-P.A., McDonald, C.A., 2010. Increased seawater temperature and decreased dissolved oxygen triggers fish kill at the Cocos (Keeling) Islands, Indian Ocean. *Journal of Fish Biology* 77, 1219–1229. <https://doi.org/10.1111/j.1095-8649.2010.02726.x>
- Hobday, A., Oliver, E., Sen Gupta, A., Benthuyesen, J., Burrows, M., Donat, M., Holbrook, N., Moore, P., Thomsen, M., Wernberg, T., Smale, D., 2018. Categorizing and Naming Marine Heatwaves. *Oceanog* 31. <https://doi.org/10.5670/oceanog.2018.205>
- Hobday, A.J., Alexander, L.V., Perkins, S.E., Smale, D.A., Straub, S.C., Oliver, E.C.J., Benthuyesen, J.A., Burrows, M.T., Donat, M.G., Feng, M., Holbrook, N.J., Moore, P.J., Scannell, H.A., Sen Gupta, A., Wernberg, T., 2016. A hierarchical approach to defining marine heatwaves. *Progress in Oceanography* 141, 227–238. <https://doi.org/10.1016/j.pocean.2015.12.014>
- Holbrook, N.J., Scannell, H.A., Sen Gupta, A., Benthuyesen, J.A., Feng, M., Oliver, E.C.J., Alexander, L.V., Burrows, M.T., Donat, M.G., Hobday, A.J., Moore, P.J., Perkins-Kirkpatrick, S.E., Smale, D.A., Straub, S.C., Wernberg, T., 2019. A global assessment of marine heatwaves and their drivers. *Nat Commun* 10, 2624. <https://doi.org/10.1038/s41467-019-10206-z>
- Holt, J., Harle, J., Proctor, R., Michel, S., Ashworth, M., Batstone, C., Allen, I., Holmes, R., Smyth, T., Haines, K., Bretherton, D., Smith, G., 2009. Modelling the global coastal ocean. *Philosophical Transactions of the Royal Society A: Mathematical, Physical and Engineering Sciences* 367, 939–951. <https://doi.org/10.1098/rsta.2008.0210>
- Holt, J., Schrum, C., Cannaby, H., Daewel, U., Allen, I., Artioli, Y., Bopp, L., Butenschon, M., Fach, B.A., Harle, J., Pushpadas, D., Salihoglu, B., Wakelin, S., 2016. Potential impacts of climate change on the primary production of regional seas: A comparative analysis of five European seas. *Progress in Oceanography* 140, 91–115. <https://doi.org/10.1016/j.pocean.2015.11.004>
- Holt, J.T., James, I.D., 2001. An  $\sigma_t$  coordinate density evolving model of the northwest European continental shelf: 1. Model description and density structure. *J. Geophys. Res.* 106, 14015–14034. <https://doi.org/10.1029/2000JC000304>
- Hughes, T.P., Kerry, J.T., Baird, A.H., Connolly, S.R., Dietzel, A., Eakin, C.M., Heron, S.F., Hoey, A.S., Hoogenboom, M.O., Liu, G., McWilliam, M.J., Pears, R.J., Pratchett, M.S., Skirving, W.J., Stella, J.S., Torda, G., 2018. Global warming transforms coral reef assemblages. *Nature* 556, 492–496. <https://doi.org/10.1038/s41586-018-0041-2>
- Jacox, M.G., Alexander, M.A., Bograd, S.J., Scott, J.D., 2020. Thermal displacement by marine heatwaves. *Nature* 584, 82–86. <https://doi.org/10.1038/s41586-020-2534-z>
- Jenkyns, H.C., 2010. Geochemistry of oceanic anoxic events: REVIEW. *Geochem. Geophys. Geosyst.* 11, n/a-n/a. <https://doi.org/10.1029/2009GC002788>
- Jones, T., Parrish, J.K., Peterson, W.T., Bjorkstedt, E.P., Bond, N.A., Ballance, L.T., Bowes, V., Hipfner, J.M., Burgess, H.K., Dolliver, J.E., Lindquist, K., Lindsey, J., Nevins, H.M., Robertson, R.R., Roletto, J., Wilson, L., Joyce, T., Harvey, J., 2018. Massive Mortality of a Planktivorous Seabird in Response to a Marine Heatwave. *Geophys. Res. Lett.* 45, 3193–3202. <https://doi.org/10.1002/2017GL076164>
- Kay, S., Andersson, H., Eilola, K., Wehde, H., Ramirez-Romero, E., Jordà, G., Catalan, I., 2018. CERES Deliverable D 1.3: Projections of physical and biogeochemical parameters

- and habitat indicators for European seas, including synthesis of Sea Level Rise and storminess.
- Kay, S., Butenschön, M., 2018. Projections of change in key ecosystem indicators for planning and management of marine protected areas: An example study for European seas. *Estuarine, Coastal and Shelf Science* 201, 172–184. <https://doi.org/10.1016/j.ecss.2016.03.003>
- Keeling, R.F., Körtzinger, A., Gruber, N., 2010a. Ocean Deoxygenation in a Warming World. *Annu. Rev. Mar. Sci.* 2, 199–229. <https://doi.org/10.1146/annurev.marine.010908.163855>
- Keeling, R.F., Körtzinger, A., Gruber, N., 2010b. Ocean Deoxygenation in a Warming World. *Annu. Rev. Mar. Sci.* 2, 199–229. <https://doi.org/10.1146/annurev.marine.010908.163855>
- Kimor, B., Berman, T., Schneller, A., 1987. Phytoplankton assemblages in the deep chlorophyll maximum layers off the Mediterranean coast of Israel. *Journal of Plankton Research* 9, 433–443.
- Kipson, S., Linares, C., Teixidó, N., Bakran-Petricioli, T., Garrabou, J., 2012. Effects of thermal stress on early developmental stages of a gorgonian coral. *Mar. Ecol. Prog. Ser.* 470, 69–78. <https://doi.org/10.3354/meps09982>
- Kountoura, K., Zacharias, I., 2014. Annual hypoxia dynamics in a semi-enclosed Mediterranean gulf. *Journal of Marine Systems* 139, 320–331. <https://doi.org/10.1016/j.jmarsys.2014.07.007>
- Kralj, M., Lipizer, M., Čermelj, B., Celio, M., Fabbro, C., Brunetti, F., Francé, J., Mozetič, P., Giani, M., 2019. Hypoxia and dissolved oxygen trends in the northeastern Adriatic Sea (Gulf of Trieste). *Deep Sea Research Part II: Topical Studies in Oceanography* 164, 74–88. <https://doi.org/10.1016/j.dsr2.2019.06.002>
- Kružić, P., Lipej, L., Mavrič, B., Rodić, P., 2014. Impact of bleaching on the coral *Cladocora caespitosa* in the eastern Adriatic Sea. *Mar. Ecol. Prog. Ser.* 509, 193–202. <https://doi.org/10.3354/meps10962>
- Kwiatkowski, L., Torres, O., Bopp, L., Aumont, O., Chamberlain, M., Christian, J., Dunne, J.P., Gehlen, M., Ilyina, T., John, J.G., Lenton, A., Li, H., Lovenduski, N.S., Orr, J.C., Palmieri, J., Schwinger, J., Séférian, R., Stock, C.A., Tagliabue, A., Takano, Y., Tjiputra, J., Toyama, K., Tsujino, H., Watanabe, M., Yamamoto, A., Yool, A., Ziehn, T., 2020. Twenty-first century ocean warming, acidification, deoxygenation, and upper ocean nutrient decline from CMIP6 model projections (preprint). *Earth System Science/Response to Global Change: Models, Holocene/Anthropocene*. <https://doi.org/10.5194/bg-2020-16>
- Laufkötter, C., Zscheischler, J., Frölicher, T.L., 2020. High-impact marine heatwaves attributable to human-induced global warming 6.
- Le Grix, N., Zscheischler, J., Laufkötter, C., Rousseaux, C.S., Frölicher, T.L., 2021. Compound high-temperature and low-chlorophyll extremes in the ocean over the satellite period. *Biogeosciences* 18, 2119–2137. <https://doi.org/10.5194/bg-18-2119-2021>
- Linares, C., Coma, R., Diaz, D., Zabala, M., Hereu, B., Dantart, L., 2005. Immediate and delayed effects of a mass mortality event on gorgonian population dynamics and benthic community structure in the NW Mediterranean Sea. *Mar. Ecol. Prog. Ser.* 305, 127–137. <https://doi.org/10.3354/meps305127>
- Lionello, P., Scarascia, L., 2018. The relation between climate change in the Mediterranean region and global warming. *Reg Environ Change* 18, 1481–1493. <https://doi.org/10.1007/s10113-018-1290-1>

- Liu, G., Heron, S., Eakin, C., Muller-Karger, F., Vega-Rodriguez, M., Guild, L., De La Cour, J., Geiger, E., Skirving, W., Burgess, T., Strong, A., Harris, A., Maturi, E., Ignatov, A., Sapper, J., Li, J., Lynds, S., 2014. Reef-Scale Thermal Stress Monitoring of Coral Ecosystems: New 5-km Global Products from NOAA Coral Reef Watch. *Remote Sensing* 6, 11579–11606. <https://doi.org/10.3390/rs61111579>
- Long, M.C., Deutsch, C., Ito, T., 2016. Finding forced trends in oceanic oxygen: TRENDS IN DISSOLVED OXYGEN. *Global Biogeochem. Cycles* 30, 381–397. <https://doi.org/10.1002/2015GB005310>
- Longhurst, A., Sathyendranath, S., Platt, T., Caverhill, C., 1995. An estimate of global primary production in the ocean from satellite radiometer data. *J Plankton Res* 17, 1245–1271. <https://doi.org/10.1093/plankt/17.6.1245>
- Macías, D., Stips, A., Garcia-Gorriz, E., 2014. The relevance of deep chlorophyll maximum in the open Mediterranean Sea evaluated through 3D hydrodynamic-biogeochemical coupled simulations. *Ecological Modelling* 281, 26–37. <https://doi.org/10.1016/j.ecolmodel.2014.03.002>
- Macias, D., Navarro, G., Echevarria, F., Garcia, C.M., Cueto, J.L., 2007. Phytoplankton pigment distribution in the northwestern Alboran Sea and meteorological forcing: A remote sensing study. *Journal of Marine Research* 22.
- Marbà, N., Duarte, C.M., 2010. Mediterranean warming triggers seagrass (*Posidonia oceanica*) shoot mortality: WARMING AND POSIDONIA OCEANICA SHOOT MORTALITY. *Global Change Biology* 16, 2366–2375. <https://doi.org/10.1111/j.1365-2486.2009.02130.x>
- Marty, J.-C., Chiavérini, J., Pizay, M.-D., Avril, B., 2002. Seasonal and interannual dynamics of nutrients and phytoplankton pigments in the western Mediterranean Sea at the DYFAMED time-series station (1991–1999). *Deep Sea Research Part II: Topical Studies in Oceanography* 49, 1965–1985. [https://doi.org/10.1016/S0967-0645\(02\)00022-X](https://doi.org/10.1016/S0967-0645(02)00022-X)
- Mavropoulou, A.-M., Vervatis, V., Sofianos, S., 2020. Dissolved oxygen variability in the Mediterranean Sea. *Journal of Marine Systems* 208, 103348. <https://doi.org/10.1016/j.jmarsys.2020.103348>
- Maynou, F., Sabatés, A., Ramirez-Romero, E., Catalán, I.A., Raya, V., 2020. Future distribution of early life stages of small pelagic fishes in the northwestern Mediterranean. *Climatic Change* 161, 567–589. <https://doi.org/10.1007/s10584-020-02723-4>
- McSweeney, C.F., Jones, R.G., Lee, R.W., Rowell, D.P., 2015. Selecting CMIP5 GCMs for downscaling over multiple regions. *Clim Dyn* 44, 3237–3260. <https://doi.org/10.1007/s00382-014-2418-8>
- Mena, C., Reglero, P., Hidalgo, M., Sintés, E., Santiago, R., Martín, M., Moyà, G., Balbín, R., 2019. Phytoplankton Community Structure Is Driven by Stratification in the Oligotrophic Mediterranean Sea. *Front. Microbiol.* 10, 1698. <https://doi.org/10.3389/fmicb.2019.01698>
- Merchant, C.J., Embury, O., Bulgin, C.E., Block, T., Corlett, G.K., Fiedler, E., Good, S.A., Mittaz, J., Rayner, N.A., Berry, D., Eastwood, S., Taylor, M., Tsushima, Y., Waterfall, A., Wilson, R., Donlon, C., 2019. Satellite-based time-series of sea-surface temperature since 1981 for climate applications. *Sci Data* 6, 223. <https://doi.org/10.1038/s41597-019-0236-x>
- Messmer, M., Gómez-Navarro, J.J., Raible, C.C., 2017. Sensitivity experiments on the response of Vb cyclones to sea surface temperature and soil moisture changes. *Earth Syst. Dynam.* 8, 477–493. <https://doi.org/10.5194/esd-8-477-2017>

- Moeller, H.V., Laufkötter, C., Sweeney, E.M., Johnson, M.D., 2019. Light-dependent grazing can drive formation and deepening of deep chlorophyll maxima. *Nat Commun* 10, 1978. <https://doi.org/10.1038/s41467-019-09591-2>
- Morley, J.W., Batt, R.D., Pinsky, M.L., 2017. Marine assemblages respond rapidly to winter climate variability. *Glob Change Biol* 23, 2590–2601. <https://doi.org/10.1111/gcb.13578>
- Nykjaer, L., 2009. Mediterranean Sea surface warming 1985–2006. *Clim. Res.* 39, 11–17. <https://doi.org/10.3354/cr00794>
- Olita, A., Sorgente, R., Natale, S., Gaberšek, S., Ribotti, A., Bonanno, A., Patti, B., 2007. Effects of the 2003 European heatwave on the Central Mediterranean Sea: surface fluxes and the dynamical response. *Ocean Sci.* 3, 273–289. <https://doi.org/10.5194/os-3-273-2007>
- Oliver, E.C.J., Benthuyesen, J.A., Bindoff, N.L., Hobday, A.J., Holbrook, N.J., Mundy, C.N., Perkins-Kirkpatrick, S.E., 2017. The unprecedented 2015/16 Tasman Sea marine heatwave. *Nat Commun* 8, 16101. <https://doi.org/10.1038/ncomms16101>
- Oliver, E.C.J., Benthuyesen, J.A., Darmaraki, S., Donat, M.G., Hobday, A.J., Holbrook, N.J., Schlegel, R.W., Sen Gupta, A., 2021. Marine Heatwaves. *Annu. Rev. Mar. Sci.* 13, 313–342. <https://doi.org/10.1146/annurev-marine-032720-095144>
- Oliver, E.C.J., Donat, M.G., Burrows, M.T., Moore, P.J., Smale, D.A., Alexander, L.V., Benthuyesen, J.A., Feng, M., Sen Gupta, A., Hobday, A.J., Holbrook, N.J., Perkins-Kirkpatrick, S.E., Scannell, H.A., Straub, S.C., Wernberg, T., 2018. Longer and more frequent marine heatwaves over the past century. *Nat Commun* 9, 1324. <https://doi.org/10.1038/s41467-018-03732-9>
- Oschlies, A., Brandt, P., Stramma, L., Schmidtko, S., 2018. Drivers and mechanisms of ocean deoxygenation. *Nature Geosci* 11, 467–473. <https://doi.org/10.1038/s41561-018-0152-2>
- Pagès, R., Baklouti, M., Barrier, N., Ayache, M., Sevault, F., Somot, S., Moutin, T., 2020. Projected Effects of Climate-Induced Changes in Hydrodynamics on the Biogeochemistry of the Mediterranean Sea Under the RCP 8.5 Regional Climate Scenario. *Front. Mar. Sci.* 7, 563615. <https://doi.org/10.3389/fmars.2020.563615>
- Pan, F., Guo, Z., Cai, Y., Liu, H., Wu, J., Fu, Y., Wang, B., Gao, A., 2019. Kinetic Exchange of Remobilized Phosphorus Related to Phosphorus-Iron-Sulfur Biogeochemical Coupling in Coastal Sediment. *Water Resour. Res.* 55, 10494–10517. <https://doi.org/10.1029/2019WR025941>
- Pastor, F., Valiente, J.A., Palau, J.L., 2018. Sea Surface Temperature in the Mediterranean: Trends and Spatial Patterns (1982–2016). *Pure Appl. Geophys.* 175, 4017–4029. <https://doi.org/10.1007/s00024-017-1739-z>
- Pavlidou, A., Kontoyiannis, H., Anagnostou, Ch., Siokou-Frangou, I., Pagou, K., Krasakopoulou, E., Assimakopoulou, G., Zervoudaki, S., Zeri, Ch., Chatzianestis, J., Psyllidou-Giouranovits, R., 2010. Biogeochemical Characteristics in the Elefsis Bay (Aegean Sea, Eastern Mediterranean) in Relation to Anoxia and Climate Changes, in: Yakushev, E.V. (Ed.), *Chemical Structure of Pelagic Redox Interfaces, The Handbook of Environmental Chemistry*. Springer Berlin Heidelberg, Berlin, Heidelberg, pp. 161–201. [https://doi.org/10.1007/698\\_2010\\_55](https://doi.org/10.1007/698_2010_55)
- Paytan, A., McLaughlin, K., 2007. The Oceanic Phosphorus Cycle 14. <https://doi.org/10.1021/cr0503613>
- Pearce, A.F., Feng, M., 2013. The rise and fall of the “marine heat wave” off Western Australia during the summer of 2010/2011. *Journal of Marine Systems* 111–112, 139–156. <https://doi.org/10.1016/j.jmarsys.2012.10.009>

- Peck MA, Catalán IA, Damalas D, M, E., Ferreira JG, Hamon KG, Kamermans P, S, K., Kreiß CM, Pinnegar JK, Sailley SF, NGH, T., 2020. Climate change and European Fisheries and Aquaculture: “CERES” Project Synthesis Report. Universität Hamburg. <https://doi.org/10.25592/UHHFDM.804>
- Perkins-Kirkpatrick, S.E., King, A.D., Cougnon, E.A., Holbrook, N.J., Grose, M.R., Oliver, E.C.J., Lewis, S.C., Pourasghar, F., 2019. The Role of Natural Variability and Anthropogenic Climate Change in the 2017/18 Tasman Sea Marine Heatwave. *Bulletin of the American Meteorological Society* 100, S105–S110. <https://doi.org/10.1175/BAMS-D-18-0116.1>
- Powley, H.R., Krom, M.D., Van Cappellen, P., 2017. Understanding the unique biogeochemistry of the Mediterranean Sea: Insights from a coupled phosphorus and nitrogen model: P and N Cycling in the Mediterranean Sea. *Global Biogeochem. Cycles* 31, 1010–1031. <https://doi.org/10.1002/2017GB005648>
- Powley, H.R., Krom, M.D., Van Cappellen, P., 2016. Circulation and oxygen cycling in the Mediterranean Sea: Sensitivity to future climate change: OXYGEN CYCLING IN THE MEDITERRANEAN SEA. *J. Geophys. Res. Oceans* 121, 8230–8247. <https://doi.org/10.1002/2016JC012224>
- Previati, M., Scinto, A., Cerrano, C., Osinga, R., 2010. Oxygen consumption in Mediterranean octocorals under different temperatures. *Journal of Experimental Marine Biology and Ecology* 390, 39–48. <https://doi.org/10.1016/j.jembe.2010.04.025>
- Rabalais, N.N., Díaz, R.J., Levin, L.A., Turner, R.E., Gilbert, D., Zhang, J., 2010. Dynamics and distribution of natural and human-caused hypoxia. *Biogeosciences* 7, 585–619. <https://doi.org/10.5194/bg-7-585-2010>
- Ramfos, A., Isari, S., Somarakis, S., Georgopoulos, D., Koutsikopoulos, C., Fragopoulou, N., 2006. Mesozooplankton community structure in offshore and coastal waters of the Ionian Sea (eastern Mediterranean) during mixed and stratified conditions. *Mar Biol* 150, 29–44. <https://doi.org/10.1007/s00227-006-0326-0>
- Renaud, M.L., 1986. HYPOXIA IN WUISIANA COASTAL WATERS DURING 1983: IMPLICATIONS FOR FISHERIES 8.
- Robinson, A.R., Golnaraghi, M., 1994. The Physical and Dynamical Oceanography of the Mediterranean Sea, in: Malanotte-Rizzoli, P., Robinson, A.R. (Eds.), *Ocean Processes in Climate Dynamics: Global and Mediterranean Examples*. Springer Netherlands, Dordrecht, pp. 255–306. [https://doi.org/10.1007/978-94-011-0870-6\\_12](https://doi.org/10.1007/978-94-011-0870-6_12)
- Rogers-Bennett, L., Catton, C.A., 2019. Marine heat wave and multiple stressors tip bull kelp forest to sea urchin barrens. *Sci Rep* 9, 15050. <https://doi.org/10.1038/s41598-019-51114-y>
- Rohling, E.J., Hilgen, F.J., 2007. The eastern Mediterranean climate at times of sapropel formation: a review 12.
- Rohling, E.J., Marino, G., Grant, K.M., 2015. Mediterranean climate and oceanography, and the periodic development of anoxic events (sapropels). *Earth-Science Reviews* 143, 62–97. <https://doi.org/10.1016/j.earscirev.2015.01.008>
- Rubio-Portillo, E., Izquierdo-Muñoz, A., Gago, J.F., Rosselló-Mora, R., Antón, J., Ramos-Esplá, A.A., 2016. Effects of the 2015 heat wave on benthic invertebrates in the Tabarca Marine Protected Area (southeast Spain). *Marine Environmental Research* 122, 135–142. <https://doi.org/10.1016/j.marenvres.2016.10.004>

- Ruiz-Barradas, A., Nigam, S., Kavvada, A., 2013. The Atlantic Multidecadal Oscillation in twentieth century climate simulations: uneven progress from CMIP3 to CMIP5. *Clim Dyn* 41, 3301–3315. <https://doi.org/10.1007/s00382-013-1810-0>
- Russo, T., Carpentieri, P., D'Andrea, L., De Angelis, P., Fiorentino, F., Franceschini, S., Garofalo, G., Labanchi, L., Parisi, A., Scardi, M., Cataudella, S., 2019. Trends in Effort and Yield of Trawl Fisheries: A Case Study From the Mediterranean Sea. *Front. Mar. Sci.* 6, 153. <https://doi.org/10.3389/fmars.2019.00153>
- San Diego-McGlone, M.L., Azanza, R.V., Villanoy, C.L., Jacinto, G.S., 2008. Eutrophic waters, algal bloom and fish kill in fish farming areas in Bolinao, Pangasinan, Philippines. *Marine Pollution Bulletin* 57, 295–301. <https://doi.org/10.1016/j.marpolbul.2008.03.028>
- Santinelli, C., Hansell, D.A., Ribera d'Alcalà, M., 2013. Influence of stratification on marine dissolved organic carbon (DOC) dynamics: The Mediterranean Sea case. *Progress in Oceanography* 119, 68–77. <https://doi.org/10.1016/j.pocean.2013.06.001>
- Schiaparelli, S., Castellano, M., Povero, P., Sartoni, G., Cattaneo-Vietti, R., 2007. A benthic mucilage event in North-Western Mediterranean Sea and its possible relationships with the summer 2003 European heatwave: short term effects on littoral rocky assemblages. *Marine Ecology* 28, 341–353. <https://doi.org/10.1111/j.1439-0485.2007.00155.x>
- Schmidtko, S., Stramma, L., Visbeck, M., 2017. Decline in global oceanic oxygen content during the past five decades. *Nature* 542, 335–339. <https://doi.org/10.1038/nature21399>
- Shutler, J.D., Smyth, T.J., Saux-Picart, S., Wakelin, S.L., Hyder, P., Orekhov, P., Grant, M.G., Tilstone, G.H., Allen, J.I., 2011. Evaluating the ability of a hydrodynamic ecosystem model to capture inter- and intra-annual spatial characteristics of chlorophyll-a in the north east Atlantic. *Journal of Marine Systems* 88, 169–182. <https://doi.org/10.1016/j.jmarsys.2011.03.013>
- Skiris, N., Sofianos, S., Gkanasos, A., Mantziafou, A., Vervatis, V., Axaopoulos, P., Lascaratos, A., 2012. Decadal scale variability of sea surface temperature in the Mediterranean Sea in relation to atmospheric variability. *Ocean Dynamics* 62, 13–30. <https://doi.org/10.1007/s10236-011-0493-5>
- Smale, D.A., Wernberg, T., Oliver, E.C.J., Thomsen, M., Harvey, B.P., Straub, S.C., Burrows, M.T., Alexander, L.V., Benthuisen, J.A., Donat, M.G., Feng, M., Hobday, A.J., Holbrook, N.J., Perkins-Kirkpatrick, S.E., Scannell, H.A., Gupta, A.S., Payne, B.L., Moore, P.J., 2019. Marine heatwaves threaten global biodiversity and the provision of ecosystem services. *Nat. Clim. Chang.* 9, 306–312. <https://doi.org/10.1038/s41558-019-0412-1>
- Sparnocchia, S., Schiano, M.E., Picco, P., Bozzano, R., Cappelletti, A., 2006. The anomalous warming of summer 2003 in the surface layer of the Central Ligurian Sea (Western Mediterranean). *Ann. Geophys.* 24, 443–452. <https://doi.org/10.5194/angeo-24-443-2006>
- Stramma, L., Johnson, G.C., Sprintall, J., Mohrholz, V., 2008. Expanding Oxygen-Minimum Zones in the Tropical Oceans. *Science* 320, 655–658. <https://doi.org/10.1126/science.1153847>
- Sutton, R.T., 2005. Atlantic Ocean Forcing of North American and European Summer Climate. *Science* 309, 115–118. <https://doi.org/10.1126/science.1109496>
- Taylor, J.R., Ferrari, R., 2011. Shutdown of turbulent convection as a new criterion for the onset of spring phytoplankton blooms. *Limnol. Oceanogr.* 56, 2293–2307. <https://doi.org/10.4319/lo.2011.56.6.2293>



- Taylor, K.E., Stouffer, R.J., Meehl, G.A., 2012. An Overview of CMIP5 and the Experiment Design. *Bulletin of the American Meteorological Society* 93, 485–498. <https://doi.org/10.1175/BAMS-D-11-00094.1>
- Troupin, C., Barth, A., Sirjacobs, D., Ouberdous, M., Brankart, J.-M., Brasseur, P., Rixen, M., Alvera-Azcárate, A., Belounis, M., Capet, A., Lenartz, F., Toussaint, M.-E., Beckers, J.-M., 2012. Generation of analysis and consistent error fields using the Data Interpolating Variational Analysis (DIVA). *Ocean Modelling* 52–53, 90–101. <https://doi.org/10.1016/j.ocemod.2012.05.002>
- Turley, C., Bianchi, M., Christaki, U., Conan, P., Harris, J., Psarra, S., Ruddy, G., Stutt, E., Tselepides, A., Van Wambeke, F., 2000. Relationship between primary producers and bacteria in an oligotrophic sea—the Mediterranean and biogeochemical implications. *Mar. Ecol. Prog. Ser.* 193, 11–18. <https://doi.org/10.3354/meps193011>
- Ulses, C., Estournel, C., Fourrier, M., Coppola, L., Kessouri, F., Lefèvre, D., Marsaleix, P., 2020. Oxygen budget for the north-western Mediterranean deepconvection region (preprint). *Biogeochemistry: Open Ocean*. <https://doi.org/10.5194/bg-2020-277>
- Vaquer-Sunyer, R., Duarte, C.M., 2008. Thresholds of hypoxia for marine biodiversity. *PNAS* 105, 15452–15457. <https://doi.org/10.1073/pnas.0803833105>
- Vedor, M., Queiroz, N., Mucientes, G., Couto, A., Costa, I. da, Santos, A. dos, Vandeperre, F., Fontes, J., Afonso, P., Rosa, R., Humphries, N.E., Sims, D.W., 2021. Climate-driven deoxygenation elevates fishing vulnerability for the ocean’s widest ranging shark. *eLife* 10, e62508. <https://doi.org/10.7554/eLife.62508>
- Wernberg, T., Smale, D.A., Tuya, F., Thomsen, M.S., Langlois, T.J., de Bettignies, T., Bennett, S., Rousseaux, C.S., 2013. An extreme climatic event alters marine ecosystem structure in a global biodiversity hotspot. *Nature Clim Change* 3, 78–82. <https://doi.org/10.1038/nclimate1627>
- Wright, J.J., Konwar, K.M., Hallam, S.J., 2012. Microbial ecology of expanding oxygen minimum zones. *Nat Rev Microbiol* 10, 381–394. <https://doi.org/10.1038/nrmicro2778>
- Yamaguchi, R., Suga, T., 2019. Trend and Variability in Global Upper-Ocean Stratification Since the 1960s. *Journal of Geophysical Research* 16.
- Yeruham, E., Rilov, G., Shpigel, M., Abelson, A., 2015. Collapse of the echinoid *Paracentrotus lividus* populations in the Eastern Mediterranean—result of climate change? *Scientific Reports* 5, 13479. <https://doi.org/10.1038/srep13479>